

SINGLE PARTICLE INDUCTIVELY COUPLED PLASMA SPECTROSCOPY
(SP-ICP-MS) AS A TOOL FOR IDENTIFYING, QUANTIFYING
AND STUDYING THE TRANSFORMATION OF
ANTHROPOGENIC NANOMATERIALS

by
Shaun Bevers

© Copyright by Shaun Bevers, 2023

All Rights Reserved

A thesis submitted to the Faculty and the Board of Trustees of the Colorado School of Mines in partial fulfillment of the requirements for the degree of Doctor of Philosophy (Geochemistry)).

Golden, Colorado

Date _____

Signed: _____

Shaun Bevers

Signed: _____

Dr. James Ranville
Thesis Advisor

Golden, Colorado

Date _____

Signed: _____

Dr. James Ranville
Professor, Program Head
Geochemistry

ABSTRACT

Nanomaterials in the environment occupy a wide variety of roles in the environment due to their unique, size-dependent reactivity. Abundant, natural nanomaterials influence a wide variety of geochemical processes such the global transport of micronutrients through aeolian dust or the bioavailability of metal ions in aqueous systems. Furthermore, the expansion of human activity has caused newer, incidental and engineered nanomaterials to enter the environment in increasing concentrations with unknown effects. Characterization of these environmental nanomaterials is essential to understanding natural geochemical cycles and the effects that anthropogenic activity have upon them.

Single Particle Inductively Coupled Plasma Mass Spectrometry (spICP-MS) is a technique of growing importance in the analysis of environmental materials. Nanoparticles are ablated, ionized and detected through this technique revealing their elemental content and size. Although in widespread use, environmentally sampled nanomaterials can confound this technique due to their broad and continuous distributions of particles of sizes ranging in orders of magnitude. The three chapters of original research presented herein attempt to lay out guideposts for the analysis of these environmental nanomaterials. The first chapter combines simple techniques such as settling and filtration to increase the depth of information obtained from a simple spICP-MS analysis and presents the results of combining spICP-MS with a time-of-flight detector for particle-specific, multi-element characterization. The second chapter lays out a method of modeling spICP-MS analysis using a power law model which provides a more accurate measurement of particle size and number concentration than a simple analysis of mean particle size and detected number. Lastly, we apply the lessons of the previous chapter to study the UV degradation of nanoplastics, a difficult to analyze and dangerous environmental contaminant. The lessons in spICP-MS data analysis and experimental design presented in this thesis will hopefully be of use to future environmental researchers.

TABLE OF CONTENTS

ABSTRACT	iii
LIST OF FIGURES.....	vii
LIST OF TABLES	xi
ACKNOWLEDGMENTS.....	xii
DEDICATION	xiii
CHAPTER 1 INTRODUCTION.....	14
1.1 Anthropogenic Nanomaterials in the Environment.....	14
1.2 Detection/Characterization of Anthropogenic Nanomaterials: Mass, Number and Size	15
1.3 Techniques for Nanomaterial Characterization	16
1.4 Continuous and Polydisperse Distributions Frustrate Environmental Colloid Analysis	20
1.5 Thesis Objectives.....	22
CHAPTER 2 QUANTIFICATION AND CHARACTERIZATION OF NANOPARTICULATE ZINC IN AN URBAN WATERSHED.....	25
2.1 Introduction.....	25
2.2 Materials and Methods.....	26
2.2.1 Study Location.....	26
2.2.2 Field Sampling.....	27
2.2.3 Laboratory Analysis/Preparation	28
2.2.4 Single Element, spICP-QMS Analysis	28
2.2.5 Additional Sampling Processing for spICP-QMS	29
2.2.6 Multi-Element, spICP-TOFMS Analysis	29
2.3 Results.....	30
2.3.1 Bulk Water Chemistry	30
2.3.2 Single Element, spICP-QMS Results	31
2.3.3 Multiple Element, spICP-TOFMS Results	35
2.4 Discussion.....	37
2.4.1 General Water Chemistry	37
2.4.2 Particle Analysis (spICP-QMS).....	38
2.4.3 Particle Analysis (spICP-TOFMS).....	41
2.5 Conclusion	44

2.6	Coauthor Contributions.....	44
2.7	Supporting Information.....	45
CHAPTER 3 NOVEL METHODOLOGY FOR THE ANALYSIS OF POLYDISPERSE ENGINEERED AND NATURAL COLLOIDS BY SINGLE PARTICLE INDUCTIVELY COUPLED PLASMA SPECTROSCOPY (spICP-MS)		
		50
3.1	Introduction.....	50
3.2	Materials and Methods.....	53
3.2.1	Nanoplastic Synthesis.....	53
3.2.2	Environmental NMs (Colloids).	53
3.2.3	Nano-analysis	53
3.3	Results and Discussion	54
3.3.1	Particle-Generated Background in Polydisperse Samples.....	54
3.3.2	Making Use of Imperfect Data: Power Law Modeling	56
3.3.3	Determining the “Artifact-Free” Size Distribution of Metal-Tagged NPs	58
3.3.4	β Values Reflect Physical Characteristics of the Measured PSDs.....	59
3.3.5	Changes in PSD/PNC of Al-bearing Stream Particles During a Storm Event	61
3.4	Conclusions.....	67
3.5	Acknowledgments.....	68
3.6	Coauthor Contributions.....	68
3.7	Supporting Information.....	68
3.7.1	Sampling Campaign	68
3.7.2	Laboratory Analyses.....	69
CHAPTER 4 SINGLE PARTICLE INDUCTIVELY COUPLED PLASMA AS A TOOL FOR THE STUDY OF NANOPLASTIC GENERATION AND PHOTODEGRADATION		
		76
4.1	Introduction.....	76
4.2	Research Objectives.....	80
4.2.1	UV Photodegradation of Nanoplastics	80
4.2.2	Nanoplastic Shedding and Fragility of UV Photodegraded Macroplastic.....	83
4.3	Materials and Methods.....	84
4.4	Results and Discussion	86
4.4.1	Establishment of the Conveyor Belt and Influence of NOM.....	86
4.4.2	Particle Fragility	91
4.4.3	Variable Sonication Time: Examination of the Magnitude of Photoinduced Fragility.	95
4.4.4	Macroplastic Fragility Analysis by spICP-MS.....	100
4.4.5	Overall Conclusions.	101

4.5	Supporting Information.....	102
CHAPTER 5 CONCLUSIONS AND FUTURE DIRECTIONS.....		104
5.1	Summary of Results and Implications	104
5.2	Future Avenues of Inquiry	106
REFERENCES		108
APPENDIX A PERMISSIONS		122

LIST OF FIGURES

Figure 1-1	Overview of analytical methodologies for nanomaterial characterization	16
Figure 1-2	spICP-MS Analysis of a mix of Au Nanoparticle Standards (Blue) and an Al colloid (Orange)sampled from Cherry Creek, Denver, CO (Chapter 3). Particle numbers have been normalized and particle size for the Al particles was calculated converting the detected Al mass into an equivalently sized metal Al particle. Monodisperse Au nanoparticle standards with mean diameters of 30, 60 and 80nm were mixed to create the Au NP mix.....	21
Figure 2-1	Map of the urban South Platte watershed and sampling locations for July 16th and 17th, 2018.....	27
Figure 2-2	spICP-Q-MS Results. (a) Number of Zn particles detected in a 60 second total acquisition time at each site, (b) Average Zn mass per particle.....	31
Figure 2-3	spICP-Q-MS Results. (a) Raw spICP-MS spectrum of unfiltered Zn particles for sampling site above the wastewater treatment plant, (b) Raw spICP-MS spectrum of 0.02 μm filtered sample collected from the South Platte River above the wastewater treatment plant.....	32
Figure 2-4	Distribution of resolved, dissolved, and non-resolved zinc species at the various sampling locations. Bolded numbers represent total zinc concentrations in $\mu\text{g/L}$	33
Figure 2-5	(a) Distribution of zinc species in West sand creek (7/16/2018) , concentrations in ppb, (b) Size distribution of raw vs. settled detected zinc events computed using ZnO density = 5.61 and a spherical geometry.....	34
Figure 2-6	Distribution of zinc speciation obtained by settling and 0.02 mm filtration across the watershed.....	35
Figure 2-7	Distribution of zinc species at different sampling sites as determined by spICP-TOFMS. Numbers represent the number of particles detected in 180 seconds of data collection.	36
Figure 2-8	(a) Number of particles detected defined by mass percent zinc, (b) Spherical diameters as related to the mass percent of zinc, computed by summing of all elements converted to oxides.	36
Figure 2-9	(a) Particle diameters of zinc-containing particles at different sites if only ZnO is considered, (b) Particle diameters at different sites if all elements measured by spICP-TOFMS are considered and converted to oxides.	37
Figure 2-10	Hydrographs for selected sampling locations A) West Clear Creek, B) West Sand Creek, C) South South Platte, D) Cherry Creek at Denver, CO, E) North South Platte, F) Cherry Creek below Cherry Creek Lake.	47
Figure 2-11	Turbidity plotted against various metal concentrations. A) Turbidity plotted against aluminum, silicon, and iron for all sample sites B) Turbidity plotted against zinc for all sample sites A) Turbidity plotted against zinc for all sample sites excluding WCIC, ESC, and WSC due to high flow conditions.....	48
Figure 2-12	Size Histograms for sp-ICP-QMS measurements of raw samples. Panels correspond to sites: A. AWWTP; B. BWWTP; C. WCIC; D. SSP; E. NSP (7/16); F. ECIC (7/16); G. WSC; H. ESC; I. CC. Histograms for ECIC (7/17) and NSP (7/17) not shown. Diameter	

	calculated by conversion of detected particle mass to a spherical metal Zn particle ($\rho = 7.14\text{g/cm}^3$).	49
Figure 3-1	PSDs of 10-fold serial dilutions of a 0.1% Ta-Ethoxide Polyvinylpyrrolidone (PVP) suspension (Undiluted Nominal Concentration: 10.1mg/mL PVP). Threshold size (dashed line) and the particle no. detected (bold number) for each dilution is indicated. Detected particle number was not corrected for dilution. Particle diameters reflect a conversion of the measured mass of ^{181}Ta to an equivalent diameter of a PVP particle based on the (0.1%) loading of Ta-Ethoxide and the polymer density (1.2 gm/cm^3).....	54
Figure 3-2	Dilutions of a 0.1% Ta-Ethoxide PVP suspension (nominal initial concentration of 88 mg/L PVP) (Panel A) and an Al-containing environmental colloid (Panel B) sampled from Cherry Creek, Denver CO on May 20 th 2022. Particle diameters reflect the equivalent size of PVP particles given the loading of Ta-Ethoxide (Panel A) or the equivalent size of K-Feldspar given the percent composition of Al (Panel B). For each dilution the particle numbers were normalized to lowest dilution (100x), denoted by (dc: dilution corrected).	56
Figure 3-3	Log-log plot of PSD for 10-fold dilutions ($10^2\text{x} - 10^6\text{x}$) of a 0.1% Ta-Ethoxide PVP suspension using spICP-MS (nominal undiluted concentration: 8.8g/L). Higher dilutions were normalized to the original 10^2x dilution. The model (black dashed line) is the linear regression of the power law model of particle number vs particle diameter (see text for details).	58
Figure 3-4	Log-log plots of (10^2 - 10^5x) dilutions of a 1% Ta-Ethoxide PVP (Panel A), and 10^2x and 10^3x dilutions of a 0.1% Ta-Ethoxide PMMA suspension (Panel B). For each dilution the particle numbers were normalized to lowest dilution. SEM micrographs of the dry 1% Ta-Ethoxide PVP (Panel C) and 0.1% Ta-Ethoxide PMMA powder (Panel D) mounted on carbon tape and sputter coated with Au.	60
Figure 3-5	spICP-MS results for a single 10^2x dilution (all dates) of Al-bearing colloids collected from Cherry Creek, CO USA across a major storm event. The table shows the calculated threshold particle size for each sample. Particle diameters reflect a conversion of the detected Al mass to the diameter of an equivalently sized K-Feldspar particle.....	62
Figure 3-6	Example log-log plot (5/21 data) used for power law analysis of Cherry Creek storm samples. Particle numbers are corrected for the dilution factor.	63
Figure 3-7	(a)Log α values and (b) β values were derived from the power law modeling of a dilution series for each date (data in SI). (c) PNC acquired from a single dilution (10^2x) across all samples (d) mean particle size acquired from a single dilution (10^2x) across all samples. Arrows show the temporal relationships among the samples and sampling dates of each data point labeled in panels (a-d).....	65
Figure 3-8	Hydrographs for Cherry Creek at the South Platte Confluence (Panel A, UGS GAUGE ID: 06713500) and at the mouth of Cherry Creek Reservoir along Cherry Creek (Panel B, UGS GAUGE ID: 06713000) over the course of the study time period, May 19 th – May 23 rd 2022. The confluence between Cherry Creek and the South Platte River is downstream of the study site whereas Cherry Creek Reservoir is upstream.....	70
Figure 3-9	sp-ICP-MS analysis of dilutions of monodisperse 50nm ^{197}Au Nanoparticles (Nanocomposix, San Diego, CA) with nominal concentrations of ^{197}Au ranging from 50ppb to 50ppt. A consistent particle detection threshold was used for all dilutions that converts to a particle diameter of 7nm.	71

Figure 3-10 Residual plots for linear regression of Log N vs Log D for 0.1% (w/w) Ta-Ethoxide PVP...	72
Figure 3-11 Comparison of the Power Law Model derived from the combined dataset to the dilution-corrected size distributions measured for the 0.1% Ta-Ethoxide (w/w) PVP suspension. The model line represents the results of linear regression of the Log-Log plot (Figure 3.3) and the power law model of particle number vs particle diameter generated from the linear regression. Particle numbers are normalized to the lowest dilution, denoted by (dc)...	72
Figure 3-12 Residual plots for linear regression of Log N vs Log D for 1% (w/w) Ta-Ethoxide PVP (Panel A) and 0.1% (w/w) Ta-Ethoxide PMMA (Panel B).....	73
Figure 3-13 A. Plot of Log Number vs Diameter of the combined datasets used for power law modeling overlaid with the model line (dashed redline) for each sample. B. Residuals of power law models for each sample.	73
Figure 3-14 Log N- Log D comparisons of sp-ICP-MS PSD data measured at dilutions spanning 100x to 10,000x for Cherry Creek Samples. Panels correspond to individual samples: a. 5/19; b. 5/20; c. 5/21; d. 5/22; and e. 5/23. Particle numbers are corrected for the dilution.	74
Figure 4-1 Schematic describing the (a) Quantification of nanoplastic released from a macroplastic as a function of UV photodegradation, and (b) Direct quantification of nanoplastic photodegradation.....	80
Figure 4-2 The “conveyor belt” hypothesis for the photodegradation of PM and the size regimes for which spICP-MS is applicable. spICP-MS Data broken into three different size ranges of analysis: (A) “Dissolved”; (B) Quantifiable Particles; and (C) Non-quantifiable Particles. The particle detection threshold (see chapter 3) has been converted to an equivalent mass of polymer assuming a 1% (w/w) loading of Ta-Ethoxide (details in Methods).	81
Figure 4-3 Sample parameters measured by spICP-MS for PM suspensions without NOM (PM) and with 10 mg /L SRFA (PM-NOM) over 13d of 300nm light irradiation: Particle Number Concentration (A, PM; B NOM-PM), Mean Particle Diameter (C PM; D NOM-PM), and Particle Mass Concentration (PMC) (E PM; F PM-NOM).	88
Figure 4-4 SPOS analysis of (a) D13 PM and (b) PM-NOM Suspensions. Particle numbers corrected for any dilution made prior to SPOS analysis. Although particles <2µm were measured by SPOS, analysis was focused on larger sizes which are practically invisible to the spICP-MS.	89
Figure 4-5 (A) PSD for PM dark control day 7 where blue and red lines represent spICP-MS analysis with and without sonication prior to analysis, respectively. (B) PSD for the day 7, irradiated PM samples A, B and C 7 where dashed and solid lines represent spICP-MS analysis with 0 or 5min sonication prior to analysis, respectively. Particle Diameters reflect an equivalent PM particle size to the 181Ta particle mass measured by spICP-MS. ..	91
Figure 4-6 Ratio of spICP-MS measured PNC and PMC for Sonicated (5min, SN) and Non-Sonicated (NS) samples for PM (Panels a and b, respectively) and PM-NOM suspensions (Panels c and d, respectively). There were no measurements of SN to NS material for the Dark and Light (A) samples on D11 for the PM suspension (Panels a/b).....	93
Figure 4-7 Normalized PNC for PM D7 5min Sonicated (solid lines) and No Sonication (dotted lines) samples (non-normalized data shown in Figure 5b).....	94
Figure 4-8 Non-Sonicated (NS) (a) Particle Number Concentration (part/mL), (b) Particle Mean Diameter, and (c) Particle Mass Concentration (PMC) as function of irradiation time	

measured by spICP-MS. Particle Diameters reflect an equivalent PM particle size to the ^{181}Ta particle mass measured by spICP-MS. (d) Particle Number Concentration (PNC) as measured by SPOS on D13 for the three irradiated samples. PNC is corrected for the dilution factor and volume measured during the SPOS experiment.....	96
Figure 4-9 Ratio of sonicated (15min) to no sonication PNC (Panel A) and PMC (Panel B) measured by spICP-MS.	97
Figure 4-10 PNC (a) and PMC (b) from spICP-MS analysis of D13 samples where samples were sonicated for 0, 5, 15 and 30min prior to analysis.....	97
Figure 4-11 Ratio of Sonicated (5min or 30min) particle number to Non-Sonicated Particle no measured by SPOS.	98
Figure 4-12 (A) Particle size distributions of nanoplastic released post-sonication for coupons UV irradiated for 0-14d. Each irradiation time has duplicates but only one PSD for each irradiation time is shown. (B) Average total PM particle mass released post sonication. Average value of two coupons per irradiation time.	100
Figure 4-13 spICP-MS PSD of D0 PM Suspension. Particle number concentration corrected for transport efficiency and dilution factor. Particle diameters reflects an equivalently sized PM particle to the amount of ^{181}Ta mass detected by the spICP-MS.	102
Figure 4-14 UV Absorbance of NOM control samples (no PM) at D0, and both the D13 Dark and Light Controls.....	103
Figure 4-15 Ratio of PNC (Panel A) and PMC (Panel B) of Sonicated (5min) (SN) to No Sonication (NS) measured by spICP-MS over the irradiation course. The PNC and PMC values for D13 C that are off scale are 10.33 and 3.08, respectively.	103

LIST OF TABLES

Table 2-1	Bulk water chemistry data for sample sites used in this study.	30
Table 2-2	Zn particulate and dissolved quantification at the various samples sites used in this study....	31
Table 2-3	Typical running instrument conditions for ICP-MS.....	45
Table 2-4	Total metal data from ICP-AES and anion data from IC (concentrations in mg/L).....	45
Table 2-5	Concentrations of Zn ($\mu\text{g/L}$) per Fraction for sp-ICP-Q-MS settling experiments.	46
Table 2-6	Concentrations of Zn ($\mu\text{g/L}$) per Fraction for sp-ICP-QMS filtration experiments.	46
Table 3-1	Results of Log-Log Linear Regression for the PVP and PMMA suspensions.....	75
Table 3-2	Results from sp-ICP-MS analysis of a 100x dilution of samples taken from Cherry Creek, CO USA. Calculated particle size assumes that the mass of Al detected is contained in K-Feldspar (2.7g/cm^3). Discharge was measured at the Cherry Creek USGS Gauge (ID: 06713500).....	75
Table 3-3	Results from sp-ICP-MS analysis of a 100x/1,000x dilution of samples taken from Cherry Creek, CO USA. Sample dilutions were chosen for each date such that the threshold value for particle detection is similar. Calculated particle size assumes that the mass of Al detected is contained in K-Feldspar (2.7g/cm^3). Discharge was measured at the Cherry Creek USGS Gauge (ID: 06713500).....	75
Table 3-4	Power Law Model β and $\log \alpha$ values obtained through linear regression of sp-ICP-MS data plotted as Log N vs Log D.....	75

ACKNOWLEDGMENTS

This thesis is the culmination of 4 years of collective effort. Illuminating conversations that I had with my lab group, especially Aaron Goodman and Zhaoxun Yang, helped shape the ideas presented in this thesis. The constant support of my family, my mother Helen Han and brother Michael Bevers kept me sane throughout graduate school. None of this, going to graduate school and earning a PhD would have been possible without the support of my lifelong partner Karoline Lambert who should receive a lion's share of the credit for helping me get through graduate school. Most of all, I would like to acknowledge the patience and good cheer of my thesis advisor Dr. James Ranville who is a gem of a human being on top of being an excellent scientist.

For my Mother, Helen Han: A completion of a dream that she had for the both of us.

1.1 Anthropogenic Nanomaterials in the Environment.

Nanomaterials, defined as having one dimension 1-100nm in length, have long been recognized as ubiquitous in the natural environment and possessing unique properties unlike those of their constituent molecules or macroscopic counterparts[1], [2]. These size-dependent properties allow them to have an outsized influence on many geochemical cycles and processes compared to their relative abundance. High surface-area to mass ratios allow them to be particularly good substrates for adsorption which can directly control the speciation and bioavailability of dissolved organic molecules[3] and metal ions[4]. Their nanoscale dimensions allows them to interact with electromagnetic radiation in unique ways allowing for their participation in a variety of photochemical reactions[5, p. 201].

Many of the unique properties of nanomaterials are tunable by size, and thus engineered nanomaterials for a particular function have become more and more integrated in commercial and industrial products[6]. Titanium dioxide (TiO_2) nanoparticles are widely incorporated in a wide variety of commercial products such as toothpaste, sunscreen, paint and dyes as well as foods as a white colorant due to its low cost and perceived inertness[7], [8]. Nanomaterials have been used to give additional functionality to construction materials[6] such as self-cleaning concrete[9] and copper nanoparticle-treated wood[10], increasing the lifespan of these materials. The use of nanomaterials for the photocatalytic breakdown of pharmaceuticals[11] and other organic molecules[12] in wastewater treatment is a growing field of study. Nano-agriculture is another burgeoning field demonstrating that crop yields and health can be improved through nano-encapsulation of vital micronutrients and pesticides[13].

On the other side of the coin, increased use of engineered nanomaterials results in increased environmental release of these materials as commercial products age or are discarded[14]. However, the amount of engineered nanomaterials entering the environment is dwarfed by anthropogenic, incidental nanoparticles which are unintentionally released as a byproduct of human activity. Fine and ultrafine particulate containing a wide variety of heavy metals are a concerning byproduct of internal combustion[15]. Automobiles themselves release a variety of incidental nanomaterials through emissions and the wear of automotive parts and tire wear particles[16], [17]. Tire wear particle toxicity in the environment has been recognized as particularly worrying, and the source of summer mass fish die-offs in urban areas[18]. Outside of aerosol emissions, plastic particles, -micro (<5mm in one dimension) or nano- (<1 μm), may be the next most abundant incidental nanomaterial in the environment. Yearly global production of plastics has risen to 391 million tons as of 2021[19] and the vast majority of this plastic remains in use or discarded into landfills or directly released into the environment with little

recycling[20]. Macroplastic debris in the environment are abiotically weathered through a combination of mechanical[21] and photodegradation[22] into microplastics. At smaller sizes, these particles can be degraded biologically by macro[23] and microorganisms[24]. Nanoplastics themselves have been recognized as distinct class of pollutant with characteristics wholly different than microplastics[25]. Nanoplastics act as a vector for pollutant transport[26] but may also release plasticizers and other toxic compounds[27], [28, p. 202].

1.2 Detection/Characterization of Anthropogenic Nanomaterials: Mass, Number and Size

As engineered and incidental nanomaterials become more common in the environment, our need to characterize them grows[2], [29]. However, this is no simple matter due to a variety of factors; a simple question like “how much is there?” is complicated by several factors. Detecting these materials in the environment is often difficult given that they share chemical composition with natural nanomaterials that may be orders of magnitude more abundant[2]. For example, naturally formed carbon nanoparticles from the decay of organic matter are abundant in the environment, masking the presence of anthropogenic plastic and tire particles[30]. Although titanium dioxide is one of the most widely used engineered nanomaterials, titanium is the ninth most abundant element in the earth’s crust[31] which results in a high natural, titanium particle background. Identification of anthropogenic particles against this background requires knowledge of particle composition. In the case of titanium particles, anthropogenic particles lack the elements associated with mineral-derived, natural titanium particles and thus the two can be discriminated using mass spectrometry[32], [33]. In addition to mass, knowledge of number concentration is essential. Standards for water quality based on mass concentration, such as those set by the EPA[34], may be inadequate in describing potential health and ecological hazards of a nanomaterial. For example, a milligram of total mass would equate to 10^6 x more particles with a radius of 10nm than with a radius of 1 μ m. Nanomaterial (NM) dosage for toxicology is better described as a function of size and particle number than it is by mass in many cases[35].

Apart from determining number concentration and mass of a nanomaterial, size is perhaps the most essential measurement given that the unique reactivity of nanomaterials depends upon it. Many of the reactions that nanomaterials participate in, such as adsorption or catalysis, critically depend on surface area. Additive release from nanoplastics, tire wear particles and other anthropogenic nanomaterials is expedited by higher surface area to mass ratios. Size is also essential to estimating the overall mobility of colloidal materials both airborne and in aqueous environments. Lastly, size is one of the prime determinants of particle toxicity as smaller particles have higher biological uptake and their mechanism of action may depend on their size[36], [37].

1.3 Techniques for Nanomaterial Characterization

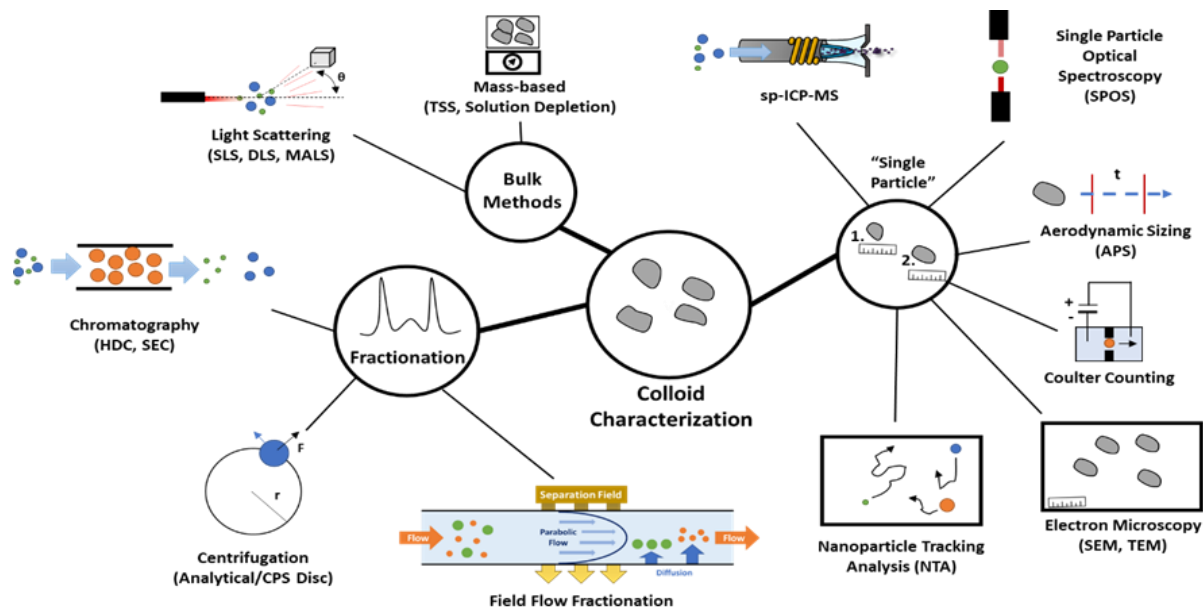


Figure 1-1 Overview of analytical methodologies for nanomaterial characterization.

Figure 1.1 shows many of the techniques[38] used for the characterization of the particle mass, number concentration and size. Single particle methods are defined as those in which particles are detected and sized individually, and aggregate measurements of colloidal properties such as mass, mean/median size are statistics of the particle population. In contrast with single particle methods, ensemble techniques[39] directly measure the average characteristics of the entire particle population.

Ensemble Techniques. When characterizing colloidal species, ensemble techniques where the properties of the entire colloidal population are measured in aggregate are the easiest place to start. Total suspended solids (TSS) is a classic ensemble technique where colloids are filtered from aqueous suspension and the resulting mass on the filter is weighed. Dynamic Light Scattering (DLS)[40], useful for estimating aggregate particle size, can be employed alone, on-line with a fractionation process or on post-fractionated samples. In this technique, polarized light is shined on a particle suspension and the particles will scatter this light destructively or constructively creating intensity fluctuations. The Brownian motion of the particles will cause an intensity pattern over a given amount of time that contains information about the diffusion coefficient of the particles in suspension. This intensity is fit with an autocorrelation function and information about particle size can be extracted.

Separations. Although DLS, TSS and other ensemble techniques including inductively coupled plasma mass spectroscopy (ICP-MS) provide bulk characterization of a colloid, these techniques can be confounded in the presence of polydisperse samples with a range of particle sizes requiring the use of a separation technique in tandem. For example, Field Flow Fractionation (FFF)[41] is a separation

technique where sample is injected into a flow channel and separation is achieved through the application of a force field perpendicular to the direction of flow. This field can be one of a variety of different forces including hydraulic, centrifugal, electric or thermal causing separation of particles on the basis of size, density, charge or thermophoretic mobility, respectively. Asymmetric field flow fractionation (AF4)[42] is the most common variation of the technique, where a cross flow is applied perpendicular to the laminar flow which propels the sample. The hydraulic force from the crossflow presses particles to the bottom of the separation channel where diffusion allows them to move back towards the center of the channel. The ability of the particle to move towards the center of the channel thus depends on their diffusion constant i.e. their size. Particles of different sizes will reside at different heights in the channel and thus the laminar flow parallel to the channel will propel them at different velocities, achieving separation. This technique has been successfully combined with a variety of detection techniques such as ICP-MS allowing for the measurement of elemental mass per size[43], [44]. Other common fractionation techniques include chromatography (hydrodynamic[45], size exclusion[46]) and centrifugation (analytical ultracentrifugation[47], differential centrifugal separation[48]). The combination of separation methods and ensemble measurement techniques allows for a more granular characterization of colloidal populations based on size or other physical characteristics.

However, separation techniques are not a panacea for characterizing polydisperse nanoparticle suspensions. Many of these techniques require high sample concentrations as there will be loss during the separation process itself, and the detection techniques used in combination might have low sensitivity e.g., DLS. Irregularly shaped particles can confound size-based separation methods e.g., FFF and samples containing a wide variety of sizes may challenge the resolution of many fractionation techniques.

Single Particle Methods. Although simple to employ, bulk techniques coupled with fractionation cannot always provide the required information to successfully characterize the mass concentration, number concentration and size of particles present in a nanoparticle suspension. To fill this gap, single particle techniques, where particles are individually detected, counted and sized, were developed. Although there are a multitude of techniques available, electron microscopy, nanoparticle tracking analysis and single particle ICP-MS (spICP-MS) are briefly described here.

Electron Microscopy (EM). Conventional optical microscopy, although convenient and inexpensive, is only useful for imaging materials >200nm in dimension beyond which a new illumination source is needed. Electron microscopy[49], [50] at its most basic involves illuminating an immobilized sample under vacuum with an electron beam. The electrons of the beam will pass through the solid (if it is sufficiently thin, <100nm in depth) or interact with the solid both elastically (backscattered electrons) and inelastically (secondary electrons, X-rays). Scanning electron microscopy (SEM), the most common EM technique for colloid analysis, involves detecting the elastically backscattered and/or secondary electrons emitted from the sample providing 3D morphology of the sample typically at a resolution of 10-20nm.

Transmission electron microscopy (TEM) relies on detecting the electrons that completely pass through the solid which can provide 2D imaging of the particle's internal morphology down to sub-nanometer resolutions.

The value of both techniques is that particles can be imaged and sized directly, with particle volume directly measured and not based on an assumed e.g., spherical shape. However, there are some noticeable disadvantages to using SEM/TEM, the first of which is that a large number of images are required to accurately measure the particle size distribution across a population of particles. For example, guidelines suggest that about 500 particle detections[51] are needed for accuracy, which can require 50-200 individual images depending on the concentration of particles immobilized to the SEM grid. Although there are automated methods for particle detection and counting such as ParticleSizer, a script for the ImageJ software (National Institutes of Health, Bethesda, MD), this process can still be laborious. It is also difficult to estimate the particle number concentration in the original sample on the basis of TEM/SEM images.

Sample preparation for SEM/TEM can also be problematic as aqueous suspensions must be dried down on a solid surface or immobilized on a filter. Drying can lead to a "coffee ring effect" which causes non-homogenous distributions of particles across the surface. Sample aggregation is also possible during sample preparation, leading to artificial distortion of the measured particle size distributions. Non-conductive samples, including most polymers and minerals, require a conductive coating of sputtered metal to reduce charging during sample illumination with the electron beam. This coating is generally thin, but a thick coating can obscure sample features. Although some elemental information may be obtained by analyzing the emitted X-Rays during EM analysis (X-Ray Fluorescence), particle identity in an SEM image can only be inferred from morphology and not chemical composition. Dust, metal particles introduced during the coating and other contaminating particles are difficult to discriminate from the sample itself.

Nanoparticle Tracking Analysis (NTA). Nanoparticle tracking analysis[52]–[54] is based on observations of the Brownian motion of particles in an aqueous suspension. In the absence of a concentration gradient or other hydrodynamic/thermal forces, small particles will move randomly in all directions which is known as diffusion. On long timescales, these movements cancel each other out giving a net result of no movement, but on short timescales, these motions can be observed. During NTA analysis, particles in an aqueous suspension are visualized and detected through their scattering of incident laser light in combination with imaging using a CCD camera. Particle motion is captured through the CCD camera images over small, time intervals (30ms) which can be analyzed to quantify particle motion in two dimensions. The observed mean displacement, $\overline{(x,y)^2}$, can then be related back to particle diameter, d , using the Stokes-Einstein Equation:

$$d = \frac{16k_B T}{3\pi\eta\langle x, y \rangle^2} \quad (1.1)$$

Where k_B is the Boltzmann Constant, T is temperature and η is the viscosity of the medium.

As particle detection is based on the scattered intensity of the particle, the minimum detectable size can vary depending on the refractive index of the particle material. For strongly scattering particles such as Au nanoparticles, the minimum detectable diameter is ≈ 10 nm whereas weakly scattering biological nanoparticles can only be detected to a size of ≈ 50 nm. Given that the technique is based on light scattering, there are a number of possible artifacts that can occur in NTA analysis. Larger particles or aggregates will produce greater scattered intensity than smaller particles and can mask these smaller particles, biasing the measured particle mean size[55]. Furthermore, due to the shape of the incident laser beam, particles with larger size or higher refractive index will be more successfully detected at the edge of the beam, leading to bias in the counting of these particles[54]. Sample particle number concentration may also be underestimated due to the aforementioned factors[56] and to the limitations of the CCD camera[53], [54].

Single Particle Inductively Coupled Mass Spectroscopy (spICP-MS). spICP-MS[57] utilizes the element specificity and low mass detection limits[58] of the ICP-MS to count and size individual, metal-containing particles. Particles are introduced singly into the plasma where they are converted to ions which register as a pulse of signal that can be distinguished from background. Background may consist of a combination of instrument noise or signal resulting from dissolved species. The use of 50 μ sec – 2 msec dwell times[59], [60] for the analysis results in the minimization of background noise. In this manner, the mass of element per particle can be determined, which can then be converted to a particle size with an assumed shape and elemental composition.

The two major advantages of this technique, the outstanding sensitivity and the ability to selectively detect only particles containing a certain element, has been leveraged to study anthropogenic materials in a wide variety of environmental settings[61]. However, there are some notable analytical challenges still facing the technique. High dissolved backgrounds that mask particle signals can be resolved using a fractionation technique such as FFF[62] or HDC[63], but these techniques can lead to sample loss. Many light elements (N, C, P and other p-block elements) are inefficiently converted to ions by the plasma, due to their high first ionization energies resulting in high detection limits. Carbon detection is particularly difficult as it is inefficiently ionized by the plasma and most aqueous samples contain a high amount of dissolved carbon species limiting the detectable ^{13}C particle size by spICP-MS to particles $> 1 \mu\text{m}$ in diameter [64]. Larger particles can be more difficult to characterize by spICP-MS due to the difficulty in transporting larger particles into the plasma and the uncertainty that these larger particles are fully converted into ions[64]–[66].

Lastly, although one can use spICP-MS to only detect particles containing an element of choice, this may not be enough to validate the particle's identity. For example, ZnO, is an engineered nanoparticle prevalent in a wide range of consumer goods from tires to sunscreens. However, ZnO or Zn itself is present in many different mineral particles making it difficult to speciate Zn-containing particles into anthropogenic and natural classifications[67]. Some of these problems are ameliorated by use of a time-of-flight detector instead a quadrupole detector for spICP-MS analysis, allowing for the quantitation of multiple elements per particle[32], [68]. For example, natural and anthropogenic titanium particles may be differentiated based on titanium's co-occurrence with other elements such as Nb. However, differences in detection limits between the different elements and the higher variability in particle composition on the nanoscale complicate these efforts[69].

Other Single Particle Techniques. Single particle optical sizing (SPOS)[70] is a technique that counts and sizes particles in aqueous suspension either through the scattering or obscuration of an incident laser beam. The amount of scattered (particles 0.5-2 μ m in diameter) or obscured (2-400 μ m) light produces a signal that is proportional to the volume of the particle. Coulter particle counters[71, p. 200], [72] are another single particle technique that sizes particles based on changes in electrical resistance as particles traverse a microchannel. Particles 0.4 μ m-1600 μ m in size can be sized based on the area of this pulse in the solution's electrical resistance. Both are simple techniques to use excepting that Coulter counting requires the particles to be in an electrolyte solution. However, both techniques are prone to particle coincidence[73], [74], i.e. where two particles enter the measurement zone and are counted as one particle. This practically limits their use to only dilute particle suspensions which is a limitation shared by spICP-MS.

1.4 Continuous and Polydisperse Distributions Frustrate Environmental Colloid Analysis

Comparison studies between different analytical techniques often use standard reference materials as a basis of comparison. In general, these reference samples are monodisperse[56], [75, p. 201], [76], i.e. they have particle number size distributions that are normally distributed about the mean size. In the case where the analysis of polydisperse samples by different techniques is compared[29], [77], the polydisperse test samples are a mix of monodisperse standards of different mean size. However, these monodisperse and polydisperse standards do not accurately represent the majority of sampled environmental colloids[78, p. 20].

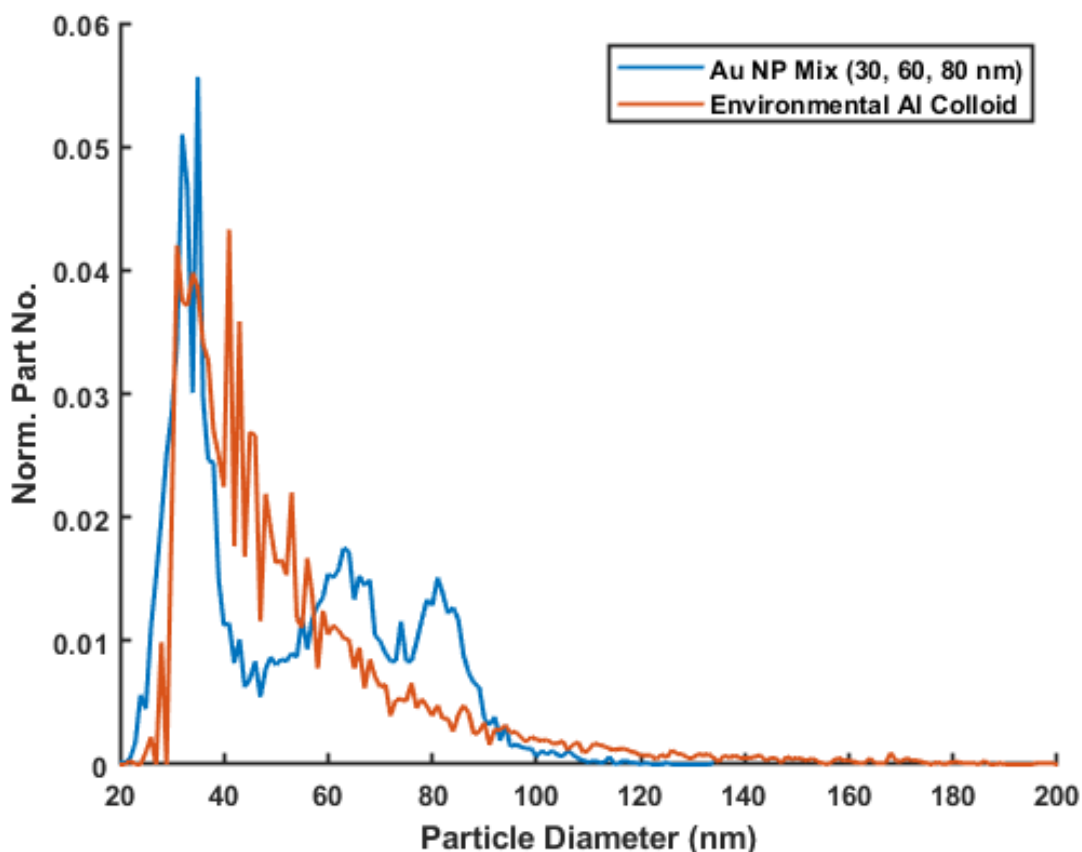


Figure 1-2 spICP-MS Analysis of a mix of Au Nanoparticle Standards (Blue) and an Al colloid (Orange) sampled from Cherry Creek, Denver, CO (Chapter 3). Particle numbers have been normalized and particle size for the Al particles was calculated converting the detected Al mass into an equivalently sized metal Al particle. Monodisperse Au nanoparticle standards with mean diameters of 30, 60 and 80nm were mixed to create the Au NP mix.

Figure 1.2 shows a particle size distribution (PSD) measured by spICP-MS of a mix of three Au nanoparticle standards (blue line, mean diameters of 30, 60 and 80nm) and an Al colloid sampled from Cherry Creek, CO (See Chapter 3 for sampling/analysis details). Although the mix of Au nanoparticle standards is polydisperse, the PSD has distinct features at the mean of each Au NP mix component. In contrast, the Al colloid has particles ranging across the 30-160nm measured size range. Further, the distribution of particle numbers across the measured size range is discontinuous for the Au NP mix compared to the Al colloid.

The relationship between particle number and size demonstrated by this Al colloid is common across many environmental samples and often follow Pareto’s Law (power law)[79]–[81]:

$$\frac{\Delta N}{\Delta D_p} = \alpha \left(\frac{D_p}{\Delta D_p} \right)^{-\beta} \tag{1.2}$$

This equation describes the change in particle number with size ($\Delta N/\Delta D_p$), as function of a constant α , multiplied by the particle diameter divided by bin size ($D_p/\Delta D_p$) which is raised to the constant $-\beta$. ΔD_p is the width of the measurement bin size. The constants α and β are related to the total particle concentration and the slope of the particle number-particle size relationship, respectively.

To illustrate the analytical challenges associated with environmental colloids, let us consider the sampled Al colloid from figure 2.1. This colloid likely contains a multitude of different Al-bearing particles, some natural (clays, minerals, etc.) and some anthropogenic (car wear particles, emission-derived, etc.), all with differing chemical composition. On top of the variety in chemical composition, the complex mélange of biological, chemical and physical forces creating and transforming these particles will lead to a diversity of shapes and sizes. Thus, a continuous distribution of particle sizes akin to figure 2.1. is obtained for many environmental colloid samples.

All facets of this colloid present challenges to accurate analysis. At high particle number concentrations, the high ratio of small particles to large particles can distort measured particle size distributions by causing particle coincidence, the erroneous counting of multiple particles as one particle. In techniques such as spICP-MS, SPOS or Coulter counting, this effect particularly worrisome as it can unequally distort the particle size distribution across the measured range. The presence of a mix of larger and smaller particles presents a challenge for light scattering techniques, as the larger particles will scatter more light, biasing any measurements towards them. Variations in particle shape and density combined with the continuous distribution of particle numbers by size can frustrate efforts to separate particles using techniques such as FFF or centrifugation. Further, variations in particle composition (clay, mineral, etc.) also makes it difficult to accurately assess particle size from particle mass measured through a technique like spICP-MS.

Outside of their characterization, the polydisperse nature of these real, environmental colloids frustrate attempts to study the wide variety of environmental transformations and reactions that these particles participate in. Changes in size-specific segments of this data can be difficult to discern, which frustrates efforts to study differences in colloidal populations after major environmental events such as a storm or due to exposure to solar radiation. Many environmental colloids contain such a wide diversity in particle types, any environmental transformation is bound to affect only one segment of the total colloid. New methodology is necessary if these types of commonly encountered environmental colloids and the size-dependent reactions are to be successfully characterized and quantified.

1.5 Thesis Objectives.

The principal goal of this thesis is to develop methodology enabling for the accurate detection and quantification of anthropogenic nanomaterials for the purposes of both quantifying their impact on the environment and studying the reactions in which they participate. The identification and quantitation of

anthropogenic nanomaterials in the environment is complicated by a background of natural particles with similar compositions and the polydisperse nature of sampled colloids themselves. Single particle ICP-MS (spICP-MS) was chosen as the analytical technique of choice for this thesis due to its outstanding elemental sensitivity coupled with its ability to discriminate between particles based on elemental composition.

Chapter 2 of the thesis is focused on the question of identifying anthropogenic particles against a natural particle background[67]. To this end, Zn speciation was studied pre- and post-storm in the surface waters of the urban South Platte watershed (Denver, CO) using spICP-MS. The principal hypothesis was that the elemental specificity of the spICP-MS could be combined with pre-analysis filtration or settling to discriminate between natural and anthropogenic materials. Analysis was conducted using both a quadrupole detector (sp-ICP-Q-MS) for the detection of a single element (^{64}Zn) and a time-of-flight (sp-ICP-TOF-MS) detector for the detection of a broad range of elements (Al, Si, Fe, Cu, Ti, Zn, Pb, Cd, Cu, Nd, Ni, and Au). Additional sample processing, 0.02 μm filtration and settling, were used to further fractionate samples for sp-ICP-Q-MS analysis. The highlights of this work included the ability of filtration combined with spICP-Q-MS to speciate the total Zn into particulate fractions and identify larger particles with only a small mass fraction of Zn. Multi-element spICP-TOF-MS results were used to speciate Zn-containing particles, revealing the possible presence of anthropogenic particles in the form of particles only containing Zn.

Chapter 3 presents a study designed to improve our ability to use single particle ICP-MS to analyze polydisperse nanomaterials. Polydispersity of environmental colloids is an under-researched topic, and the possible power-law distribution of particle number by particle size can have detrimental effects on their quantitation. A manufactured, polydisperse, Ta-tagged nanoplastic suspension with a power-law particle size distribution was used to demonstrate the presence of a particle-based background in spICP-MS analysis. Prior work focused on spICP-MS background signal generally focused on instrument noise or dissolved background, and the likelihood of a particle-based background at high particle concentrations is often underreported. Data from multiple dilutions combined with a power law model was shown to successfully resolve this particle background and provide quantitation across a range of sizes impossible with only a single dilution. Further, the application of this methodology to an environmental system was demonstrated through the analysis of Al-bearing colloids in an urban stream pre- and post- storm. This new spICP-MS methodology was compared to traditional, single dilution spICP-MS to highlight the data distortions inherent in using a single dilution. This project highlighted the presence of particle-based backgrounds in spICP-MS measurements and demonstrated a novel methodology to resolve these backgrounds.

Chapter 4 focuses on using the lessons from the previous two chapters to study the UVB photodegradation of tantalum-labeled, polymethylmethacrylate (PM) nanoplastic. Although spICP-MS

has been used in the past to study environmental transformations such as the dissolution of Ag nanoparticles[82] and the UVC photodegradation of PS microplastics[83], this technique has not been applied to a more environmentally relevant, polydisperse starting material such as this PM nanoplastic. Through quantification of nanoplastic mass via the homogeneously distributed tantalum tag, this study demonstrated that the UVB photodegradation of PM proceeds in a “conveyor belt” manner, where irradiated particles become smaller and smaller over time. Furthermore, the presence of particles made fragile by UVB irradiation is demonstrated through sample sonication, revealing another facet of the overall photodegradation process. Lastly, the ability of spICP-MS to follow the release of nanoplastics generated from the photodegradation of macroplastic and the increasing fragility of the macroplastic with UVB irradiation is demonstrated. This study demonstrates that spICP-MS can be used to answer lingering questions about the environmental transformation of nanoplastic and other incidental nanomaterials.

Lastly, Chapter 5 briefly summarizes the work presented in this thesis and offers avenues of future inquiry.

CHAPTER 2 QUANTIFICATION AND CHARACTERIZATION OF NANOPARTICULATE ZINC IN AN URBAN WATERSHED

Adapted from S. Bevers, M. D. Montano, L. Rybicki, T. Hofmann, F. von der Kammer, J. F. Ranville. “Quantification and Characterization of Nanoparticulate Zinc in an Urban Watershed.” *Frontiers in Environmental Science: Biogeochemical Dynamics*, 8:84 (2020).

2.1 Introduction

The combination of increasing global human populations, combined with rising urbanization have placed stress on urban watersheds through the direct influx of anthropogenic contaminants and other man-made influences[6], [84, p. 20]. The concurrent rise of impermeable surfaces in an urban environment results in greater stormwater run-off into these water bodies[85], carrying a variety of contaminants ranging from automotive fluids and resuspended particulate emissions[86], dissolved metals[87], and suspended solids[88], all of which having possible deleterious effects on human and ecological health[89].

The increasing development of nano-enabled consumer and industrial products has resulted in a number of potential release pathways for engineered nanoparticles (ENPs) during use and disposal[90]–[92]. In addition to intentionally ENPs, urban centers serve as a source of incidental nanoparticles (INPs) that are unintentionally produced from human-driven processes such as vehicle emissions[93], tire wear[94], and road dust[95]. These man-made particles infiltrate urban streams via storm water, adding to the naturally occurring nanoparticulates (NNP) load present from bio- and geogenic sources[2], [96].

One nanomaterial of particular interest is zinc oxide (ZnO). As an ENP, it is used in large quantities (10,000 tons annually circa 2012)[97] in tire manufacture[98], sunscreens[99], [100] and paints[101] with the potential to leach into the environment after use. There are several sources of Zn INPs as well, primarily generated from tire wear[102] and the resuspension of road dust[103]. While not highly toxic, zinc’s effect on aquatic species has led to EPA establishing hardness-dependent water quality criteria in the few tens to hundreds ug/L range[104]. In order to protect our urban watersheds, it is necessary to develop risk managements strategies that can effectively mitigate the influx of these potential contaminants. However, the complexity of nano-scale zinc in the environment requires the development of new sophisticated means of detection, quantification, and differentiation of the different sources of particulate zinc.

Single particle ICP-MS (spICP-MS) has a widely demonstrated utility in the analysis of natural waters for ENPs[105], [106] and NNPs[32], [107]. In a study examining TiO₂ ENP release from sunscreens, spICP-MS was utilized to demonstrate an increase in particulate Ti from anthropogenic activity[108, p. 201]. Hadioui et al. used ICP-quadrupole-MS coupled with ion exchange chromatography to measure

ZnO nanoparticles in the presence of high dissolved Zn backgrounds[109]. Expanding upon this work, Fréchette-Viens et al. employed a high-resolution, ICP-sector-field-MS instrument to push the size detection limits of ZnO nanoparticles in surface waters while noting the presence of larger heteroaggregate particles containing small amount of Zn[63]. Nevertheless, these studies also highlight a fundamental weakness of quadrupole mass analyzers in their inability to monitor multiple ions simultaneously. Though some studies have shown the potential to monitor two or more elements in a given particle event[110], [111], to accurately characterize the source of nanoparticulate Zn requires a means of analyzing multiple elements simultaneously. In recent years, commercially available ICP-time-of-flight-mass spectrometry (ICP-TOFMS) has shown the potential to significantly augment the utility of single particle analysis. The intrinsic nature of time-of-flight mass analysis permits the quasi-simultaneous detection of a wide mass range on microsecond time scales, the duration being bound to the extraction frequency. Typical acquisition times (33-46 μ s)[112]–[114] are on the same order as the nanoparticle detection events (500 μ s)[115]. Recent studies have demonstrated its utility in characterizing a variety of nanomaterials ranging from simple core-shell ENPs[68] and multi-element steel NPs[116] to more complex atmospheric nanoparticulates[117]. Given this capability, ascertaining the sources of NPs may be possible by monitoring the respective elemental or isotopic ratios on a particle-by-particle basis[32], [118].

In this study we demonstrate a multi-method approach for detecting and quantifying Zn NPs in the portion of the South Platte Watershed that encompasses Denver, CO (USA). Water samples were taken from multiple tributaries and the main stem of the South Platte River in mid-July 2018 within 2 days of a large storm event that significantly increased stream flow. Settling and filtration were used to separate different size fractions of particulate zinc, which were then quantified by spICP-QMS. Analysis by spICP-TOFMS provided particle-by-particle elemental associations of zinc to investigate the sources of Zn NPs across the watershed.

2.2 Materials and Methods

2.2.1 Study Location

The urban reaches of the South Platte River, the primary water source for Denver (CO, USA), as well as several of its tributaries were examined (Figure 2.1). The South Platte River enters the metro area from the southwest corner and exits north of the city. Major tributaries that feed the South Platte River within the Denver metro area include Clear Creek (CIC), Cherry Creek (CC) and Sand Creek (SC). Streamflow throughout the basin is low during fall and winter months. Flow increases beginning in April and peaks in the months of June and July as a result of mountain snow melt. Annual precipitation in the metro area ranges between 180 -380 mm per year, which mostly falls during April to September. Notably, much of

the summer precipitation occurs as brief-duration thunderstorms, resulting in short-term elevated stream flow. Sampling was timed to capture urban runoff following one such event in 2018.



Figure 2-1 Map of the urban South Platte watershed and sampling locations for July 16th and 17th, 2018.

2.2.2 Field Sampling

Sampling was performed on July 16th and 17th, 2018 following a rainfall event on July 14th-15th. Rainfall was not uniform across the basin and resulted in streamflow increases that varied among the sampling locations (hydrographs provided in supporting information Figure 2.10). On July 16th five sites were sampled (Figure 2.1); three sites examined the confluence between the South Platte River downstream Denver (flow to the north), Clear Creek (flow from the west) and Sand Creek (flow from the east). Two samples were also taken from the South Platte River at points approximately 500 m upstream and downstream of the Robert W. Hite wastewater treatment plant, the largest such facility in Denver. Locations are labeled as: WSC (West Sand Creek), ECIC (East Clear Creek), NSP (North South Platte), AWTTP (South Platte above the wastewater treatment plant), and BWTP (South Platte below the wastewater treatment plant). To examine tributary inputs from outside the central urban area, sampling on July 17th occurred at locations labeled ESC (East Sand Creek), WCIC (West Clear Creek), SSP (South South Platte) and CC (Cherry Creek). Both ECIC and NSP were also resampled on this date (Figure 2.1).

Grab samples were collected by submerging polyethylene bottles (1 L) approximately 10 cm or more below the surface, at a point at least 0.5 meter from the streambank. Bottles were filled and emptied three times to rinse the virgin bottles prior to collecting the sample. Subsamples were taken for chemical

analysis in the laboratory at Colorado School of Mines. The remaining sample was stored at 4°C until further processing and single particle ICP-MS analysis.

2.2.3 Laboratory Analysis/Preparation

Subsamples (10 ml) were subjected to a modification of the EPA Total Recoverable Method, EPA 200.2[119]. To accommodate our small-footprint digestion equipment, the method was modified by reducing the sample and acid volumes by a factor of 10. All other aspects of EPA 200.2 remained unchanged. All samples were shaken prior to subsampling. Cation concentrations were determined by ICP-OES (PerkinElmer Optima 7300 DV), the operational details and QA procedures being provided in ESI. Major anions (Cl and SO₄) were measured by ion chromatography (Dionex: ThermoFisher, ICS-900). Turbidity measurements were made using a Hach DR 890 meter (HACH Method 8237), and results reported in formazin absorbance units (FAU). Results for metals, anions and turbidity are reported in Table 2.1.

2.2.4 Single Element, spICP-QMS Analysis

Single particle (spICP-QMS) analysis was performed using an ICP-quadrupole mass spectrometer (NexION 300 D, Perkin Elmer). For single particle analysis, the transport efficiency (TE) was determined using the mass-based method as described by Pace et al[120]. A 60 nm Au nanoparticle (NIST SRM 8013, citrate-stabilized, mean size of 56.0 ± 0.5 nm by TEM) was used as a known mass standard. Dissolved standards of 0 to 100 ppb Au (SPEX CertiPrep in 2% (v/v) hydrochloric acid) and Zn (SPEX CertiPrep in 2% (v/v) nitric acid) were prepared using nitric acid (Fisher Scientific, Optima grade, 32-35%) and were diluted in Milli-Q water (18.2 M Ω -cm, Barnstead International) on the day of each analysis. All unfiltered samples and Au NP standards were sonicated in a sonic bath for 5 minutes prior to analysis. ¹⁹⁷Au or ⁶⁴Zn were analyzed using a dwell time of 100 μ s, no settling time, sample flow rate = 0.3 ml/min, a total data collection time of 60 s, and a very short detector dead time (35 ns) between readings. Data acquisition and data processing were performed using the Syngistix™ Nano Application Module (PerkinElmer). TE determination is built into the software and is calculated in order to determine NP mass (from which size is computed) and the number concentration. Particle events were identified as ICP-MS responses that were deemed to be above the threshold intensity, which was determined in real-time using the average background plus 3σ [120]. The particle number concentration is computed from the number of NP events detected after adjustment for the sample flow rate and TE. In addition to particle analysis, data collected by spICP-QMS was integrated over the entire 60 second analysis and, through use of the calibration curves, the mass concentration of Zn (ug/L) was determined.

2.2.5 Additional Sampling Processing for spICP-QMS

Samples were also filtered through a 0.02 μm filter (Whatman Anotop) prior to spICP-QMS analysis to obtain an estimate of the dissolved elemental concentration ($\mu\text{g/L}$). Filtered samples also provided a means of evaluating the spICP-QMS baseline obtained for non-filtered samples. This is often assumed to represent the dissolved element mass concentration ($\mu\text{g/L}$). A crucial parameter in sizing nanomaterials by spICP-MS is the selection of particle composition (i.e. element mass fraction and density), and geometry. As a quadrupole mass analyzer is only capable of selecting for one mass-to-charge ratio at a time, it is necessary to utilize other means to approximate the values needed for particle sizing. To provide this additional information on the Zn-containing particles, each non-filtered sample was gently agitated and then subjected to settling in a 15ml centrifuge tube (VWR, Falcon brand). Sampling from the upper 2 cm after 70 min provided a size separation at approximately 4.5 μm , assuming a spherical particle with a density of 2.5 g/cm^3 , typical of sediment minerals. Using ZnO density (5.61) gives an approximate size cutoff of 2.5 μm . Comparison of the observed changes in NP mass (size) and integrated concentration (number/ml and $\mu\text{g/L}$), to that predicted assuming the Zn was present as either ZnO or associated with sediment particles, provides insight into Zn form/mineralogy.

2.2.6 Multi-Element, spICP-TOFMS Analysis

Unfiltered samples were examined by multi-element analysis using single particle ICP- time-of-flight mass spectrometry (spICP-TOFMS) at the University of Vienna. Data were collected using an icpTOF 2R (TOFWERK AG, Thun, Switzerland). The ICP-TOF has a mass-resolving power of 6000 FWHM and a TOF extraction efficiency of 46 kHz, measuring a majority of the atomic mass range (7-250 m/z^+). The operation of the ICP-TOF utilizes a notch filter, which allows for the attenuation of up to four chosen masses, typically chosen for their abundance, which can lead to signal suppression of ions of interest. In this case, $^{40}\text{Ar}^+$, $^{16}\text{O}_2^+$, $^{35}\text{Cl}^+$, and $^1\text{H}^+$ were chosen. To improve the signal-to-noise of $^{56}\text{Fe}^+$ and $^{28}\text{Si}^+$, both of which have isobaric interferences in $^{40}\text{Ar}^{16}\text{O}^+$ and $^{14}\text{N}_2^+$ respectively, a 7% H_2/He mixture was used for a collision gas. The flow parameters of this gas were optimized before analysis for maximum sensitivity. Dissolved calibration solutions were prepared from ESI stock solution of dissolved metals (Al, Si, Fe, Cu, Ti, Zn, Pb, Cd, Cu, Nd, Ni, Au), analyzed prior to each sample run, with a continuing check verification standard (CCV) every 10 samples to account for any drift in instrument sensitivity. Additional and typical operating parameters are listed in supporting information (SI Table 2.3). A 100nm gold nanoparticle (BBI solution) was used as a known mass standard for obtaining TE. Due to limitations on data transfer from the data acquisition system to the laboratory computer, a 3 ms dwell time was used, despite the much shorter mass sweep time. To avoid particle coincidence for this long dwell time, a 1000 X dilution of the samples was required. This was not required for the spICP-QMS analysis.

The raw mass spectrum data were initially processed using TofWare (TOFWERK AG, Thun, Switzerland) which allowed for peak integration after initial subtraction of the spectral baseline. The resulting data was then processed via a custom Python script which performed calibration and spectral correction of the data. The script also then processed the single particle data according to the previously established methodology[59], [120], [121], which was similar to that used for spICP-QMS analysis. The subsequent data output resulted in a compiled list of particle events with time and their associated masses, which can then be converted into mass and size according to single particle theory.

2.3 Results

2.3.1 Bulk Water Chemistry

Table 2-1 Bulk water chemistry data for sample sites used in this study.

Sampling date	Turbidity (FAU)	Total recoverable metals (mg/L)					Anions (mg/L)		spICP-MS (ug/L)	% recovery
		Al	Si	Fe	Mn	Zn	Cl	SO4	Zn	
16-Jul										
NSP	50	1.39	7.01	1.57	0.20	0.043	60	77	11.5	27
WSC	170	7.57	20.64	6.86	0.38	0.068	65	171	13.9	20
ECIC	31	1.03	5.72	1.33	0.19	0.049	49	61	13.3	27
BWWTP	27	1.20	6.54	1.25	0.15	0.032	69	81	9.2	29
AWWTP	32	1.27	6.54	1.31	0.16	0.026	61	69	6.3	24
17-Jul										
NSP	29	1.00	6.87	0.99	0.20	0.050	93	151	13.7	27
ESC	258	10.67	27.88	9.03	0.35	0.072	42	196	19.9	28
ECIC	13	0.16	4.10	0.31	0.19	0.022	75	86	8.4	38
WCIC	7	0.17	3.20	0.34	0.05	0.061	14	35	23.2	38
SSP	19	0.61	3.79	0.62	0.40	0.009	67	73	1.8	20
CC	7	0.46	9.29	0.41	0.27	0.004	189	177	1.2	29

Total recoverable (TR) mass concentrations (ug/L) for those elements that were also examined by spICP-MS are given in Table 2.1, with major cation concentrations provided in SI. Although TR aggressively digests suspended sediments, in most cases particulate matter remained after the digestion and was removed by filtration (0.45µm, nylon, GEI). Samples from Sand Creek contained considerably more suspended sediment than those from other sites. Chloride and sulfate were the major anions measured (Table 2.1). Alkalinity, representing another possible major anion, was not measured. Turbidity (Table 2.1) was used as a surrogate for suspended sediment concentration.

2.3.2 Single Element, spICP-QMS Results

Table 2-2 Zn particulate and dissolved quantification at the various samples sites used in this study

Sampling date	Particle conc. (# / L)		Average Diameter (ZnO eq.)		Background dissolved Zn (ppb)		
	Raw	Settled	Raw	Settled	Raw	Settled	0.02 filtered
16-Jul							
NSP	7.6E+03	1.4E+05	67	96	11.2	8.4	3.9
WSC	2.2E+03	2.4E+05	124	95	13.9	7.2	0.9
ECIC	1.7E+05	1.2E+05	115	102	13.3	10.1	4.0
BWWTP	1.2E+05	4.5E+04	97	91	9.2	7.9	5.2
AWWTP	1.3E+05	8.6E+04	98	86	6.3	4.6	1.7
17-Jul							
NSP	6.4E+04	1.4E+05	106	96	13.7	8.2	1.6
ESC	2.0E+05	1.9E+05	118	107	19.9	13.5	0.3
ECIC	1.7E+05	1.5E+05	95	90	8.4	6.6	5.2
WCIC	6.0E+05	3.8E+04	135	132	23.2	18.6	1.9
SSP	1.3E+05	1.1E+05	73	66	1.8	0.3	0.2
CC	1.2E+05	1.0E+05	63	62	1.2	0.8	0.4

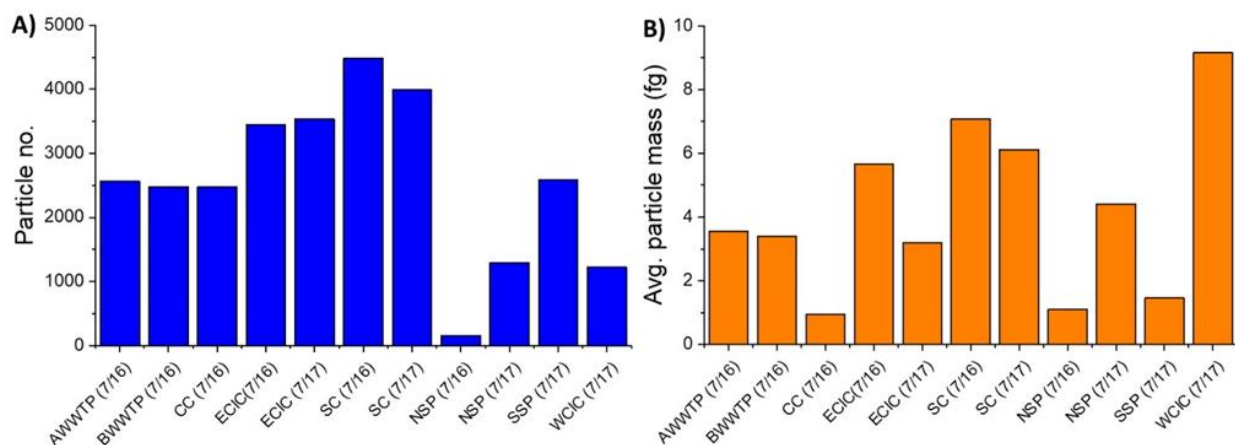


Figure 2-2 spICP-QMS Results. (a) Number of Zn particles detected in a 60 second total acquisition time at each site, (b) Average Zn mass per particle.

Data collected for the unfiltered sample using spICP-QMS was integrated over the entire 60 s analysis to determine the mass concentration of Zn (Table 2.1). The number of particles measured in the raw samples (60 s analysis time) were, with one exception, always greater than 1000, and in most cases greater than 2000 (Figure 2.2a). Accounting for flow rate and transport efficiency resulted in calculated particle number concentrations for most samples of between 7500 and 170,000 particles mL⁻¹ (Table 2.2). Integration of the particle-generated ⁶⁴Zn pulses yields a range of 0.5 to 9 femtograms for the number-weighted, geometric mean of the Zn mass contained in each particle (Figure 2.2b).

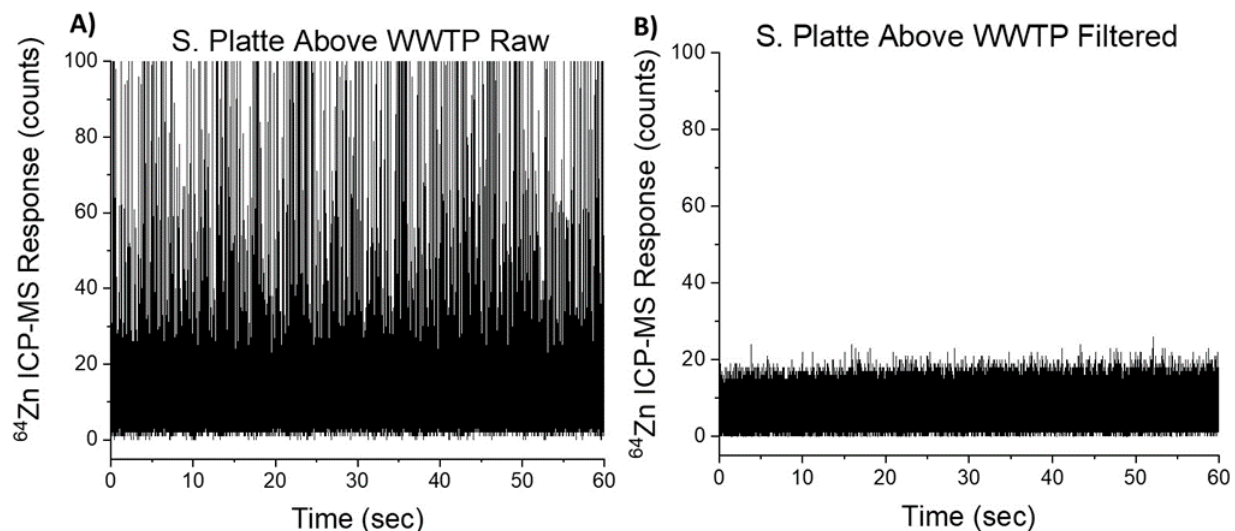


Figure 2-3 spICP-Q-MS Results. (a) Raw spICP-MS spectrum of unfiltered Zn particles for sampling site above the wastewater treatment plant, (b) Raw spICP-MS spectrum of 0.02 μm filtered sample collected from the South Platte River above the wastewater treatment plant.

Analysis of unfiltered samples by spICP-QMS resulted in a series of pulses (representing NPs) over an elevated background (Figure 2.3a). We have applied a methodology that defines the Zn distribution as being composed of resolved, unresolved, and dissolved fractions. Resolved nanoparticulate Zn (RP) represents particles that have sufficient Zn content to be discriminated from the baseline signal when using the Syngistix software. In spICP-MS analysis, the baseline elemental signal is often considered to approximate the dissolved metal concentration[110]. Analysis of the 0.02 μm membrane-filtered sample gives a more direct approximation of dissolved Zn (Figure 2.3b) by removing a majority of particulate Zn, although smaller NPs could be present in this fraction. This pore size is well below the size detection limit of the spICP-QMS (approximately 50 nm as ZnO)[58] and thus would not contain observable individual NPs. In this study, we also define an unresolved nanoparticle fraction (URNP) as the difference between the Zn baseline concentration in the raw sample minus the 0.02 μm filtered sample.

$$[\text{Zn}]_{\text{URNP}} (\mu\text{g/L}) = [\text{Zn}]_{\text{Raw,Diss.Baseline}} - [\text{Zn}]_{\text{0.02}\mu\text{m,Diss.Baseline}} \quad (2.1)$$

For the example shown, the baseline in the raw and the 0.02 μm filtered samples give “dissolved” Zn concentrations of 6.1 $\mu\text{g/L}$ and of 0.8 $\mu\text{g/L}$, respectively. Subsequently the difference of these two values give the URNP Zn concentration of 5.3 $\mu\text{g/L}$. The distribution in the Zn mass concentration of these three fractions across the watershed is shown in Figure 2.4 (SI Table 2.5).

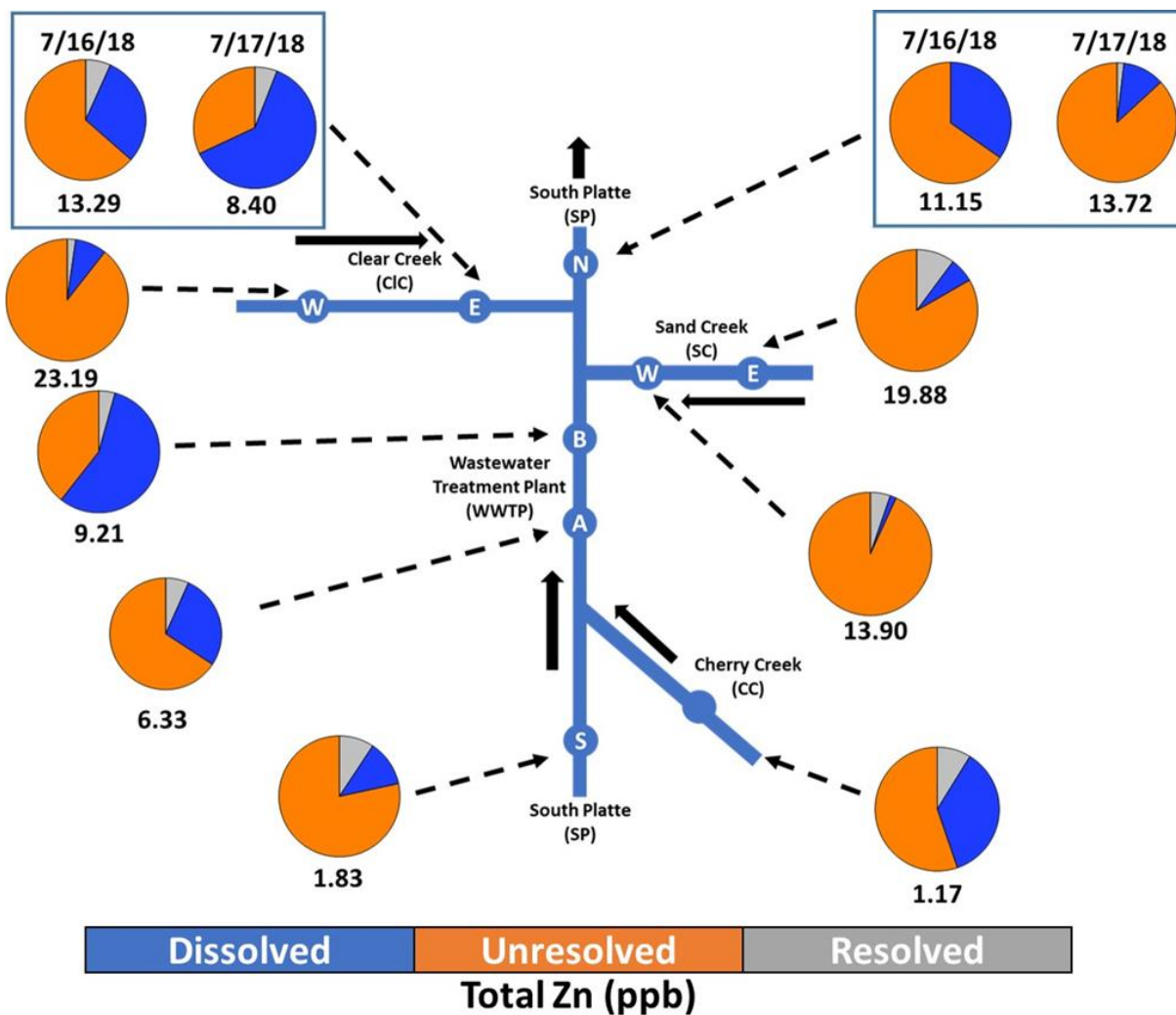


Figure 2-4 Distribution of resolved, dissolved, and non-resolved zinc species at the various sampling locations. Bolded numbers represent total zinc concentrations in µg/L.

Settling experiments were an attempt to examine Zn that might be present as ZnO (density = 5.61 g/cm³) and as zinc-associated with mineral matter (density = 2.65 g/cm³). Integration of Zn counts obtained by spICP-QMS for the settling experiments provided the mass concentrations of Zn (µg/L) in each of three fractions that were defined as particulate (i.e. subject to settling), colloidal (i.e. non-settleable) and dissolved (0.02µm filtrate). Subtraction of the integrated Zn counts measured after settling from that of the raw sample was used to compute the particulate fraction. Likewise, subtraction of the integrated Zn counts for the 0.02 µm filtered sample from the counts for the sample after settling yields a colloidal fraction.

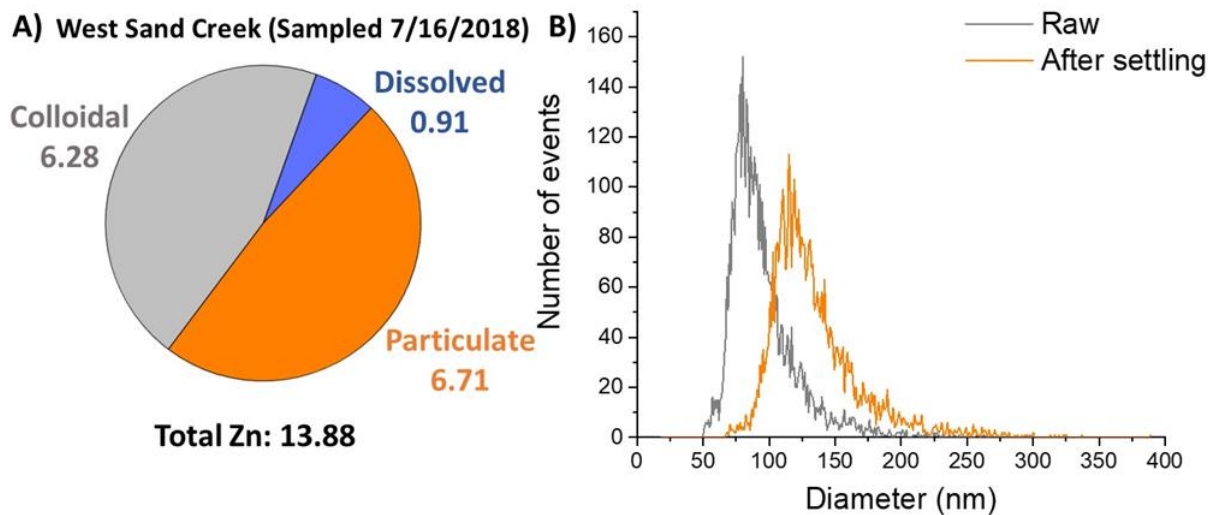


Figure 2-5 (a) Distribution of zinc species in West sand creek (7/16/2018) , concentrations in ppb, (b) Size distribution of raw vs. settled detected zinc events computed using ZnO density = 5.61 and a spherical geometry.

Figure 2.5a provides an example of this categorization for the mass concentration ($\mu\text{g/L}$) as well as the effect on the mean particle size determination, details provided in subsequent discussion of particle characterization. The distribution of these fractions across the watershed is shown in Figure 2.6 (SI Table 2.5).

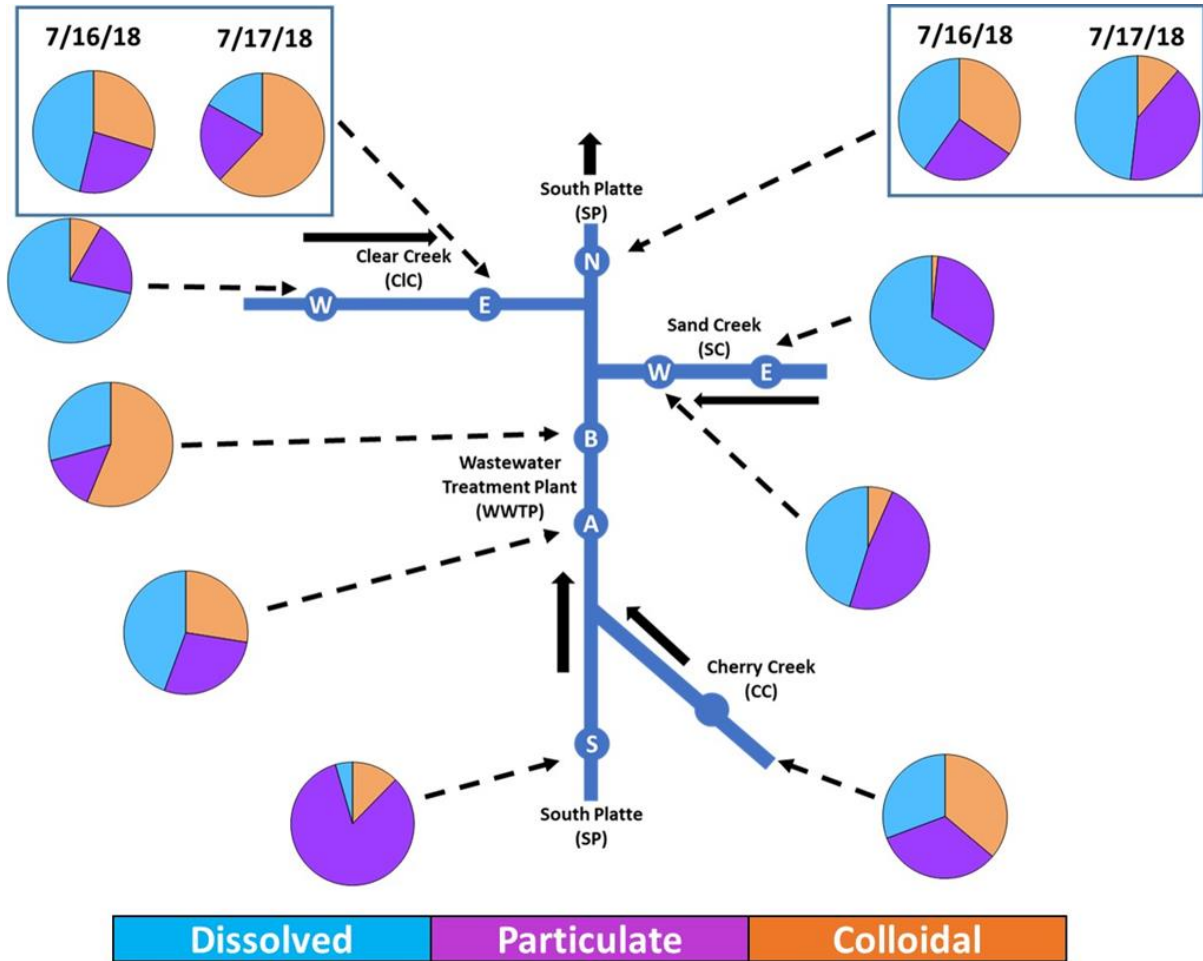


Figure 2-6 Distribution of zinc speciation obtained by settling and 0.02 mm filtration across the watershed.

2.3.3 Multiple Element, spICP-TOFMS Results

Results of the spICP-TOFMS analysis of samples collected from across the basin are presented as pie charts (Figure 2.7) with orange to represent particles that contained no detectable element other than Zn and blue as particles containing elements in addition to Zn, with Fe, Mn, Al and Si being the other detected elements. The numerical values of detected events of ^{64}Zn in these two classes are also displayed in Figure 2.7.

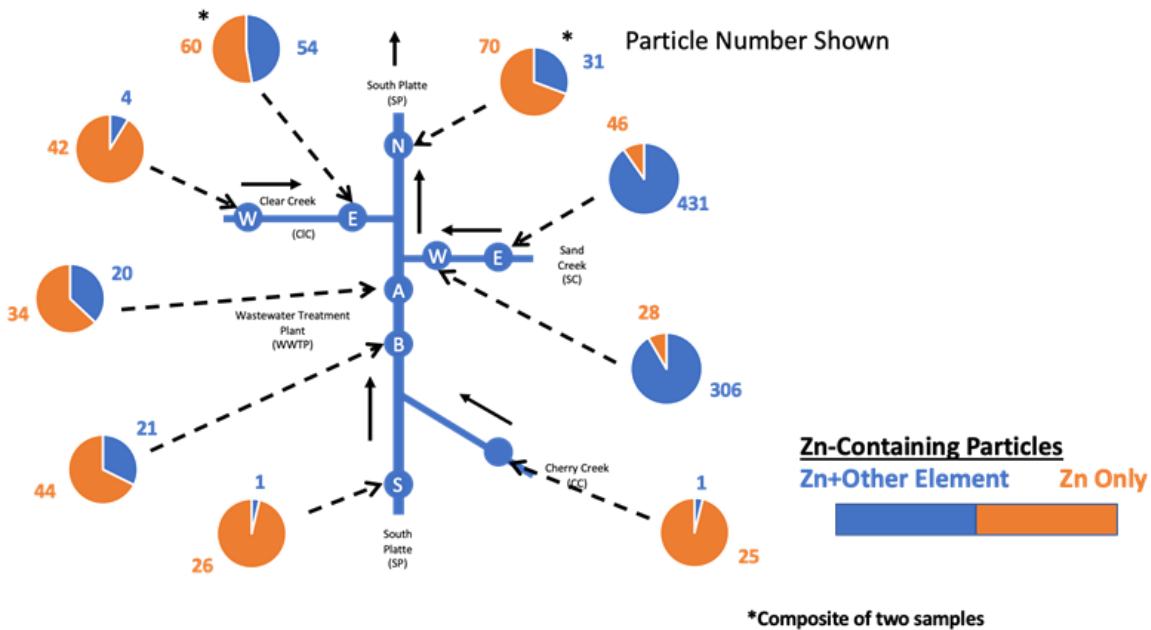


Figure 2-7 Distribution of zinc species at different sampling sites as determined by spICP-TOFMS. Numbers represent the number of particles detected in 180 seconds of data collection.

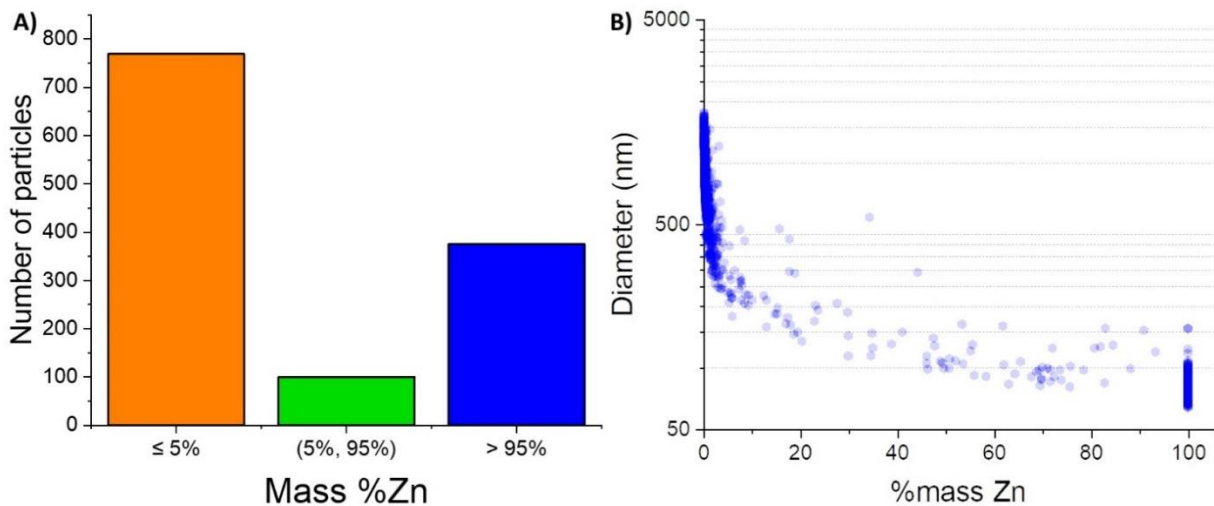


Figure 2-8 (a) Number of particles detected defined by mass percent zinc, (b) Spherical diameters as related to the mass percent of zinc, computed by summing of all elements converted to oxides.

Zn nanoparticles detected across all sites are represented in Figure 2.8a by the percent mass of Zn of which they are composed. Particles were detected primarily in two categories: those composed of high (>95%) and very low (<5%) proportions of Zn mass. With ICP-TOFMS we can use the observed elemental associations to make better estimates of overall particle size. Although the mineralogy is not known, it is a reasonable assumption that the Zn-only particles (> 95%) present in fully oxygenated surface waters are ZnO. To approximate the size of the particles containing multiple elements (< 5 % and

5-95%) we converted the elements to their oxides (i.e. Al_2O_3 , SiO_2 , MnO_2 , Fe_2O_3 , ZnO), calculated a volume for each oxide from the mass and density, summed the volumes of all oxides present in the particle and computed an average spherical size (Figure 2.8b). To examine spatial differences, the average and variation (box and whiskers plots) of particle diameters from each sample location were computed (Figure 2.9). Diameters were calculated assuming all Zn is present as ZnO (Figure 2.9a), as would be done for single element spICP-MS, and using the sum of the metal oxide mass, obtained by spICP-TOFMS (Figure 2.9b).

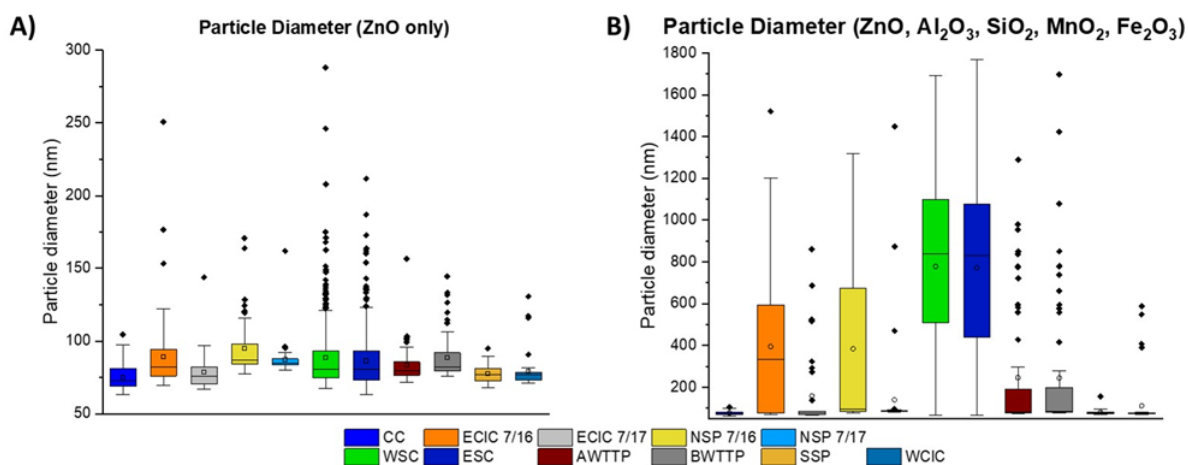


Figure 2-9 (a) Particle diameters of zinc-containing particles at different sites if only ZnO is considered, (b) Particle diameters at different sites if all elements measured by spICP-TOFMS are considered and converted to oxides.

2.4 Discussion

2.4.1 General Water Chemistry

Total Recoverable metals and turbidity across watershed. The total recoverable (TR) metals concentrations (Table 2.1) varied little across the watershed, but for two notable exceptions. Elevated levels of Si, Al and Fe (2-5x) were found in samples from both Sand Creek sites as compared to all other sampling sites. This observation correlated with a higher turbidity measured at these two sites (East, 258 FAU; West, 170 FAU), suggesting that these elements are present largely as part of the total suspended sediments. TR concentrations of each metal show strong correlations ($0.94 < R^2$) with turbidity (SI Fig 2.11), consistent with their abundance in earth materials and their low solubility in neutral waters. Total recoverable Zn shows a weaker relationship to turbidity, but there are several observations that bear further examination. The West Clear Creek site has a high total recoverable Zn concentration (0.068 mg/L) but a low turbidity (7 FAU), which could be attributed to dissolved Zn from mining inputs upstream of the watershed. Most of the urban waters have a moderate correlation ($R^2 = 0.66$) between these two parameters, if both sand creek sites are also excluded. These two sites show a combination of

high total recoverable Zn and turbidity, but the ratio of these two parameters is lower than for the other urban sites. This observation suggests that the high total suspended solids in Sand creek contains some amount of Zn, but not at the level seen in the other urban waters. The severe rainfall event on July 15th, 2018 (ESI Figure 2.11), which was more evident on the east side of the urban area, most likely mobilized sediment leading to the high measured turbidity. Although not investigated, we note that the central urban sites appear to have the higher levels of both sulfate and chloride, likely indicating generally poorer water quality than WCIC, a less urbanized upstream site.

Settling Results for mass concentrations (particulate, colloidal, dissolved). A comparison of background dissolved Zn concentrations measured by spICP-MS is presented for the raw, settled and 0.02 μm filtered samples (Table 2.2). The 0.02 μm sample approximates the truly dissolved fraction of Zn, as filtration removes all but the smallest of particulates. Differences in the Zn baseline between the raw and settled samples suggest that particles with low Zn mass (Figure 2.2b) are being removed by settling (Table 2.2). The total amount of Zn present in the settleable fraction (Figure 2.6, SI Table 2.5) varied anywhere from 15-83% of the total Zn across the watershed. The highest absolute particulate mass concentrations were found in Sand Creek (ESC, 6.4 $\mu\text{g/L}$; WSC, 6.7 $\mu\text{g/L}$). Sand creek also had the highest turbidity values and high total recoverable Zn, suggesting that Zn may be present adsorbed to larger sediment particles. This is corroborated by the high concentrations of settleable Zn. As noted previously the ratio of Zn to turbidity is lowest for Sand Creek, perhaps reflecting the transport of sediment from the less-urbanized eastern side of the watershed.

The colloidal portion of the total Zn (Figure 2.6) varied greatly across the watershed from 5-72% with the highest concentrations in West Clear Creek and East Sand Creek (WCIC, 16.62 $\mu\text{g/L}$; ESC 13.15 $\mu\text{g/L}$). Although the particulate and colloidal fractions form a higher proportion of the total Zn contributed by southern tributaries (SSP, CC), the higher absolute values of total Zn from the western and eastern inputs (WCIC, WSC/ESC) makes these the significant sources of particulate Zn.

2.4.2 Particle Analysis (spICP-QMS)

Integrated Zn mass concentration across watershed (recovery compared to TR). The percent recovery of Zn, defined as the total concentration measured by spICP-MS divided by the total recoverable (TR) concentration measured by ICP-AES, varied from 20-38% with a mean of 28% across the watershed (Table 2.1). The low percent recovery measured for the spICP-MS could be attributed to Zn contained in particles larger than what can be measured by the ICP-MS. The maximum size limit for the sp-ICP-MS is based on both the need to avoid clogging of the nebulizer and the maximum-sized particle that can be completely transported through the spray chamber and ablated by the plasma. A study of silica nanoparticles in spICP-MS suggests that the maximum ablation size is upwards of 1200nm[59], [115]. Analysis of TR metal requires sample acidification, which liberates an indeterminate amount of the Zn

contained in these larger particles, resulting in the higher TR Zn concentrations. As was previously noted, settled sediments were observed after acid digestion in some cases, especially the Sand Creek samples. Since the focus of this study is the nanoparticulate fraction, the low recovery is not of great concern but highlights that larger sediments need consideration if particulate-associated metal transport is of concern.

Resolved vs unresolved mass concentration. Additional fractionation was performed to gain more insights into the speciation of colloidal/NP Zn. One such analysis was to measure the dissolved Zn concentration in 0.02 μm filtered samples. It was hypothesized that the Zn baseline “dissolved” signal, obtained for raw samples, contained a large fraction of colloidal Zn that was not massive enough to exceed the size detection limit required to be registered as a particle. Filtration was chosen over dilution for examining this size fraction, as dilution may cause dissolution and/or disaggregation of particles, resulting in artificial changes to the mass distributions[122]. Although the amount of “dissolved” Zn (i.e. baseline concentration of raw samples) was greatly reduced through filtration, the 0.02 μm filtered samples still had particles roughly 50-60nm in mean diameter suggesting that some particles can still pass. This may also be a consequence of non-spherical shapes passing through the filter. Moreover, these particle detections may also be false positives due to their proximity to the size detection limit (45nm)[58]. Though particle information (i.e. size and number) cannot be obtained for the URNP fraction in this approach, it does provide insight into the mass concentration. Characterization of this URNP of Zn is important as these small particles may possess nano-characteristics (high specific surface area, bioavailability) different than their ionic and particulate counterparts[123], [124]. Across the watershed these unresolved fractions represent greater than 50 % of the Zn mass concentration (Figure 2.4), highlighting the importance of the smaller size fraction of NPs. Based on these results, more studies comparing filtration and dilution as fractionation techniques to better resolve the smallest NPs might provide a deeper understanding of nanomaterial transport and potential ecotoxicological risk.

Particle number, particle mass concentration, and particle mass (size) distributions. Across the South Platte Watershed, the number concentrations of Zn-containing particles measured by spICP-QMS were all within an order of magnitude ($\sim 60,000$ - $220,000$ particles/mL) with no higher particle numbers measured in the South Platte as compared to its tributaries (Figure 2.2a). Included in the data is a number concentration recorded for the NSP sample collected on 7/16/18 that is not in agreement with the sample collected on 7/18/18 or consistent with the value for the total Zn in the 7/16/18 sample. This result is considered an error particle counting but does not affect the integrated mass concentrations (i.e. Zn counts). The highest number concentration was observed in the Sand Creek samples, consistent with the high turbidity measured for these samples. Mean particle Zn mass (Figure 2.2b) across all sites was within an order of magnitude (1-10pg Zn/particle). Overall, the lack of increase in the NP number concentration or variation in NP Zn mass as the South Platte flows through the urban corridor suggests either no

substantial anthropogenic contribution of resolvable Zn NPs or that these measures are insensitive to urban impacts.

One notable trend is that the total Zn mass concentrations (Figure 2.4) were lower in the southern inputs to the South Platte (CC and SSP) compared to the urban sites downstream (AWWTP, BWTTP, NSP). The higher Zn mass concentrations in all three fractions (dissolved, unresolved, and resolved particles) in the downstream sites suggest that the urban environment is contributing Zn to the watershed. Among potential INPs, tire wear particles[16, p. 2], [17] and brake dust[125] are two likely sources of Zn particles in an urban watershed; as their presence in areas adjacent to roadways has been well-documented in soil, air and stormwater[6]. The Sand Creek site produced two samples with high Zn mass concentrations, which were principally contained in the resolved and unresolved particle fractions. Examination of the hydrographs around the watershed (Figure S2.1) shows that the rain event on July 15th, 2018 had considerable impact on Sand Creek. Flow increased by seven-fold from the event and this was the largest increase in flow of any South Platte tributary proportional to base flow. The increase in Zn particles, both resolved and non-resolved (Figure 2.4), could possibly thus be attributed to the rainfall pattern and the high volume of rainwater washing particles into Sand Creek and resuspending bed sediment. West Clear Creek is another tributary where high amounts of resolved and non-resolved Zn particles were observed (Figure 2.4) and these particles may be the result of widespread abandoned metal sulfide mines in the upper Clear Creek watershed[126].

Although the study focuses on the variation in concentration (mass and number) and chemical characteristics of Zn-containing particles within the urban watershed, it is useful to examine other information obtained by spICP-QMS, namely the particle mass (i.e. size) distributions (SI Figure 2.12). The lack of particles detected at small sizes (Figure 2.5b, computed for this example using a density of ZnO, 5.61 g/cm³), despite the limit of detection being an ample distance below the mean measured size, resulted in size distributions that appear approximately gaussian. With high dissolved Zn backgrounds, smaller particles that register close to the average background can be obscured. However, in these data sets the dissolved background does not fully account for the absence of smaller NPs. For example, based on the instrumental noise and the dissolved background, for East Sand Creek, the limit of detection is estimated to be 55nm, well below the leading edge of the particle distribution at roughly 77nm (Figure 2.5b). Whether the measured particle size distributions are abnormal for this type of analysis is an open question. Pareto's law suggests that particle distributions in the environment should follow a power law relationship between size and number, namely as particles get smaller, their number should exponentially increase[127]. Numerous studies have found that observed particle distributions can follow this law[128], display a Poisson distribution[17], [109] or even be bimodal[129]. These studies highlight many possible causes to explain distributions not following Pareto's law include influence of the type of sample (sediment vs. aqueous) or particle source (road wear vs. atmospheric). Thus, the lack of an observed

monotonically decreasing number-based size distribution may arise from real effects or from analytical artifacts. ENP may not behave according to Pareto's law in that they are manufactured and perhaps introduced into the environment with a more defined size distribution. Natural processes such as weathering, that produce NP, could adhere to the law more closely as nanoparticles are not the starting material but a product of a bulk transformation. Another analytical explanation for the observed particle size distributions is that although NPs may be present in the "gap" between the DL and the maximum of the distribution, random variation in NP-generated signal results in their partial undercounting when close to the background noise level (i.e. some particles generate counts below the 3σ size DL). Regardless of cause, for very polydisperse natural samples, the counting statistics obtained in this study may not be sufficient to draw a conclusion regarding the distribution shape. Previous studies[130] have suggested that 10^5 particles counted are necessary for a firm conclusion about particle size and have found a 3-10% variation in measured sizes. These are valid concerns that must be addressed in future field-based studies of NP size distributions.

Settling particle results (number, size, background/dissolved). In addition to filtration, settling experiments were a means of discerning more about the speciation of Zn particles present in the resolved and unresolved particulate fractions. Figure 2.5a compares the distribution of particle masses for the settled and raw samples of West Sand Creek (7/16/18). Both raw and settled samples had approximately the same number of particles (Raw, 4482 particles; Settled, 4820 particles) but their mean diameter was different (Raw, 134nm; Settled, 103nm). In the time-frame used, the 100 -200 nm particle distribution (Figure 2.5b) should not have been affected if particles were zinc metal or ZnO. Background Zn concentrations for the raw and settled samples were 13.90 and 7.19ppb, respectively, with a dissolved Zn concentration for the site (0.02 μ m filtered sample) was 0.91 ppb. It is apparent from the decrease in mean particle diameter and background Zn concentration in the settled sample, that settling removed Zn from solution even though the resolved Zn particles in the raw sample had a size distribution well below the calculated settleable size. A likely explanation is that part of the Zn measured in the raw sample is associated (either adsorbed or as a minor component) of larger minerals and hetero-aggregates. These larger particles containing low amounts of Zn could avoid detection as a resolvable Zn particle by the spICP-QMS. Thus, their absence from solution would be noted by a decrease in the background Zn concentration. This approach allows one to use spICP-QMS to gather more indirect evidence on the nature of metal-containing NPs but also leads direct to the obvious need for multi-element NP analysis.

2.4.3 Particle Analysis (spICP-TOFMS)

Given the varying morphologies and speciation of Zn, spICP-TOFMS was employed to quantify multiple elements within each particle. (Figure 2.7). One inherent advantage of the ICP-TOFMS is the ability to distinguish between particles composed only of Zn (as the cation) and those that contain

additional elements (excluding O, S, and other non-ionizable elements). This distinction is important in attempting to separate particles of anthropogenic origin from those of natural origin. Anthropogenic particles (i.e. tire wear, ENPs) are more likely to contain Zn as the only or primary metallic element. NNP with adsorbed Zn would contain other elements at amounts above that of Zn. Similarly, mineral NPs containing Zn within their lattice and hetero-aggregates of Zn-NPs and NNPs would also have some proportion of Zn but are likely to be principally composed of other elements.

It is important to note that fewer particles were counted by spICP-TOFMS, amounting to 10-20% that of the quadrupole instrument (Figure 2.7). Due to the difference in dwell times between the quadrupole and TOF instruments, 0.1 and 3msec, respectively, considerable dilution for the TOF experiments was necessary to avoid coincidence of particles within one dwell time. The 1:1000 dilution used in these experiments for the TOF measurements is the most likely cause of the low particle numbers detected by the TOF, however instrument sensitivity differences are also a possible cause. Data acquisition over a longer time period could be used to offset dilution differences and thus generate a comparable number of particles for both techniques.

Across all sites, similar average masses of Zn per particle were found in the Zn-only particles. Converting these masses to diameters, and assuming all the Zn is present as spherical ZnO NPs (Figure 2.9a), these particles were roughly 80 nm in diameter, most values falling within 20nm of this average value. We obtained a similar result for all Zn-containing NP when using an ICP-QMS, which provides only a single element analysis, concluding that the measured Zn NPs are relatively similar in size and composition across the South Platte watershed. However, with a TOF detector we can consider the other elements present in each particle, in this case Fe, Mn, Al and Si, which imply a more complex mineralogy for the Zn-containing particles. Mineral particles can promote adsorption, particularly the common metal oxides (Fe, Mn)[131] and aluminosilicate clays (Al, Si)[132]. Converting the mass of each element to an oxide (Fe_2O_3 , MnO_2 , SiO_2 , Al_2O_3), assuming a density and spherical geometry, and combining them with mass of ZnO from the previous figure, we can approximate a more likely size of the particles (Figure 2.9b). Plotting all particles by total oxide equivalent spherical size versus %m Zn (Figure 2.8b), we find a clear relationship with low % zinc being uniformly large (200-1000 nm) and high % zinc being uniformly small (60-100 nm).

The disconnect between the ZnO-only particle size and the particle size where all five elements are considered allows us to tease out differences in Zn particle speciation. Zn-containing particles where the Zn is adsorbed or hetero-agglomerated should show a large deviation between the particle radii calculated when considering ZnO only versus all five elements. It is expected that the Zn-adsorbed/aggregated particles would primarily be composed of other elements besides Zn and thus have only a small proportion of the total mass as Zn. This bears out for the size distributions of sampling sites such as Sand Creek, East Clear Creek and North South Platte (7/16/18), where the ZnO-only radius is much smaller

than the radius of particles where all elements were considered (Figure 2.9a, b). For Sand Creek, the higher proportion of Zn possibly contained as an adsorbate also supports the settling experiments utilizing the ICP-QMS. A high proportion of the Zn particles present in the Sand Creek samples could thus be classified as sediment particles with adsorbed Zn. Conversely, the small difference between Zn-only and multi-element particle size (Figure 2.9a, b) suggest that NPs primarily composed of Zn dominated other locations along the South Platte such as the wastewater treatment plant sites (AWTTP, BWTTP). This may be some indication of a greater anthropogenic contribution.

Separating particles based on the percentage of their % Zn mass also allowed for better speciation of the particulate-associated Zn in a sample. The different chemical properties of nanoparticulate Zn as compared to dissolved metal ions or adsorbed Zn is well known. ZnO and other metal oxide nanoparticles are potent reactive oxygen species generators and have ecotoxicity characteristics distinct from the dissolved forms of the metals[133]. Adsorption of heavy metals to nanoparticles is an important component of many biogeochemical cycles and identifying the prevalence of adsorbed metal can be a boon to modeling and environmental remediation[4].

Dissolution studies have shown ZnO can be soluble (7-16mg/mL)[134]–[137] at the pH values expected for these surface waters (pH 7-8). However, ZnO dissolution can be affected by inorganic factors including water hardness[135] and pH[136], [138] or organic species such as fulvic acids, NOM[136] or protein[139]. Also, ZnO may compose up to 1% by weight of the total tire mass[98] and ZnO particles from tire wear may be embedded in rubber, protecting them from solubilization. ZnO may also be protected from dissolution by being coated by a less soluble Zn mineral such as ZnCO₃[135]. Based on the host of factors that can affect ZnO particle dissolution, it seems highly possible that ZnO NP could be present in natural waters.

Future studies might be improved by including transmission electron microscopy (TEM) or scanning electron microscopy (SEM) to identify the chemical speciation of Zn particles be they ZnO, ZnS, ZnCO₃ or a more exotic metal compound. However, the ppb levels, which results in low particle numbers, make observing these particles by EM very difficult. The identification of the exact Zn particle mineralogy would aid in determination of their origin and determining a truer particle size. Similarly, Fe, Mn, Al and Si were assumed to be oxides for the purposes of calculating a particle size. This assumption was made for simplicity sake but does not reflect the probability that these elements are most likely present as a variety of aluminosilicate minerals. More detailed analysis of the mineralogy present in these samples would allow for more accurate representations of particle size where these elements are considered, although determining the association of Zn with the observed minerals is problematic at the low (< 5%) Zn contents observed in these waters.

2.5 Conclusion

By utilizing sp-ICP-MS, using both a quadrupole and a time-of-flight detector, the nanoparticulate populations present in an urban watershed could be more fully characterized. The unique use of settling and filtration experiments combined with an ICP-QMS provided further speciation of metal-containing particles using single element data. ICP-TOFMS analysis provided invaluable insights into the elemental abundances (i.e. mineralogy) present on a particle-by-particle basis. The totality of these analyses allows for the further speciation of metal-containing particles into particles composed completely of a given metal, and those with the metal adsorbed to, or incorporated within, colloidal mineral matter. This survey of the South Platte watershed found that Zn-only particles were more abundant in the central, more urbanized parts of the watershed, suggesting, but not confirming, anthropogenic origin. ZnO nanoparticles from tire wear particles were hypothesized, but not investigated, as the most likely source. If regulation is in the future for nanomaterial emissions, the ability to distinguish between particulate types will be invaluable. Most significantly, the study demonstrates that multi-elemental information, provided by an ICP-TOFMS, may form the future basis for developing the field of particle-by-particle geology, utilizing each particles elemental composition. Furthermore, a variety of different information about metal speciation can be derived from the application of settling and filtration as fractionation tools prior to ICP-QMS analysis.

2.6 Coauthor Contributions

L. Rybicki and J. F. Ranville were responsible for collection of the storm colloid samples from the South Platte watershed and the collection of spICP-Q-MS data at Colorado School of Mines. M. D. Montano, T. Hoffman and F. von der Kammer collected the spICP-TOF-MS data presented in this chapter at the Hoffman Laboratory at the University of Vienna. Additionally, J. F. Ranville and M. D. Montano supervised this work and helped prepare the manuscript for publication.

2.7 Supporting Information

Table 2-3 Typical running instrument conditions for ICP-MS.

ICP-QMS (NexION 300D ICP-MS)	
Instrument Parameter	Value
Nebulizer Gas Flow	0.86 – 0.98 ml/min
Sample Flow Rate	0.3 ml/min
Spray Chamber	Quartz cyclonic
ICP RF Power	1600 W
Dwell time	100 μ s
Transport efficiency	6-10%
Analytes	¹⁹⁷ Au, ⁶⁴ Zn
Analysis Time	60 s
Sample Flow Rate	0.3 ml/min
ICP-TOFMS (icpTOF-2R)	
Instrument Parameter	Value
Nebulizer Gas Flow	0.85 – 1.0 ml/min
Sample Flow Rate	0.28 ml/min
Spray Chamber	Quartz cylconic
ICP RF Power	1550 W
Dwell time	3 ms
Transport efficiency	7-15%
Analytes	²⁷ Al, ²⁸ Si, ⁴⁸ Ti, ⁵⁵ Mn, ⁵⁶ Fe, ⁵⁷ Fe, ⁵⁸ Ni, ⁶⁰ Ni, ⁶³ Cu, ⁶⁴ Zn, ⁶⁵ Cu, ⁶⁶ Zn, ⁶⁸ Zn, ¹¹⁰ Cd, ¹¹¹ Cd, ¹¹² Cd, ¹¹³ Cd, ¹¹⁴ Cd, ¹⁹⁷ Au, ²⁰⁶ Pb, ²⁰⁷ Pb, ²⁰⁸ Pb
Analysis Time	60 s
Sample Flow Rate	0.3 ml/min

Table 2-4 Total metal data from ICP-AES and anion data from IC (concentrations in mg/L).

Analyte	Detection λ	Sampling Date		7/16/2018					7/17/2018					
		DL	Mode	AWWTP	BWWTP	WSC	ECIC	NSP	WCIC	ECIC	SSP	CC	ESC	NSP
Al	396.153	0.001	Axial	0.564	0.517	1.238	0.453	0.549	0.059	0.082	0.095	0.198	1.463	0.207
Si	251.611	0.103	Axial	4.339	4.489	5.539	4.009	4.620	3.066	4.141	2.111	8.813	7.075	4.979
Fe	238.204	0.002	Axial	0.613	0.607	1.794	0.667	0.730	0.117	0.214	0.104	0.170	1.437	0.287
Mn	257.61	0.000	Axial	0.162	0.171	0.377	0.206	0.227	0.040	0.203	0.310	0.266	0.224	0.205
Zn	213.857	0.002	Axial	0.029	0.036	0.061	0.059	0.048	0.061	0.027	0.006	0.011	0.032	0.038
Zn	206.2	0.002	Axial	0.023	0.031	0.053	0.052	0.042	0.055	0.021	0.002	0.005	0.026	0.031
Ca	317.933	0.025	Axial	40.943	42.902	66.295	30.891	38.506	19.472	44.587	53.310	95.358	68.099	61.374
Mg	279.077	0.020	Radial	8.075	9.206	11.259	9.363	9.655	4.390	13.089	12.863	21.442	11.636	13.267
K	766.49	0.108	Radial	5.209	7.126	4.718	5.690	5.937	1.541	9.381	4.036	7.887	5.688	10.706
Na	589.592	0.019	Radial	41.990	50.837	59.818	39.968	45.168	8.127	62.080	39.066	113.478	53.868	79.251
S	180.669	0.0072	Axial	25.319	30.308	58.621	22.016	28.140	13.22378	32.46591	27.55753	63.50382	68.09999	54.87529
P	213.617	0.013	Axial	0.311	0.583	0.232	0.137	0.225	0.000	0.164	0.064	0.134	0.158	0.789
IC Data														
Cl		10.000		61.077	68.745	64.570	49.337	60.092	13.990981	74.97037	66.93894	188.9172	41.52354	92.65663
SO4		0	N/a	68.753	81.198	171.445	60.745	76.719	35.473524	85.78212	72.9656	177.1821	196.1048	151.1534

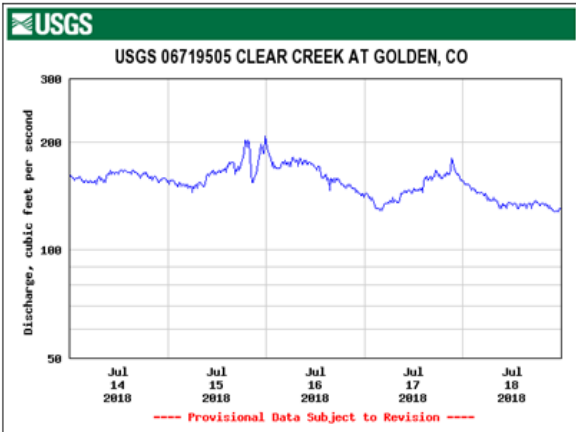
Table 2-5 Concentrations of Zn ($\mu\text{g/L}$) per Fraction for sp-ICP-Q-MS settling experiments.

Site	Fraction			Total
	Dissolved	Colloidal	Particulate	
Cherry Creek	0.42	0.36	0.39	1.17
E. Clear Creek (7/16)	3.95	6.16	3.19	13.29
E. Clear Creek (7/17)	5.21	1.42	1.77	8.40
N. South Platte (7/16)	3.86	4.49	2.80	11.15
N. South Platte (7/17)	1.55	6.61	5.56	13.72
AWWTP	1.74	2.81	1.78	6.33
BWWTP	5.18	2.69	1.34	9.21
E. Sand Creek	0.33	13.15	6.41	19.88
W. Sand Creek	0.91	6.28	6.71	13.90
S. South Platte	0.23	0.08	1.52	1.83
W. Clear Creek	1.93	16.62	4.63	23.19

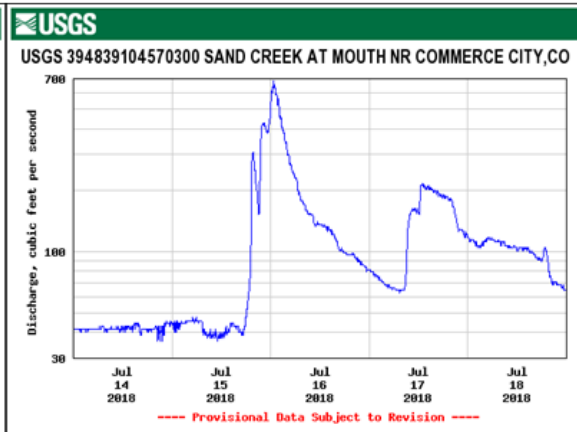
Table 2-6 Concentrations of Zn ($\mu\text{g/L}$) per Fraction for sp-ICP-Q-MS filtration experiments.

Site	Fraction			Total
	Dissolved	Resolved Nanoparticulate	Unresolved Nanoparticulate	
Cherry Creek	0.42	0.10	0.65	1.17
E. Clear Creek (7/16)	3.95	0.90	8.45	13.29
E. Clear Creek (7/17)	5.21	0.50	2.69	8.40
N. South Platte (7/16)	3.86	0.01	7.28	11.15
N. South Platte (7/17)	1.55	0.26	11.91	13.72
AWTTP	1.74	0.42	4.17	6.33
BWTTP	5.18	0.40	3.63	9.21
W. Sand Creek	0.33	1.05	18.51	19.88
E. Sand Creek	0.91	1.41	11.58	13.90
W. Clear Creek	1.93	0.52	20.74	23.19
S. South Platte	0.23	0.17	1.43	1.83

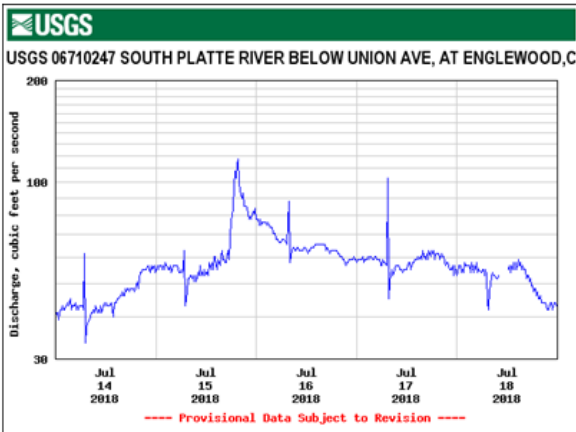
A) West Clear Creek



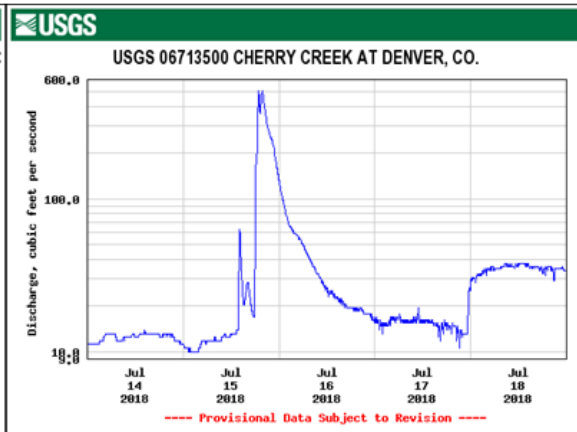
B) West Sand Creek



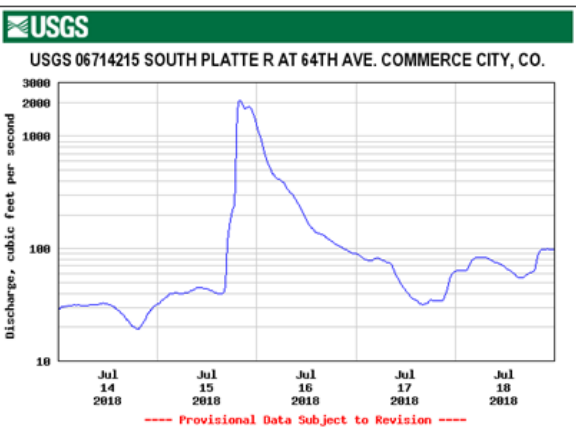
C) South South Platte



D) Cherry Creek at Denver, CO



E) North South Platte



F) Cherry Creek below Cherry Creek Lake

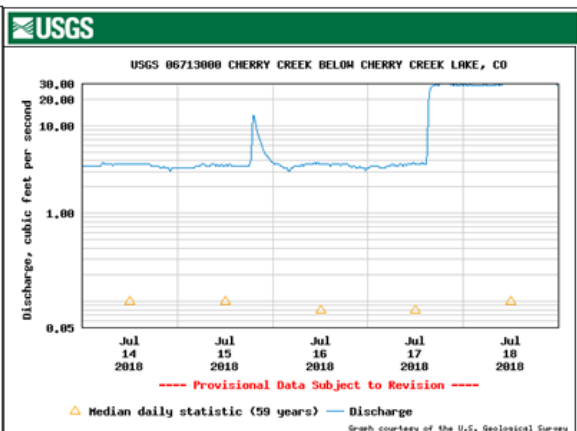


Figure 2-10 Hydrographs for selected sampling locations A) West Clear Creek, B) West Sand Creek, C) South South Platte, D) Cherry Creek at Denver, CO, E) North South Platte, F) Cherry Creek below Cherry Creek Lake.

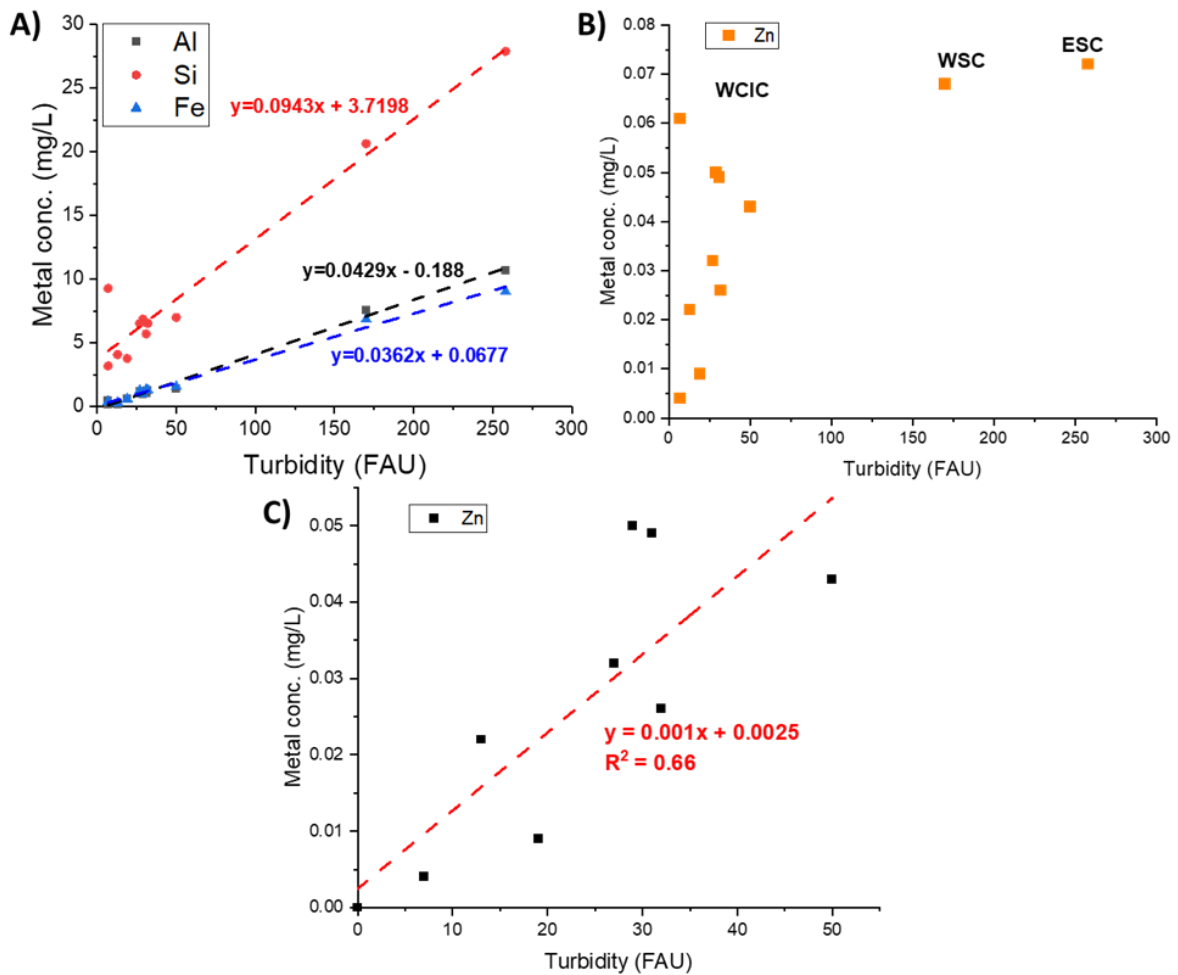


Figure 2-11 Turbidity plotted against various metal concentrations. A) Turbidity plotted against aluminum, silicon, and iron for all sample sites B) Turbidity plotted against zinc for all sample sites A) Turbidity plotted against zinc for all sample sites excluding WCIC, ESC, and WSC due to high flow conditions.

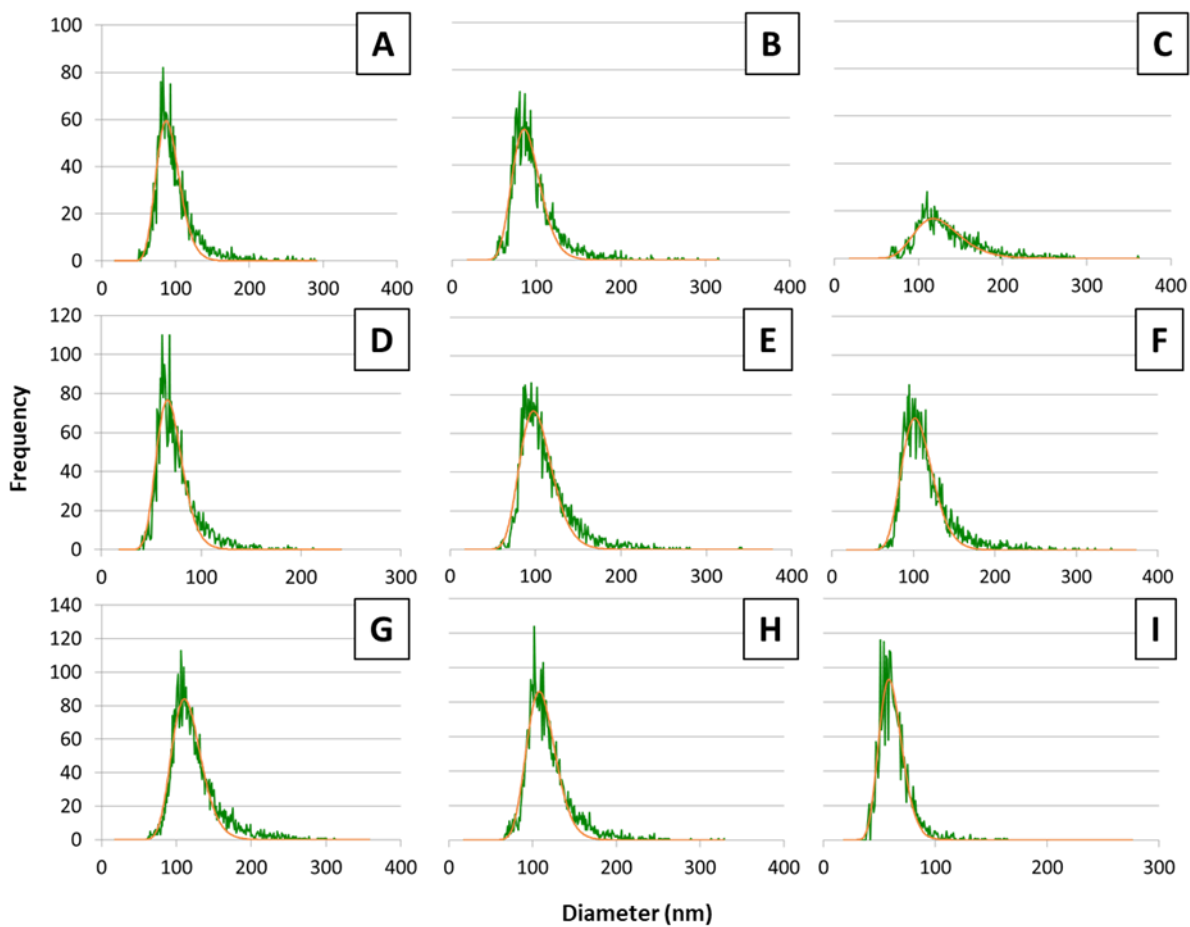


Figure 2-12 Size Histograms for sp-ICP-QMS measurements of raw samples. Panels correspond to sites: A. AWWTP; B. BWWTP; C. WCIC; D. SSP; E. NSP (7/16); F. ECIC (7/16); G. WSC; H. ESC; I. CC. Histograms for ECIC (7/17) and NSP (7/17) not shown. Diameter calculated by conversion of detected particle mass to a spherical metal Zn particle ($\rho = 7.14\text{g/cm}^3$).

CHAPTER 3 NOVEL METHODOLOGY FOR THE ANALYSIS OF POLYDISPERSE ENGINEERED AND NATURAL COLLOIDS BY SINGLE PARTICLE INDUCTIVELY COUPLED PLASMA SPECTROSCOPY (SPICP-MS)

A paper to be submitted to Environmental Science: Nano (Royal Society of Chemistry)

Beyers Shaun, Casey Smith, Howard Fairbrother and James F. Ranville.

3.1 Introduction

Nanomaterials (NMs) are operationally defined by their size (1-100nm in one dimension), and display unique sized-based properties that collectively govern the reactions in which they participate and to what degree[1]. The enhanced reactivity of NMs, as compared to their macroscopic counterparts, has led to the rapidly expanding field of nanotechnology, although some NMs (e.g. gold) have been used for millennia[140]. Nanomedicine utilizes NMs with defined size and surface functionality to target specific cells/tissues for imaging[141, p. 200] or drug-delivery[142]. Nanoencapsulation of nutrients and pesticides to control release rates increases crop productivity compared to application of their dissolved counterparts, creating the burgeoning field of nano-agriculture[13]. Natural NMs and incidental NMs (generated as a byproduct of human activity) are ubiquitous in the natural world[2]. The size-based reactivity of NMs makes them potent substrates in a wide variety of environmental processes despite their low mass concentrations relative to their macroscale and dissolved counterparts[2].

The size-dependent reactivity of engineered, incidental and natural NMs can lead to undesired environmental consequences. The oxidation state and speciation of both inorganic and organic dissolved species can be tied to the high specific surface area of NMs, which is a function of size[3], [143]. Smaller, more mobile NMs can facilitate the environmental transport of both organic and inorganic contaminants[143, p. 2], [144], [145], and micronutrients[146]. Nanoplastics (NPs: 1-1000nm), generated from weathering of microplastics (< 5 mm), are a distinct and newly recognized class of incidental NM[25] that have greater environmental mobility and higher bioavailability than microplastics[26]. Additionally, as a consequence of their high specific surface area, colloidal particles up to several microns are also a key component of environmental particle populations. Thus, to fully understand particle-mediated environmental processes, it is critical that accurate particle analysis and quantification be able to span orders of magnitude (nm – μ m).

Particle toxicology[147] is intimately tied to size, which is the principal determinant of particle ingestion[148] and cellular uptake[142]. Ultrafine aerosol particles (PM 0.1) are more toxic and persistent in human cells than their coarser counterparts (PM 2.5)[35], [37]. As a consequence of how reactive surface area scales with size, mass-based regulatory standards (mass/volume) for chemical exposures,

which are generally applied for the preservation of aquatic life and aerosol particle exposure[34], are inadequate when describing the dosage of NMs. Rather, particle number or surface area may be better descriptors of dose. Indeed, measurements of mass concentration can equate to vastly different particle number concentrations (PNC) depending on their size and polydispersity[35]. For these reasons, accurate measurement of PNC and particle size distribution (PSD) is essential to fully understand the ecological hazards and human health risks of NM exposure.

For monodisperse NMs, which often have a Gaussian size distribution of particle numbers, determination of PSD and PNC is relatively trivial using techniques such as dynamic light scattering[40], analytical ultracentrifugation[47], field flow fractionation[41], or single-particle techniques such as nanoparticle tracking analysis (NTA)[149] and single particle optical sizing (SPOS)[150, p. 200]. However, both natural and incidental NMs, as well as colloids, are generated through a wide variety of physiochemical reactions that typically produce broad, continuous PSDs that range over orders of magnitude[2]. Environmental particles have been shown to demonstrate size-dependent particle number distributions that often follow Pareto's Law (power law)[79]–[81]:

$$\frac{\Delta N}{\Delta D_p} = \alpha \left(\frac{D_p}{\Delta D_p} \right)^{-\beta} \quad (3-1)$$

where $\Delta N/\Delta D_p$ is the change in particle number with size, α and β are constants, and $D_p/\Delta D_p$ is particle diameter divided by the width of the size bin (ΔD_p). The constant α is a reflection of the magnitude of particle concentration and β describes the proportion of small to large particles (i.e. the PSD), and has been found to vary and reflect the mechanical, chemical and biological processes responsible for particle formation[81], [151]. Many of the aforementioned techniques are suitable for monodisperse particles but struggle to accurately size and/or count particles present in these continuous, polydisperse size distributions. Consequently, there is a need to develop new robust analytical approaches capable of accurately determining PSDs and PNCs for environmentally relevant NMs and polydisperse NPs.

Single particle inductively coupled plasma mass spectroscopy (spICP-MS) has seen increasing usage as a tool to characterize the PSD and PNC of metal-containing NMs and colloids[57], [65], [120], [152]. This technique takes advantage of the high elemental sensitivity and specificity of ICP-MS combined with a spray chamber that allows for the introduction of intact, individual particles into the plasma. Instrument response is continuously monitored, with 100 μ sec dwell times (i.e., integration time) commonly being employed. Particles are ionized, and the resulting ion clouds register as discrete bursts of signal on the MS detector, which when resolved from the constant background signal, enable the counting and sizing of individual, submicron particles. However, discrimination between background and particle signals is not simple and involves setting a threshold value, with signals above this value being counted and sized as particles. Threshold values are generally set as the mean (μ) plus a multiple of the standard deviation (σ)

for all measured signals. A threshold of $\mu + 3\sigma$ is widely used[120] and implemented in commercial analysis software, but other methods involving a variation of $\mu + x\sigma$ [76], [153] or modeling of background signal as a Poisson distribution have also been suggested[60], [154].

The smallest detectable mass of the element of interest is fundamentally determined by instrument sensitivity and the threshold. Conversion of this minimum mass to particle size requires assumptions about the mass fraction of the element in the individual particle, the particle density, and its shape[58]. High background signal, arising from dissolved elemental species, isobaric/polyatomic interference, or instrumental noise, increases the particle detection threshold, raising the lower limit of detectable particle size[63].

The upper limit of measurable particle mass fundamentally depends on two factors, ablation efficiency (AE), the ability of the plasma to completely ionize the particle, and transport efficiency (TE), the ability of the spray chamber to successfully aerosolize and transport the particle into the plasma. Both parameters decrease as a function of increasing particle size and density, leading to approximate upper limits of about 500nm for dense, recalcitrant silica particles[59] and 5 μ m for low density microplastic particles[64].

Possible analytical artifacts in spICP-MS arise from particle coincidence and aggregation[60], [155], [156], both of which lead to overestimates of particle size and underestimates of PNC. Coincidence arises when two or more individual particles are introduced in the plasma within the same dwell times, whereas aggregation represents the physical association of multiple particles. Both are related to total particle concentration, and thus increasing dilution directly reduces the probability of coincidence while also making aggregation less favorable.

Despite the increasing number of applications of spICP-MS for NM characterization, polydisperse samples by their nature remain difficult to characterize by spICP-MS. Given a possible power law distribution of particle numbers by particle size, there can be exponentially more small particles for every large particle present. High concentrations of the very smallest particles can form a high background of coincident particles, with the consequence that the detection threshold is increased, effectively obscuring the smaller size range of the PSD. Addressing the challenge of accurate PNC and PSD measurement for polydisperse samples in the presence of a particle-based background is the central focus of this work. We propose an approach of analyzing polydisperse samples using spICP-MS, where PSDs from multiple dilutions are compared to determine particle size ranges that contain analyzable data in which artifacts due to coincidence are absent. As our results demonstrate, data from coincidence-free regions can be combined across a series of dilutions to model the entire, broad PSD using a power law. The results generated by power law modeling of the PSDs using this new serial dilution approach are contrasted with a commonly used, single dilution spICP-MS data analysis[61], [67], [157]–[159]. To illustrate the benefits of this approach, we analyzed two types of environmentally relevant NMs: polydisperse, metal-doped NPs

which were used for method development; and Al-bearing NMs and colloids (i.e., silicate minerals) sampled during a storm event in the Denver Metro Area, CO USA.

3.2 Materials and Methods

3.2.1 Nanoplastic Synthesis.

We have prepared a broad library of metal-tagged model NPs for use in experiments to probe the effect of size on environmental behavior of NPs (C. Smith et al., JHU manuscript in prep). We have utilized two NPs from this library to develop the spICP-MS methodology reported herein. Polydisperse, model NPs composed of polyvinylpyrrolidone (PVP) or polymethylmethacrylate (PMMA) containing \approx 0.1 and 1% Ta by mass were manufactured for quantification by spICP-MS. To create these metal-doped NPs, neat polymer and organometallic additive (e.g. Ta(OC₂H₅)₅) were dissolved in an organic co-solvent (Methanol and Toluene for PVP and PMMA, respectively) to create a solution which was cast in an aluminum dish. The organic solvent was then evaporated, leaving a metal-tagged composite. MicroXRF (Bruker M4), performed in the Minerals and Materials Characterization facility (MMC) at the Colorado School of Mines demonstrated that this approach leads to a uniform distribution of metal within the composite (C. Smith et al., manuscript in prep). This uniformity enables the metal signal in spICP-MS to be used to compute the size of NPs produced by cryo-milling the composites (details in SI). Aqueous suspensions of NPs were prepared through addition of dry powder to nano-pure water; the suspensions were sonicated and then sieved (<35 μ m), producing stock solutions of polydisperse metal-tagged MPs.

3.2.2 Environmental NMs (Colloids).

Cherry Creek, a tributary of the South Platte River, originates southeast of Denver near Castlewood Canyon, CO, and is impounded in Cherry Creek Reservoir. Daily grab sampling (5/19/22-5/23/22) of Cherry Creek surface water was performed to capture a major precipitation event (5/20/22-5/22/22). The sampling site in Denver CO was roughly equidistant from the confluence with the South Platte River and Cherry Creek Reservoir (39°41'43.7"N 104°55'14.3"W). Continuous discharge data (Q, cubic feet per second, SI Figure 3.8) was obtained from the USGS (Gauge: USGS 06713500 CHERRY CREEK AT DENVER, CO). Further details can be found in SI.

3.2.3 Nano-analysis

Model NPs were imaged by scanning electron microscopy (TESCAN MIRA3 LMH Schottky field emission-scanning electron microscope (FE-SEM)) in the Minerals and Materials Characterization facility (MMC) at the Colorado School of Mines. Both model NPs and environmental NMs and colloids were analyzed by quadrupole spICP-MS (Perkin Elmer NexION 300D, Waltham, MA, USA) for ¹⁸¹Ta or ²⁷Al content, respectively. Measurements employed 100 microsecond dwell times, and size analysis utilized

the mass-based approach to determine transport efficiency[120]. TE was generally 5-8% throughout the study. Particle size was computed from the mass of ^{181}Ta or ^{27}Al detected in each particle, the mass percentage of this element in the particle, and the particle density. The ^{27}Al content of K-Feldspar, a common detrital mineral, was used to estimate particle size for the river NMs and colloids. Additional details of data collection and analysis are provided in the SI.

3.3 Results and Discussion

3.3.1 Particle-Generated Background in Polydisperse Samples

As previously noted, accurately measuring sample PSD by spICP-MS revolves around finding a dilution that successfully minimizes particle coincidence. For monodisperse samples whose mean size is well above the threshold, the effects of particle coincidence on experimentally determined size and number can be easily identified across the measured PSD (see example in SI Figure 3.9). Using monodisperse standards as a basis, Laborda et. al.[60] has suggested that nanoparticle and colloidal samples can be characterized at a single dilution that depends on the spICP-MS measurement conditions (nebulization efficiency, sample flow rate, dwell time, total acquisition time). For the conditions used in this study, this equates to ≈ 4000 particle events counted per analysis. Such an approach works well for relatively monodisperse (normally distributed) samples.

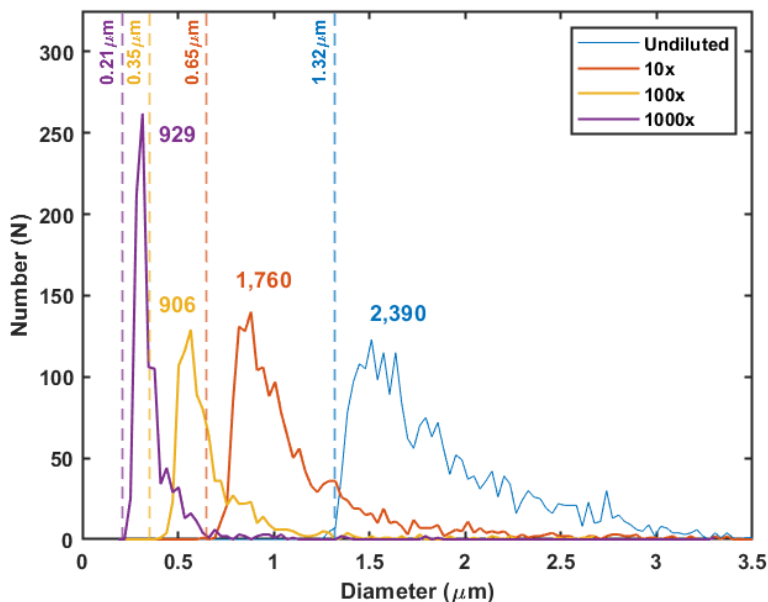


Figure 3-1 PSDs of 10-fold serial dilutions of a 0.1% Ta-Ethoxide Polyvinylpyrrolidone (PVP) suspension (Undiluted Nominal Concentration: 10.1mg/mL PVP). Threshold size (dashed line) and the particle no. detected (bold number) for each dilution is indicated. Detected particle number was not corrected for dilution. Particle diameters reflect a conversion of the measured mass of ^{181}Ta to an equivalent diameter of a PVP particle based on the (0.1 %) loading of Ta-Ethoxide and the polymer density (1.2 gm/cm^3).

Polydisperse samples such as our model NPs and natural stream particles, with particle numbers distributed over a broad continuum of sizes, pose a much greater challenge to accurate PSD/PNC measurement via a single dilution. For example, PSDs measured over serial 10x dilutions (ranging from undiluted to 10^3x) for a dispersion of 0.1% (w/w) Ta-Ethoxide doped PVP plastic NPs are shown in Figure 3.1. Clearly the reported PSD is influenced by dilution. The clearest indication of a coincidence-induced artifact is the change in the minimum observable size of the PSD. The threshold particle size ($\mu + 3\sigma$) of the undiluted sample was $1.32\mu\text{m}$. At the maximum dilution this is reduced to $0.21\mu\text{m}$, which also represents the minimum possible detectable size given the 0.1% Ta-Ethoxide loading of the plastic.

PNCs are affected by dilution as well, with increasing PNC as dilution is increased. In the undiluted and 10x dilutions, 2,390 and 1,760 particles were counted respectively, demonstrating that an additional 1,521 particles were measured over the 239 that were expected to result from the 10x dilution. Thus, total particle number did not decrease proportionally with a 10x dilution, and subsequent dilutions follow this same trend of showing “excess” particles at each step. Clearly not all of the particles are being counted in the more concentrated samples. In a well-behaved system bereft of coincidence, particle numbers should scale linearly with dilution and the PSD should remain constant. In the case of these polydisperse Ta-PVP NPs, the reason for the non-linear scaling in particle numbers can be attributed to experimentally determined threshold values being greater than the theoretical value of $0.21\mu\text{m}$. This artifact is a result of coincident small particles that elevate the thresholds. As the dilution increases, the probability of coincidence decreases, and the threshold drops. Consequently, smaller particles become observable, and are now counted as individual particles, causing the experimentally observed PNC to increase. Additional evidence of an elevated background arising from coincidence is the absence of a detectable ^{181}Ta signal following 0.02μ filtration of the undiluted sample. This observation supports the conclusion that the thresholds greater than $0.21\mu\text{m}$ are generated by coincident nanoparticles and not a consequence of ionic ^{181}Ta or small, undetectable NPs ($< 0.02\mu\text{m}$).

The observation of increasing particle numbers and changing observable particle size as a function of dilution-induced threshold reduction is characteristic of a particle-based background. In contrast, for a threshold derived from dissolved ions, it should be possible to find a dilution where the background is reduced to a point where pulses generated by the smallest particles can be resolved and quantified. For this Ta-doped PVP suspension, proportional dilution of total particle number never occurs, as shown by the nearly equal particle numbers (906 and 929) measured in the two highest dilutions: 10^2x and 10^3x respectively. This observation indicates that coincident particles smaller than the theoretical value of $0.21\mu\text{m}$ are present. Further dilution may achieve proportional dilution, but PNCs would be very low. Numerous studies have been dedicated to the resolution of particle signals from a background composed of dissolved ions, but few have discussed the presence of a background composed of coincident particles[69]. Although each dilution (Figure 3.1) comfortably has <4000 events, a criterion that has been

suggested in the past[60], [130] as necessary for avoiding coincidence in mono-dispersed samples, our results suggest that this criterion may not extend to highly polydisperse samples.

Our results (Figure 3.1) highlight that while dilution can successfully lower the threshold, it concurrently reduces counting statistics for the largest particles, drastically limiting the upper range of observable particle size, particularly at the high dilutions needed to quantify the smallest particles. Finding a single, perfect dilution that maximizes measurement range while minimizing the particle coincidence may not be feasible in highly polydisperse samples. Techniques such as hydrodynamic chromatography (HDC)[136, p. 201] or field flow fractionation (FFF)[62] have been used in combination with spICP-MS to provide physical separation by particle size. Feasibly, this would allow for the separation and quantification of any particle-based background, but in practice both techniques greatly dilute the injected sample, resulting in insufficient particles to count during spICP-MS.

3.3.2 Making Use of Imperfect Data: Power Law Modeling

As demonstrated by Figure 3.1, coincidence is a major concentration-induced cause of PSD distortion in spICP-MS that results in PNC undercounting and an erroneously higher PSD due to the summation of coincident particle masses. Furthermore, these distortions are more likely to occur in the lower region of the PSD (Figure 3.1) as the smaller particles are found at much greater concentrations in polydisperse samples. Moreover, the effect on the measured particle mass is increased proportionately more when two small particles are coincident than when one or more small particles are coincident with a much larger particle.

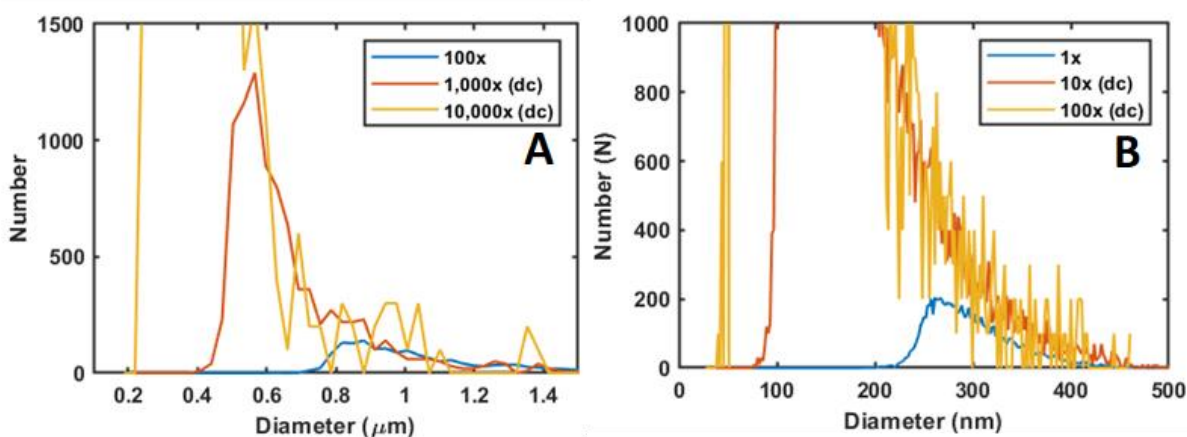


Figure 3-2 Dilutions of a 0.1% Ta-Ethoxide PVP suspension (nominal initial concentration of 88 mg/L PVP) (Panel A) and an Al-containing environmental colloid (Panel B) sampled from Cherry Creek, Denver CO on May 20th 2022. Particle diameters reflect the equivalent size of PVP particles given the loading of Ta-Ethoxide (Panel A) or the equivalent size of K-Feldspar given the percent composition of Al (Panel B). For each dilution the particle numbers were normalized to lowest dilution (100x), denoted by (dc: dilution corrected).

Figure 3.2A shows the PSD of three different dilutions of a 0.1% Ta Ethoxide PVP suspension where the particle numbers of the two higher dilutions are normalized to the lowest (10^2 x) dilution factor. With each dilution, increasingly smaller particles are uncovered because the threshold decreases, showing that the functional form of the PSD is sensitive to the dilution. Examining the PSD of the three dilutions, it is apparent that there are, however, regions of disproportional and proportional dilution. For example, between particle diameters of 0.9-1.5 μm , the dilution-corrected particle numbers of all three dilutions agree, demonstrating that in this size regime there is proportional dilution of particle number. In contrast, at particle diameters 0.75-0.9 μm , the dilution corrected particle numbers of the 10^3 x dilution do not agree with those of the 10^2 x dilution, which is attributable to the combined effects of the coincidence in the smaller size range of the 10^2 x dilution PSD and the higher threshold. Agreement is seen between the 10^3 x and 10^4 x dilutions above 0.5 μm , but a lower detectable size limit of about 0.4 μm in the 10^3 x dilution is apparent.

The dilution-corrected PSD for an Al-bearing colloid sampled from Cherry Creek, Denver CO USA (Figure 3.2B) illustrates another facet of this type of analysis. Unlike the previous example, no portion of the dilution-corrected PSD of the 10^1 x and 10^2 x dilutions overlap with the undiluted sample, suggesting that the entire PSD measured for the undiluted sample is coincident. This conclusion is supported by similar effects seen in monodisperse samples at high concentrations where coincidence and aggregation distort the entire PSD (SI Figure 3.9). In contrast, over a range of particle sizes spanning 0.2-0.5 μm , the dilution-corrected particle numbers of the 10^1 x and 10^2 x dilution of this Al-bearing colloid agree, suggesting the absence of concentration-dependent effects within this region. In other words, these overlapping regions between different dilutions where the dilution-corrected particle size distributions are coincident can be considered “artifact-free” and undistorted either partially or wholly by coincidence and/or aggregation. The identification of these regions is the essence of our new approach and is the necessary step towards finding the “artifact-free” PSD and PNC for a polydisperse sample.

Using this approach, we can use multiple dilutions to identify regions of the PSD in each dilution where particle numbers are proportionally diluted and thus are free of coincidence. As shown in Figures 3.1 and 3.2, this results in each dilution representing a different viewing window into the “artifact-free” PSD. Ideally these windows can be combined into a larger picture of the “artifact-free” PSD over all measured particle size ranges across all dilutions.

The power law model of particle number versus particle size (Equation 1) has been successfully used in the past to model polydisperse PSDs in natural samples[79], [80]. In this model, particle number is a function of particle diameter raised to a constant β , which itself is related to the distribution of particle numbers across the measured PSD (i.e. the proportion of small to large particles). The constant α is related to the total number of particles in the sample (i.e. PNC). Although power law models have been applied to data from other particle sizing techniques[80], [160], [161]it was only recently applied to

modeling spICP-MS measurements of mineral dust aerosols[69]. In the current case of the metal-tagged NPs, we use the power law to model polydisperse PSDs across a range of dilutions so that its shape and PNC can be compared independent of particle-generated thresholds at each dilution (Figure 3.1) and particle coincidence (Figure 3.2B).

The power law relationship (eq 1.) is linearized by log transformation, resulting in:

$$\log N = \log \alpha + \beta \log D \tag{3-2}$$

A plot spICP-MS data as the log of particle number, N , versus the log of particle diameter, D , will therefore have a slope of β and a y-intercept of $\log \alpha$. The value of α increases in response to increasing PNC. For these spICP-MS datasets, bin size was consistently 1nm so the term ΔD_p from Eqn. 1 can effectively be ignored.

3.3.3 Determining the “Artifact-Free” Size Distribution of Metal-Tagged NPs

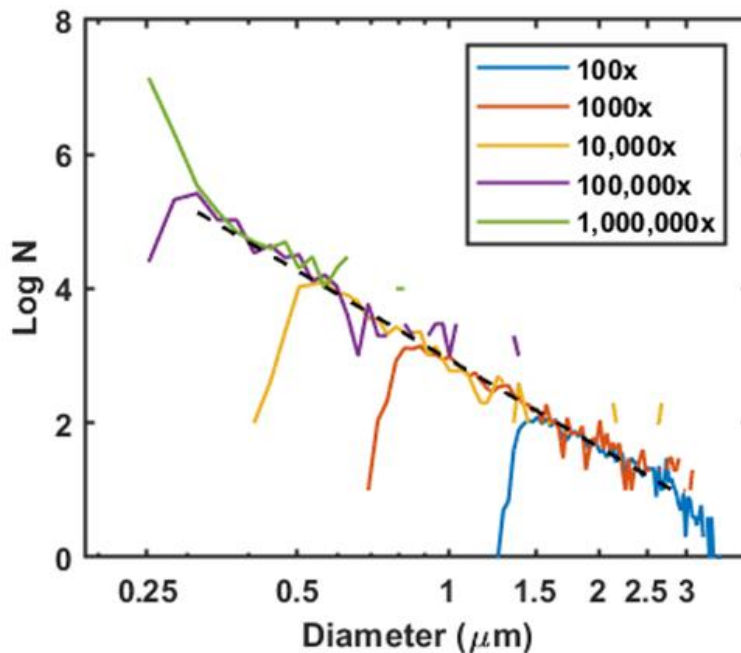


Figure 3-3 Log-log plot of PSD for 10-fold dilutions ($10^2x - 10^6x$) of a 0.1% Ta-Ethoxide PVP suspension using spICP-MS (nominal undiluted concentration: 8.8g/L). Higher dilutions were normalized to the original 10^2x dilution. The model (black dashed line) is the linear regression of the power law model of particle number vs particle diameter (see text for details).

We employed the power law analysis approach for spICP-MS data of metal tagged NPs. A log-log plot for a dilution series of 0.1% Ta-Ethoxide PVP suspended NPs (Figure 3.3) shows both rapid change in particle number near the threshold as well as regions of proportional dilution, the latter being the regions of each dilution’s PSD that is free of distortion (i.e., “artifact-free” PSD regions). The “artifact-free” PSD regions specifically identified for dilutions of 10^5x , 10^4x , 10^3x , and 10^2x were: 0.31-0.76μm,

0.76-1.13 μm , 1.13-1.57 μm , and 1.57-2.8 μm , respectively. The PSDs from each of these dilutions were combined, creating a “artifact-free” PSD spanning particle diameters of 0.31 – 2.8 μm . The lower limit of PSD used from the 10⁵x dilution, 0.31 μm , was derived from the overlap in dilution corrected PSD between the 10⁵x dilution and a 10⁶x dilution. No data from the 10⁶x dilution was incorporated into the power law fit as there was no higher dilution with which to compare.

Given the fidelity of the linear relationship between particle number and size on the log-log plot for particle sizes ranging from 0.31 – 2.8 μm across the dilution series ($R^2 = 0.982$), it suggests that the power law should continue beyond 2.8 μm in particle diameter. However, this regime cannot be quantified by spICP-MS because decreasing particle transport efficiency into the spICP-MS results in undercounting at sizes >2.8 μm . The specific particle size at which transport efficiency begins to affect the PSD measured by spICP-MS depends on the particle’s physical properties such as density and surface hydrophobicity. Previously, a transport efficiency of 0.04% was reported for more hydrophobic 2.5 μm -diameter PS beads using a cyclonic spray chamber[66] but in the present study the linear relationship between particle number and diameter continues from 2.5-2.8 μm , suggesting somewhat efficient transport of hydrophilic PVP particles <2.8 μm in diameter. It should be noted that ablation efficiency is not expected to affect the PSD measured in this experiment as previous studies have shown complete ablation of plastic microspheres up to 5 μm in diameter[64], significantly larger than any of the particles analyzed in the present study.

Linear regression of the combined PSDs presented in Figure 3.3 resulted in values of 4.956 and -4.5638 for $\log \alpha$ and β , respectively, and a power law model relating particle number to particle diameter of:

$$N = 10^{4.956} D^{-4.5638} \quad (3.3)$$

Residuals of the linear regression of the log-log plot fit (SI Fig 3.10) show no systematic, size-dependent deviation, suggesting that a log-log plot of the combined dataset is well modeled by linear regression. The high, negative β value reflects a broad size distribution with a high proportion of small to large NPs. Using equation 3 to replot the power law model over the original PSD data set for three dilutions shows good agreement (SI Figure 3.11). Given these results, we believe that the power law successfully models the relationship between particle number and particle diameter for this suspension of mechanically generated, metal-tagged PVP NPs.

3.3.4 β Values Reflect Physical Characteristics of the Measured PSDs

A central question regarding the β value is whether it reflects a difference in physical properties between two sample populations, as measured through the shape of their PSDs. Both the PVP (1% (w/w) Ta-Ethoxide) and PMMA (0.1% (w/w) Ta-Ethoxide loading) model NPs were created through the same casting, cryo-milling, and sieving processes, but due to their different mechanical properties, the resulting

NPs were expected to have different PSDs[162], [163]. The results of four dilutions of a 1% Ta-Ethoxide PVP suspension, and two dilutions of a 0.1% Ta-Ethoxide PMMA suspension are presented in Figure 3.4A and 3.4B, respectively.

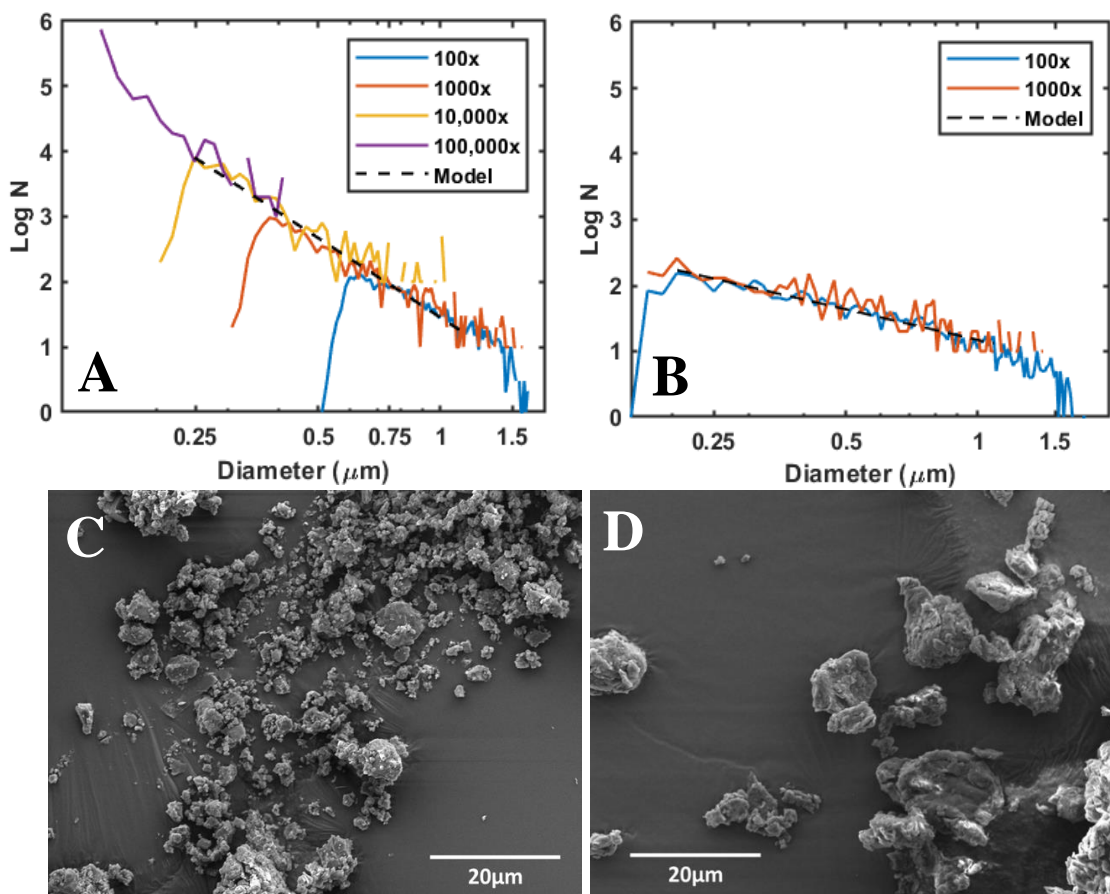


Figure 3-4 Log-log plots of (10^2 - 10^5 x) dilutions of a 1% Ta-Ethoxide PVP (Panel A), and 10^2 x and 10^3 x dilutions of a 0.1% Ta-Ethoxide PMMA suspension (Panel B). For each dilution the particle numbers were normalized to lowest dilution. SEM micrographs of the dry 1% Ta-Ethoxide PVP (Panel C) and 0.1% Ta-Ethoxide PMMA powder (Panel D) mounted on carbon tape and sputter coated with Au.

Utilizing the overlapping PSD regions from three dilutions (10^2 - 10^4 x) of the PVP suspension, linear regression of $\log N$ versus $\log D$ yielded values of -4.06 ± 0.09 and 3.45 ± 0.02 for β and $\log \alpha$, respectively ($R^2 = 0.974$). From the overlapping PSD regions of the two PMMA dilutions, values of -1.55 ± 0.06 and 2.17 ± 0.02 for β and $\log \alpha$, respectively, were obtained ($R^2 = 0.916$). The more negative value of β for the PVP (-4.06) compared to the PMMA (-1.55) indicates that particle numbers increase more rapidly with decreasing size for the PVP suspension. This lower β (i.e. a lesser increase in the proportion of small to large particles) for the PMMA is consistent with near complete overlap between the

dilution corrected $10^3\times$ and $10^2\times$ PSDs across the entire particle size regime. Further dilution of the PMMA was not possible due to low overall PNC in the undiluted suspension, although the overlap between the two dilutions suggested no further dilution was necessary. SEM micrographs qualitatively support the inference from spICP-MS that the PVP sample shows proportionally larger numbers of smaller particles as compared to the PMMA sample. Thus, the average size of particles in the SEM micrographs is clearly larger for the PMMA compared to the PVP NPs. It should be noted that the SEM images depict particles larger than the upper measurement range of the spICP-MS, but the relative trend in particle number as a function of particle size can reasonably be expected to extend to larger particle sizes given the success of the power law in modelling the PSD for PVP and PMMA in the size regime accessible to spICP-MS.

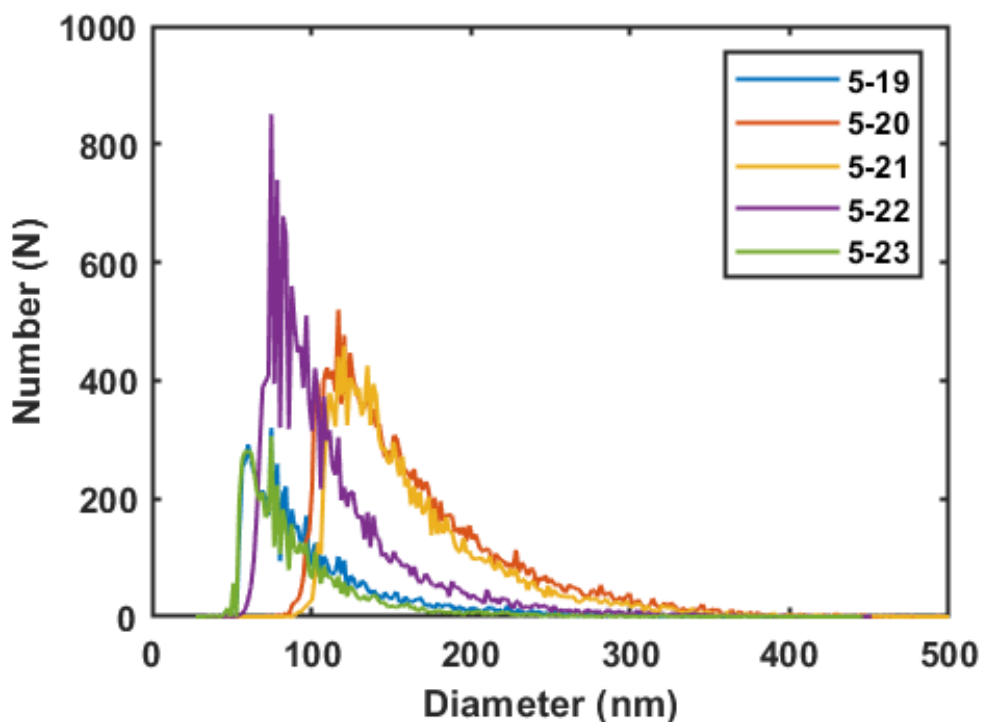
Log α values for the PVP and PMMA, 3.45 and 2.17 respectively, suggest that there are roughly 10 times the number of PVP particles in solution compared to the PMMA. This is supported by the observation that the spICP-MS data for both the $10^2\times$ and $10^3\times$ dilutions of the PMMA have the minimum threshold of 1 count (threshold size: 0.22 μm), suggesting that there is no particle-based background present. In contrast, the dilutions PVP suspension has threshold sizes ranging from 0.54-0.1 μm that decrease with the level of dilution, suggesting the presence of a particle-based threshold. The presence of this particle-based background supports the observed differences in α that indicate the PVP suspension has a higher number of particles in solution than the PMMA. Thus the “artifact-free” PNC may be approached at the higher dilutions, but low counting statistics make the results less certain. Moreover, our results suggest that β and α values reflect real, physical differences between these two NP samples and may be used to compare their PSDs and PNCs.

Overall, we have shown that for these metal-tagged NPs in a series of serial dilutions, regions of usable, non-coincident (“artifact-free”) data from each concentration-dependent PSD can be identified, combined and modeled to create a global fit of the overall PSD. In this manner, a polydisperse sample can be analyzed, preserving information about the number distribution at larger sizes while simultaneously using higher dilutions to reduce threshold and accurately measure the lower end of the total size distribution. Functionally, this extends the size range of spICP-MS analysis roughly 10-fold compared to that measured in a single dilution. Furthermore, the method produces both β , describing the shape of the PSD across the entire measured size range, and α representing the total particle concentration distributed across all sizes.

3.3.5 Changes in PSD/PNC of Al-bearing Stream Particles During a Storm Event

Having demonstrated the utility of serial dilutions to determine “artifact-free” PSDs for metal-tagged NPs, we show how this improved methodology can change our interpretation of data acquired on the resident particle populations in stream water during a hydrological event. The power law observed in

natural colloids[79] and our results for the metal-tagged NPs support our view that unless a careful dilution study is made, background size cut-offs at any single dilution are likely impacted by the coincidence created by large numbers of small particles present in natural waters. As a result of this high concentration of small particles, coincidence effects will distort the PSD and PNC determined by spICP-MS, which will go undetected in a more conventional, single dilution spICP-MS approach. To demonstrate the existence of this issue, we illustrate how conclusions regarding environmental processes in our stream study can be very different when using the comprehensive multiple dilution and single-dilution spICP-MS[61], [67], [157]–[159] approaches. In our example, Al-containing NMs and colloids were sampled from Cherry Creek, Denver CO USA (5/19/22 – 5/23/22) where storm discharge (Q, cfs) increased by as much as 10-fold (SI Fig 3.8).



<i>Sampling Date</i>	<u>5/19</u>	<u>5/20</u>	<u>5/21</u>	<u>5/22</u>	<u>5/23</u>
<i>Threshold (nm)</i>	17	29	34	20	21

Figure 3-5 spICP-MS results for a single 10^2 x dilution (all dates) of Al-bearing colloids collected from Cherry Creek, CO USA across a major storm event. The table shows the calculated threshold particle size for each sample. Particle diameters reflect a conversion of the detected Al mass to the diameter of an equivalently sized K-Feldspar particle.

Figure 3.5 shows spICP-MS PSD analysis of the different samples collected across this major storm event and measured at a single dilution (10^2 x). Particle size detection thresholds are displayed in a table below the figure. Two of the samples, 5/20 and 5/21, show particularly high thresholds compared to the

other samples, suggesting the presence of a coincident particle background at this dilution (Fig 3.1). As a point of comparison, we also measured PSDs at different dilutions to create overlapping size-distributions (example given in Figure 3.6), thereby generating “artifact-free” PSDs and power law models that avoid distortion by particle coincidence.

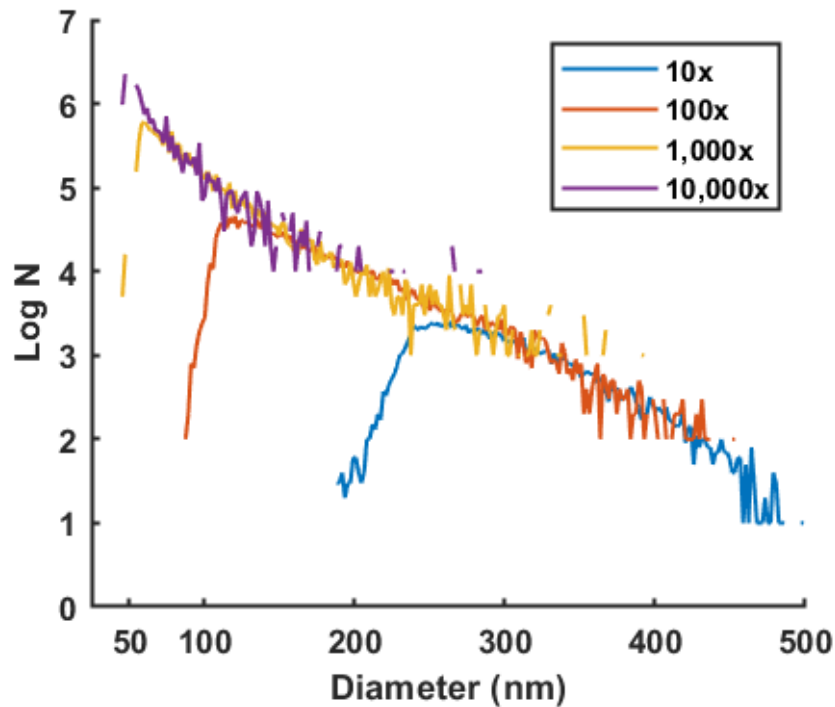


Figure 3-6 Example log-log plot (5/21 data) used for power law analysis of Cherry Creek storm samples. Particle numbers are corrected for the dilution factor.

Analysis of Storm-Influenced Stream Particle Populations: Using Serial Dilutions. Log-transformed PSDs from a dilution series of each of the five dates (Figure 3.14) were modeled to determine β and $\log \alpha$ values for each sample collected during the event. Data from two dilutions (5/19, 5/22 and 5/23 samples), or three dilutions (5/20 and 5/21 samples) were combined to generate a power law model for each sample (SI Table 3.4, SI Figures 3.13, 3.14). An example of this analysis is shown in Figure 3.6. Only two dilutions were used for the 5/19, 5/22 and 5/23 samples as low PNC made it impossible to dilute the sample more than 3 orders of magnitude and still count sufficient particle numbers. Figure 3.14 demonstrates that regions of “artifact-free” PSD data were identified for each of the samples and by regression analysis this data, we show that a power law relationship does indeed describe the PNC for all sampling dates. $\log \alpha$ values (Fig 3.7a) indicate that PNC increases with storm discharge (Q , cfs), peaks at 11 commensurate with maximum Q (119 cfs) and remained elevated post-storm (5/22, 5/23) compared to the pre-storm (5/19) PNC value. β values (Fig 3.7b) become more negative with increasing discharge, reaching a minimum, -3.97, at maximum Q , and remain suppressed post-storm compared to pre-storm.

This decrease in β indicates that the elevated discharge during the storm is preferentially mobilizing smaller-sized (fine) particulates as compared to those mobilized by the constant discharge pre-storm.

Taken together, these power law relationships and their associated $\log \alpha$ and β values measured herein support a simple model for how the characteristics of the particle population are driven by Q . On the ascending limb of the hydrograph (5/19-5/21) a strong linear relationship is observed between $\log \alpha$ and Q . During this period β becomes more negative but the relationship is not as strongly linear. On the descending limb (5/21-5/23) a generally opposite trend is observed but changes in α and β are not as linear with respect to Q . In other words, storm mobilized particulates are both greater in number and included a higher proportion of small particles compared to pre-storm, with some elevated amounts of material being transported by the waterway post-storm.

Analysis of Storm-Influenced Stream Particle Populations: Traditional Single Dilution spICP-MS Analysis. A traditional spICP-MS analysis typically focuses on reporting PNC and mean particle diameter (e.g. Figure 3.6), and is often obtained from a single dilution. A potential problem with this type of analysis may occur when particle concentration varies among different samples (e.g. acquired in our case at different points along the storm's progression) to the point that unequal thresholds are present. This would result in PNC and PSD that are inconsistent within the sample set. To illustrate that this potential issue is operative for our river study, we analyzed data from only the 10^2 x dilution (Fig 3.5a) to determine PNC (Fig 3.7c) and mean particle diameter (Fig 3.7d). Reported mean particle diameter and PNC increased with Q , peaking at 164nm and 9.5×10^5 part/mL, respectively, at the second highest Q (90cfs). PNC (Fig 3.7c) values decreased at maximum discharge, remaining near constant post-storm (5/22), before ending at a value lower than measured pre-storm. This pattern thus shows only a weak dependence of PNC on Q , which is contrary to reasonable expectations given the introduction of particles from surface runoff and sediment resuspension during the storm. Mean particle size follows a similar trend, increasing commensurate with discharge, but with little difference during the storm (5/20 and 5/21), before falling off as discharge returns to pre-storm levels. As discussed previously, the elevated thresholds of the 10^2 x dilutions of the 5/20 and 5/21 likely arise from coincident small particles in these samples and cause a distortion in the measured PSDs and PNCs in the 10^2 x dilutions.

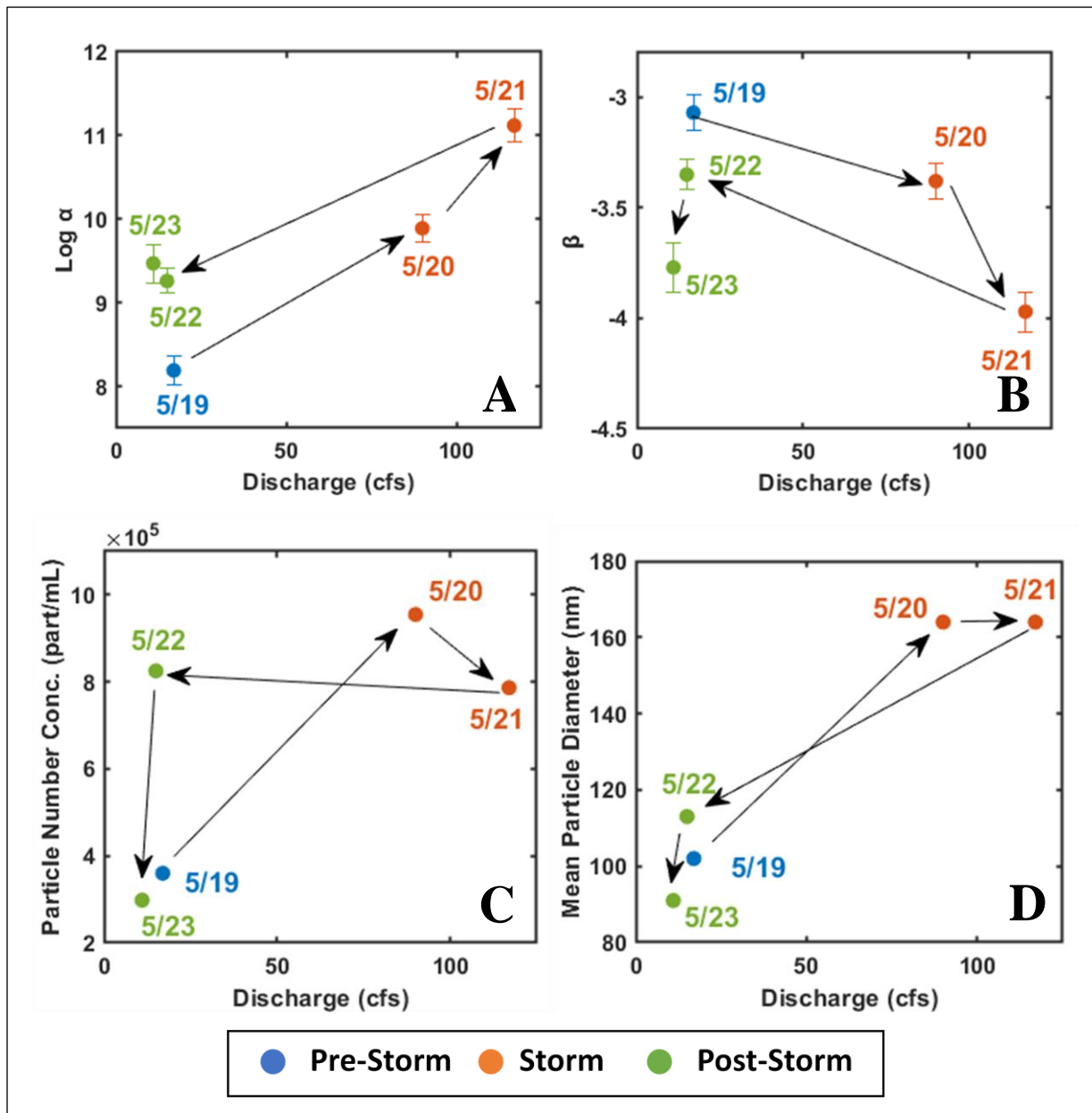


Figure 3-7 (a) Log α values and (b) β values were derived from the power law modeling of a dilution series for each date (data in SI). (c) PNC acquired from a single dilution ($10^2\times$) across all samples (d) mean particle size acquired from a single dilution ($10^2\times$) across all samples. Arrows show the temporal relationships among the samples and sampling dates of each data point labeled in panels (a-d).

Comparison of PNC vs Log α . Log α values obtained from the power law analysis using serial dilutions reflect particle number and therefore can be meaningfully compared to the PNC data acquired using a single dilution. Comparing trends in the log α values and the PNC measured from a single dilution, log α peaks with peak Q (117cfs), while in contrast, PNC peaks during a day earlier at the second highest Q (90cfs). The behavior in PNC obtained from the single dilution is contrary to the expectations of particle introduction from surface runoff and sediment resuspension accompanying the storm.

Resuspension of bed sediments and influxes of material from neighboring terrain should be maximal at maximum discharge. Additionally, PNC returns to a final post-storm value lower than pre-storm value which is also unlikely to reflect the actual situation, because PNC numbers would be expected to return to close to pre-storm levels. These differences in PNC behavior with respect to Q are likely artifactual and can be attributed to under-counting of the smaller particles in the 10^2 x dilution of the 5/21 and 5/23 samples as a result of particle coincidence.

The issue with the single dilution measurements is also evidenced by the observation that the PNC obtained by a single dilution only varies within about an order of magnitude across all dates even though variation in $\log \alpha$ suggests particle number concentration varies by > 4 orders of magnitude (SI Table 3.4). This insensitivity to PNC for the single dilution analysis can be rationalized by recognizing that as the storm progressed, the fine particles that are being introduced lead to increased particle coincidence. As a result, the true difference in PNC across the samples are obscured in the 10^2 x dilutions due to varying levels of particle coincidence. This makes it clear that the power law modeling, which necessitates the identification and exclusion of data distorted by particle coincidence using serial dilutions, allows for a more accurate accounting of PNC variation in these measured samples.

Comparison of Mean Particle Size to β . Mean particle diameter values obtained from single dilution data and β values (which reflects particle size distribution) obtained from serial dilutions show opposite trends. Thus, β values obtained from serial dilutions decrease with increasing discharge (Fig 3.5b), revealing that the proportion of small to large particles is increasing over the course of the event and persists post-storm. In contrast, the mean particle diameter, measured from the single 10^2 x dilutions of each sample (Fig 3.5d), increased with discharge before plateauing and ending at smaller value than pre-storm. Again, the difference in trends between the two analytical approaches can be attributed to the effect of coincidence on the particle-based backgrounds in the 5/20 and 5/21 samples. This unwanted effect causes an erroneous undercounting of the smaller-sized particles, whose omission skews the mean particle diameter to artificially higher values in the single dilution analysis. Using β values from serial dilution measurements which are free of distortion due to particle coincidence provides a more accurate assessment of the PSD as well as changes to the proportion of small to large particles between samples. Moreover, the availability of accurate particle size and number from serial dilution experiments also improves estimates of total colloidal mass and surface area. For example, for the 5/23 sample, using a single dilution for spICP-MS analysis results in an underestimation of total mass in particles by 22% and total particle surface area (assuming a spherical shape) by 23% compared to the power law model for the same sample, acquired using the serial dilution method developed in this manuscript.

3.4 Conclusions

Nanoparticles and colloids are important components of natural and human-impacted environments, with size playing an influential role in their environmental reactivity, fate, and transport. Key particulate classes include natural (e.g. clays, metal oxides), incidental (soot, tire wear, nanoplastic), and engineered (gold, quantum dots). The processes that generate and transport nanoparticles and colloids also result in broad size distributions. Accurate measurement of PSD that span orders of magnitude (nm to micron) is critical to our understanding of their behavior. Our proposed analysis methodology is advantageous in that particle numbers and PSDs are corrected for the deleterious effects of particle coincidence, especially at the smallest region of the PSD, by combining data from multiple dilutions.

As an illustrative example of where improved information on PSD and PNC matters, consider particle toxicity which depends on the properties of the nanomaterial in question, but also requires an accurate particle number for calculating dosage, and subsequently evaluating a nanomaterial in a toxicity assay. Total particle mass, measured through filtration or other bulk means, is an incomplete measure of PNC as a given mass could contain a wide range of particle concentrations depending on particle size. Without an accurate measurement of particle number and thereby particle dose, the relative toxicity of nanomaterial cannot be compared to another toxicant. For example, consider the characterization of aerosolized ultrafine (PM_{0.1}) particles, which are of concern to a fields as diverse as human health[37] and climate science[35]. These particles exist transiently at high, local concentrations making particle coincidence likely in their measurement, rendering particle number difficult to accurately to assess.

Techniques such as SPOS[164] or time-of-flight single particle mass spectrometers[165] struggle with coincidence in a similar manner to spICP-MS leading to the exclusion of data taken at high particle concentrations and use of high dilutions in routine analysis. As we discussed previously, these high dilution factors lead to a degradation of particle numbers measured for lower abundance, larger particles. The methodology proposed herein could be used similarly for data obtained using other single particle methods in order to identify coincidence-distorted data in samples with high total particle numbers. Furthermore, as demonstrated by the storm colloids in this manuscript, employing our methodology can lead to more accurate determination of particle number over a wider size range for high concentration samples.

Lastly, power law modeling has been undertaken in the past for the purposes of modeling aerosol, freshwater and marine colloids[79], [160], [166]. Single particle ICP-MS can often detect and size particles smaller in size than many other single particle techniques. By combining this sensitive technique with power law modeling, we can measure size distributions that are independent of the technique itself and can be compared to power law models derived from alternate techniques. For example, the influence of discharge on the β and $\log \alpha$ values determined for the storm-colloids in this study showed reasonable agreement with those calculated for larger 2-13 μ m particles during similar short-term, high-discharge

events measured with by a light-blocking laser particle sizer[161]. Combining the data of a particle sizer such as SPOS to measure larger particles with that of spICP-MS[69] can extend the characterizable size range and enhance our understanding of the entire colloidal population.

3.5 Acknowledgments

This work was supported by the National Science Foundation (Grant No. 2003481). We would like to acknowledge Aaron Goodman for his insights into power law relationships and spICP-MS methodology, as well as Stephanie Brown and Nathan Malone for their assistance in the metal-tagged nanoplastic synthesis. Additionally, the SEM and μ XRF measurements were performed in the Minerals and Materials Characterization Facility at Colorado School of Mines with the assistance of Dr. Katharina Pfaff and Kelsey Livingston.

3.6 Coauthor Contributions

Casey Smith and Howard Fairbrother carried out the nanoplastic synthesis at John Hopkins University. James F. Ranville was involved in the preparation of this manuscript and supervised the work.

3.7 Supporting Information

3.7.1 Sampling Campaign

Cherry Creek originates southeast of Denver near Castlewood Canyon, CO, and is impounded in Cherry Creek Reservoir. Flow is principally a function of release from Cherry Creek Reservoir, along with notable spikes in discharge corresponding to major precipitation events, and cuts through urban tracts of Denver, CO. Eventually the creek feeds into Denver's primary water source, the South Platte River, near downtown Denver, CO. Typical flows along Cherry Creek vary from 15-30cfs across the year with peak flows due to mountain snowmelt coming in Mar-Jul.

Daily grab sampling (5/19/22-5/23/22) of Cherry Creek surface water was performed to capture a major precipitation event (5/20/22-5/22/22). The sampling site in Denver CO was roughly equidistant from the confluence with the South Platte River and Cherry Creek Reservoir (39°41'43.7"N 104°55'14.3"W). Water was collected near the center of the channel using a 2-m pole sampler (HDPE) and transferred to 1L HDPE bottles for storage. Both the bottles and pole sampler were triple rinsed with water from the stream prior to collection. Streamflow was obtained from the USGS gauges at the confluence between the South Platte River and Cherry Creek (USGS Gauge ID 06713500) and the gauge along Cherry Creek at Cherry Creek Reservoir (USGS Gauge ID 06713000) (SI Figure 3.8). Although streamflow increased at the confluence during the precipitation event, there was no concurrent increase at

the inlet from the Reservoir indicating that localized stormwater was driving the increase in discharge rather than releases from the reservoir.

3.7.2 Laboratory Analyses

Scanning Electron Microscopy. Dry powder was mounted to a glass slide using carbon tape and imaged using a ESCAN MIRA3 LMH Schottky field emission-scanning electron microscope (FE-SEM) at magnifications of 200-2x with a beam voltage of 5keV.

Single Particle Inductively Coupled Plasma Mass Spectroscopy (sp-ICP-MS). All spICP-MS analyses were performed on a Nexion 300D Quadrupole ICP-MS (Perkin Elmer, Waltham, MA USA). A mass-based method for determining transport efficiency of Pace, et al 2011 was used for all single particle analyses. A 50nm Au nanoparticle (Fortis Life Sciences, citrate-stabilized, mean size of 50 ± 4 nm by TEM) was used as a known mass standard in the method. Dissolved Au standards (0, 1, 10, 100 ug/L) [Inorganic Ventures, MSAU-100PPM, 100ug/mL Au in 10% v/v hydrochloric acid] were prepared through dilution with Milli-Q Water (18.2 M-ohm Barnstead International). Measured TE ranged from X to Y over the course of the experiments. Ta (0, 0.2, 2, 20 ug/L) [High Purity Standards, ICP-MS-68A-B, 10mg/L in 2% nitric acid + trace hydrofluoric acid] and Al (0, 1, 2, 20ug/L) (Aristar, BDH82026-120, 100mg/L in 3% nitric acid) were prepared through dilution using nitric acid (Fisher Scientific, Trace Metal Grade, 32-35%). All standards were prepared the day of analysis. Sample containers were sonicated for 10min, subsampled and the subsample was 10 mm-filtered (nylon, Tisch Scientific) prior to sp-ICP-MS analysis. Microplastic suspensions of PVP and PMMA were prepared by resuspending dry powder immediately before analysis. All sample dilutions for sp-ICP-MS analysis used MilliQ Water.

Samples were analyzed by sp-ICP-MS for ^{197}Au , ^{181}Ta or ^{27}Al at a flow rate of 0.3mL/min, with 100 msec dwell times, over a total data collection time of 60 sec. No settling time was used and a very short detector dead time of 35ns was utilized. Raw ICP-MS data was processed for single particle analysis using Syngistix 2.3 (Perkin Elmer, Waltham MA USA) with threshold values set to the mean plus three times the standard error ($\mu + 3\sigma$). A minimum of 1 count for the threshold value was used when the Syngistix-derived threshold was <1 count. MATLAB Build R2021b (MathWorks, Natick MA USA) was used for all post-processing and fitting of sp-ICP-MS data.

MP particle sizes were calculated as a function of the detected ^{181}Ta mass in each particle which was converted to a MP particle size ($d_{polymer}$) using the equations:

$$v_{polymer} = m_{metal} \times \frac{MW_{additive}}{MW_{metal}} \times \frac{1g \text{ Polymer}}{\% (w/w)_{Additive}} \times \rho_{polymer} \quad (3.4)$$

$$d_{polymer} = \sqrt[3]{\frac{6v_{polymer}}{\pi}} \quad (3.5)$$

Where:

$v_{polymer}$	Volume of Polymer (cm^3)	$MW_{additive}$	Mol. Wt. of Additive (g/mol)
m_{metal}	Mass of Metal (g)	MW_{metal}	Mol. Wt. of Metal (g/mol)
$\rho_{polymer}$	Density of Polymer (g/cm^3)	$\% (w/w)_{Additive}$	(w/w) % of Additive in Polymer

Both equations were used to convert detected ^{27}Al mass to an equivalently sized K-Feldspar Orthoclase particle (9.69% (w/w) Al, $\rho = 2.56\text{g}/\text{cm}^3$).

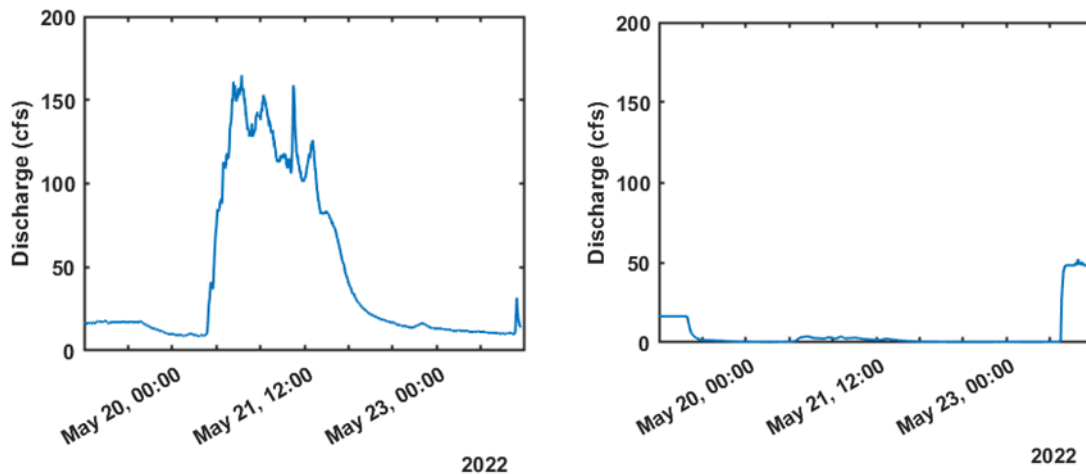


Figure 3-8 Hydrographs for Cherry Creek at the South Platte Confluence (Panel A, UGS GAUGE ID: 06713500) and at the mouth of Cherry Creek Reservoir along Cherry Creek (Panel B, UGS GAUGE ID: 06713000) over the course of the study time period, May 19th – May 23rd 2022. The confluence between Cherry Creek and the South Platte River is downstream of the study site whereas Cherry Creek Reservoir is upstream.

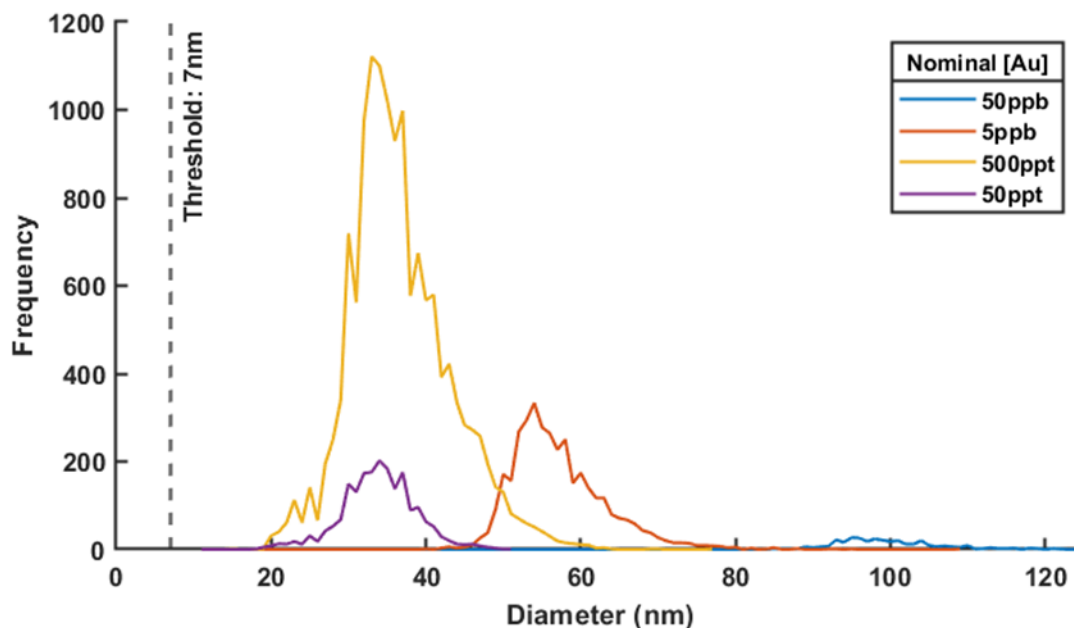


Figure 3-9 sp-ICP-MS analysis of dilutions of monodisperse 50nm ¹⁹⁷Au Nanoparticles (Nanocomposix, San Diego, CA) with nominal concentrations of ¹⁹⁷Au ranging from 50ppb to 50ppt. A consistent particle detection threshold was used for all dilutions that converts to a particle diameter of 7nm.

Fig 3-9 shows the typical effect of serial sample dilution on SD measured by sp-ICP-MS for a variety of concentrations of monodisperse ¹⁹⁷Au nanoparticles. At the highest two concentrations, coincidence and/or aggregation have caused a distortion of the SD such that particle numbers are suppressed, and the mean particle diameter is >50nm. Through serial dilution of the sample, the mean particle diameter reaches ~50nm at a [¹⁹⁷Au] of 500ppt and particle numbers scale with a further 10x dilution. Note that the threshold is well below the mean particle diameter and doesn't vary with dilution suggesting the absence of a background ¹⁹⁷Au signal.

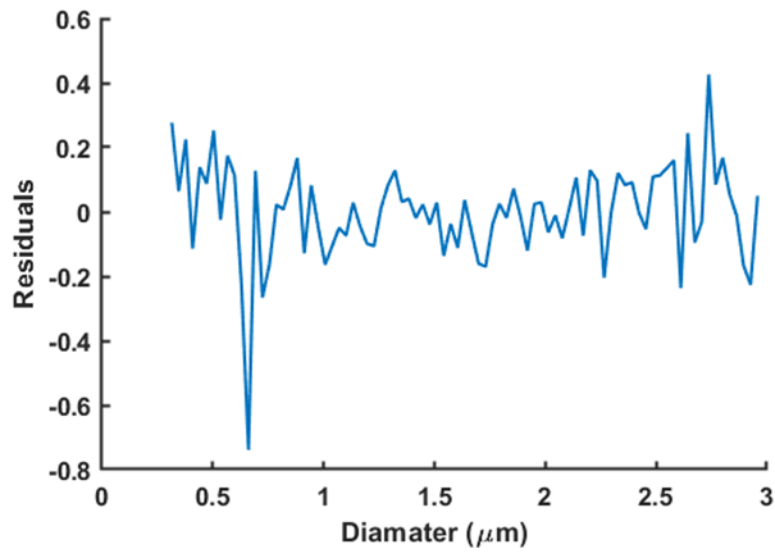


Figure 3-10 Residual plots for linear regression of Log N vs Log D for 0.1% (w/w) Ta-Ethoxide PVP.

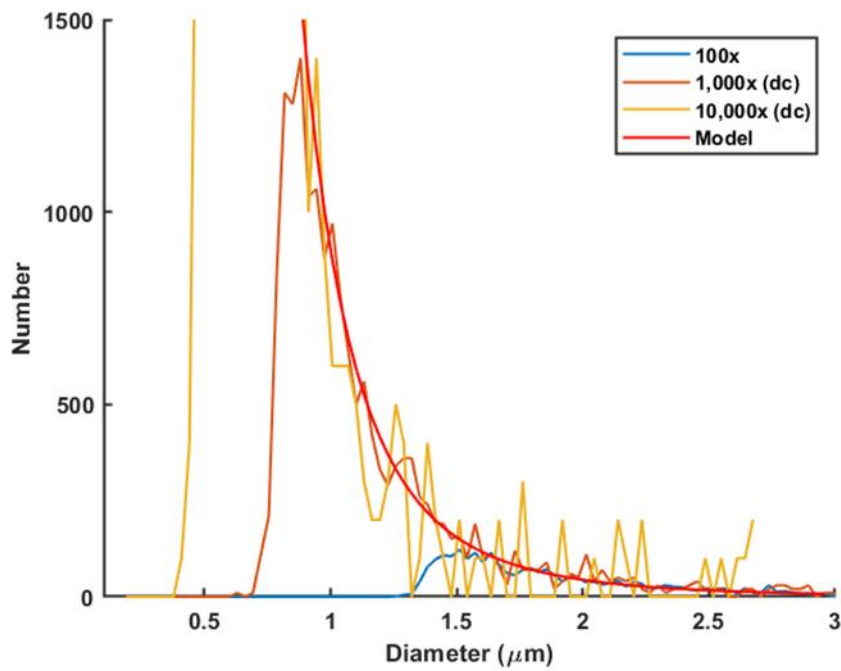


Figure 3-11 Comparison of the Power Law Model derived from the combined dataset to the dilution-corrected size distributions measured for the 0.1% Ta-Ethoxide (w/w) PVP suspension. The model line represents the results of linear regression of the Log-Log plot (Figure 3.3) and the power law model of particle number vs particle diameter generated from the linear regression. Particle numbers are normalized to the lowest dilution, denoted by (dc).

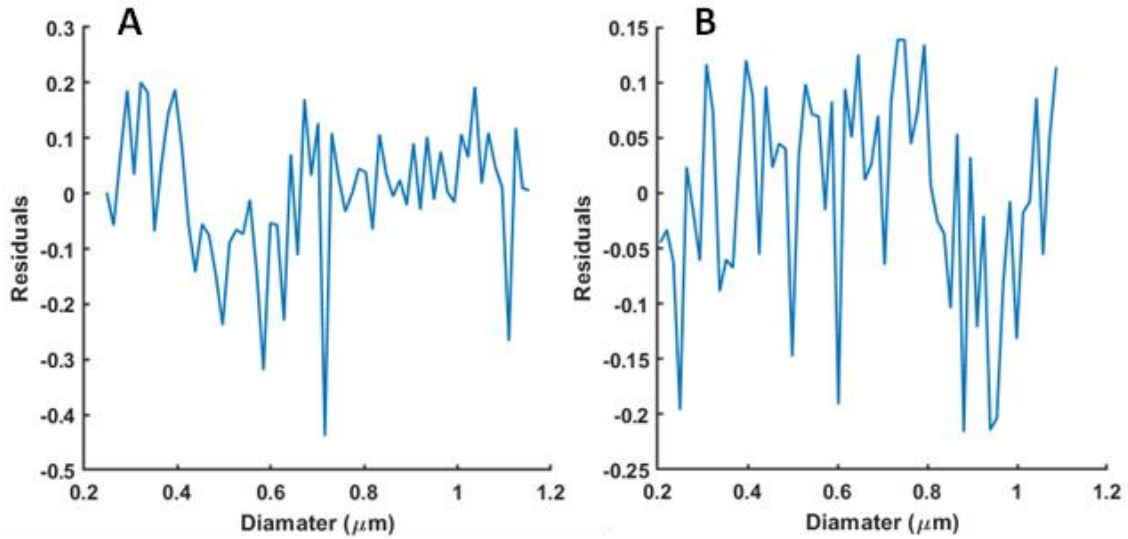


Figure 3-12 Residual plots for linear regression of Log N vs Log D for 1% (w/w) Ta-Ethoxide PVP (Panel A) and 0.1% (w/w) Ta-Ethoxide PMMA (Panel B).

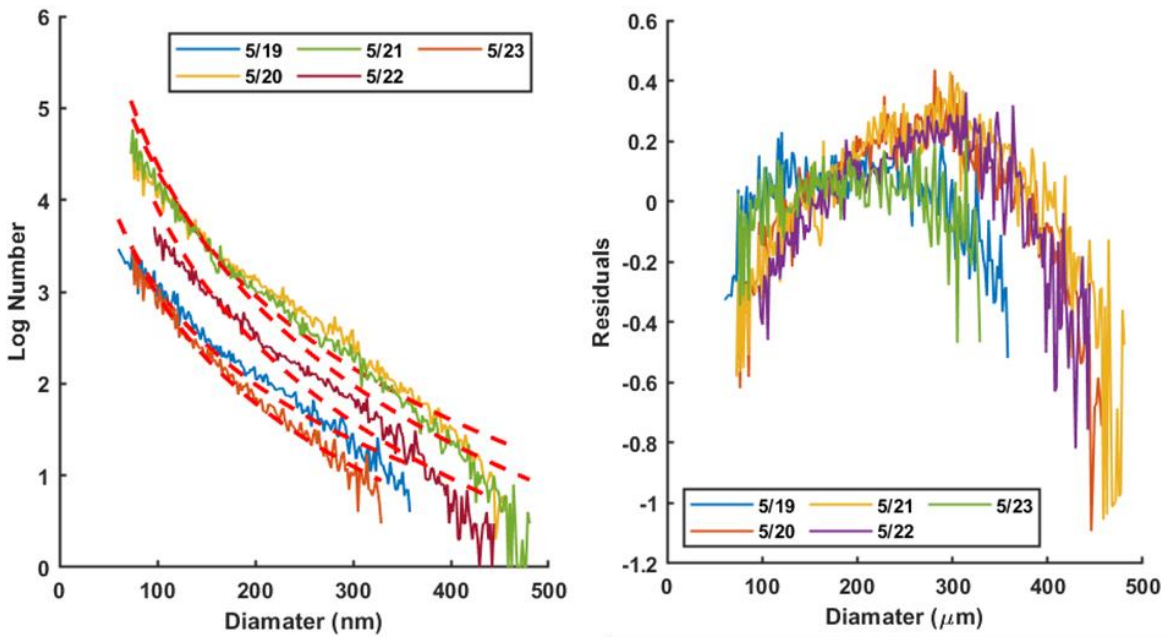


Figure 3-13 A. Plot of Log Number vs Diameter of the combined datasets used for power law modeling overlaid with the model line (dashed redline) for each sample. B. Residuals of power law models for each sample.

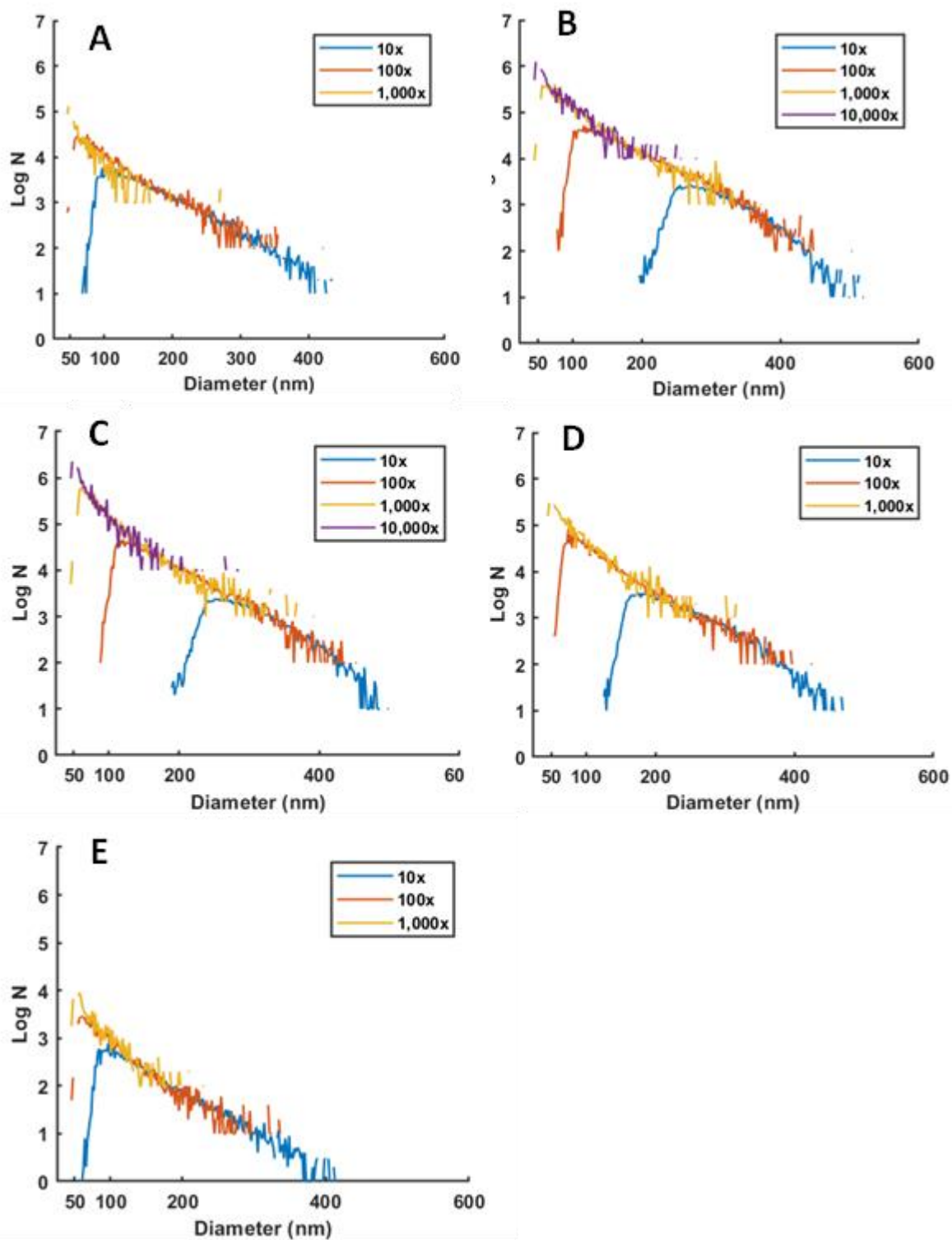


Figure 3-14 Log N- Log D comparisons of sp-ICP-MS PSD data measured at dilutions spanning 100x to 10,000x for Cherry Creek Samples. Panels correspond to individual samples: a. 5/19; b. 5/20; c. 5/21; d. 5/22; and e. 5/23. Particle numbers are corrected for the dilution.

Table 3-1 Results of Log-Log Linear Regression for the PVP and PMMA suspensions.

Polymer	Dilutions used for SD analysis	β	Log α	R ²
PVP	100x, 1,000x, 10,000x	-4.06 ± 0.09	3.45 ± 0.023	0.974
PMMA	10x	-1.55 ± 0.06	2.17 ± 0.02	0.916

Table 3-2 Results from sp-ICP-MS analysis of a 100x dilution of samples taken from Cherry Creek, CO USA. Calculated particle size assumes that the mass of Al detected is contained in K-Feldspar (2.7g/cm³). Discharge was measured at the Cherry Creek USGS Gauge (ID: 06713500).

Day	Mean Particle Diameter (nm)	Particle Conc (Part/mL)	Cherry Creek Discharge (cfs)	Threshold Size (nm)
5-19	102	360,088	17	16
5-20	164	954,849	90	29
5-21	164	786,431	117	35
5-22	113	825,232	15	20
5-23	91	298,314	11	16

Table 3-3 Results from sp-ICP-MS analysis of a 100x/1,000x dilution of samples taken from Cherry Creek, CO USA. Sample dilutions were chosen for each date such that the threshold value for particle detection is similar. Calculated particle size assumes that the mass of Al detected is contained in K-Feldspar (2.7g/cm³). Discharge was measured at the Cherry Creek USGS Gauge (ID: 06713500).

Day	Dilution Used	Mean Particle Diameter (nm)	Particle Conc (Part/mL)	Cherry Creek Discharge (cfs)	Threshold Size (nm)
5-19	100x	102	360,088	17	16
5-20	1,000x	97	4,389,040	90	16
5-21	1,000x	90	5,340,620	117	16
5-22	100x	113	825,232	15	20
5-23	100x	91	298,314	11	16

Table 3-4 Power Law Model β and log α values obtained through linear regression of sp-ICP-MS data plotted as Log N vs Log D.

Day	Dilution Used	β	Log α	Cherry Creek Discharge (cfs)	Threshold Size (nm)
5-19	100x	-3.07 ± 0.08	8.19 ± 0.18	17	16
5-20	1,000x	3.38 ± 0.08	9.89 ± 0.17	90	16
5-21	1,000x	-3.97 ± 0.09	11.12 ± 0.20	117	16
5-22	100x	-3.35 ± 0.07	9.26 ± 0.15	15	20
5-23	100x	-3.77 ± 0.11	9.47 ± 0.23	11	16

CHAPTER 4 SINGLE PARTICLE INDUCTIVELY COUPLED PLASMA AS A TOOL FOR THE STUDY OF NANOPLASTIC GENERATION AND PHOTODEGRADATION

4.1 Introduction

Plastic waste is a large and growing problem across the globe, with 4.8-12.5 x 10⁶ tons of plastic entering the earth's oceans on a yearly basis[167]. Although macroscale plastic debris is worrying on its own, a variety of environmental processes including mechanical wear, heat, UV degradation and biological processes transform these macroplastics into microplastics (<5mm in one dimension[168]) and eventually into nanoplastics (<1000nm)[25]. Nanoplastics themselves represent a unique class of contaminant that is distinct from their microplastic brethren for a variety of reasons. Firstly, their movement in aqueous systems is dominated by Brownian motion due to their size, and they are less subject to buoyancy and sedimentation. For example, according to Stokes' law, a 1mm Polyvinyl Chloride sphere will settle at a rate of 22cm/s whereas a 100nm sphere will settle at a rate of 7cm/yr[25]. Thus, independent of external forces or degradation, these nanoplastics have a much higher residence times in aquatic systems. Furthermore, for a given mass, nanoplastics will have more surface area than microplastics, making them more effective at adsorbing and transporting both inorganic[169] and organic[170] pollutants. Although plastics are referred to by their principal polymer component (polystyrene, polypropylene, etc.), commercial plastics contain a wide variety of additives for the purposes of tuning their physical and chemical properties. However, these compounds may become toxic when leached from their plastic matrices[27], [28] and the high surface area of nanoplastics aids this process[28]. Lastly, particle size is the principal factor in determining biological uptake. The smaller size of the nanoplastics makes their uptake much more likely than that of microplastics in aquatic environments[26]. For example, ultrafine aerosols, which include airborne nanoplastics, are more adept at penetrating biological tissue and can cause a wide variety of effects not seen from coarser particulates[35], [37], including inflammation.

Collection, characterization and quantification of microplastics is difficult but possible utilizing fractionation techniques such as filtration used in combination with light microscopy or IR-Raman Spectroscopy[171]. However, nanoplastics are a more difficult substrate to characterize as their smaller size naturally precludes using many of the analytical techniques used for microplastics. Separation techniques such as filtration may also struggle to separate these smaller plastics from background material and may cause sample loss. Lastly, the carbon composition and possibly low environmental concentrations of nanoplastics make them difficult to directly detect against a background of natural or other anthropogenic carbon-containing particles.

Single particle inductively coupled plasma mass spectrometry (spICP-MS) is a premier tool for the analysis of environmental colloids[57]. The technique marries the high element-specific sensitivity of

ICP-MS with a sample introduction system that introduces single particles into the plasma allowing for individual particles to be counted and sized. Particles entering the plasma produce a discreet burst of signal that can be differentiated from a background of dissolved element. The dividing line between dissolved and particle signals is a threshold value that is usually set as the mean of all measured signals plus a multiple of the standard deviation of the mean signal ($\mu+x\sigma$). Setting of the final threshold value involves an iterative process where particle signals are identified through thresholding, catalogued and removed from the signal population, and the threshold is recalculated. Commonly, a threshold of $\mu+3\sigma$ is used[130] in commercial software. Particle quantification by spICP-MS can be superior to more commonly employed bulk methods, as particles can be detected, sized and quantified at mass concentrations substantially less than other methods such as bulk ICP-MS analysis.

The application of spICP-MS to the quantification of micro and nanoplastics can be divided into two categories: Direct detection of plastic particles using their endogenous ^{13}C content or detection of the plastic particles through metal tagging of the particle. Direct detection of plastic particles was first pioneered by Bolea-Fernandez et al.[172] who demonstrated that plastic particles with diameters of $1\mu\text{m}$ and $2.5\mu\text{m}$ could be detected above background and sized using their naturally abundant ^{13}C content. Laborda et. al.[64] took this concept a step further using ^{13}C content to detect microplastics released from commercial products into nano-pure H_2O . Lastly, Liu et al.[83] followed the photodegradation of $5\mu\text{m}$ polystyrene spheres across 24hrs of exposure to UV-C light. Although impressive technical feats, this type of spICP-MS analysis is limited for a variety of reasons. The presence of carbonate as well as other organic compounds in most waters creates a high background of dissolved ^{13}C signal. Additionally, carbon is not efficiently ionized by the plasma torch with a first ionization efficiency of only 5% [173]. Both factors limit the spICP-MS ^{13}C analysis of microplastics to particles with diameters $>0.8-1\mu\text{m}$. This naturally limits the use of ^{13}C detection to mostly carbon free aqueous matrices limiting the applicability of this method for measuring particles in natural environmental matrices. Furthermore, this type of detection has no means to distinguish nanoplastic from other naturally occurring carbon particles or other carbon-based anthropogenic particles such as tire wear particles.

For these reasons, metal-tagging of micro and nanoplastics through the incorporation of metal moieties in the plastic themselves or by labeling the plastic particles with metal tags prior to spICP-MS analysis has been pursued. The advantage of this type of labeling is two-fold. The high elemental sensitivity of the ICP-MS allows for the detection of particles containing atto-grams of metal, Thus, doping only requires a very small weight percentage of metal, preserving the plastic particles physical and chemical attributes. Incorporation of a rare metal such as palladium or tantalum allows for the detection of the metal-doped plastic particles against both a carbon and mineral particle background.

Jimenez-Lamana et al.[174] presented a method for labeling negatively charged polystyrene microspheres with positively charged Au nanoparticles, allowing for their detection and counting by

spICP-MS. However, this technique only allowed for the counting of plastic particles not sizing, and the labeling method could be subject to interference if other negatively charged contaminant particles are present. Lai et al.[175] demonstrated another labeling method where Au nanoparticles were grown on the surface of microplastic particles using dissolved gold and NaBH₄, making them detectable by spICP-MS. For the labeling of plastic particles, they employed a mild digestion followed by cloud point extraction to remove any background particles. Both methods highlight two major limitations with post-synthesis labeling of microplastic particles: (a) This method of labeling only allows for particle counting not sizing as label incorporation may not scale with particle size, and (b) background particles can be labeled as well by the same processes, requiring a laborious, pre-labeling separation of microplastic particles.

In terms of incorporating metal tags into the plastic structure itself, one popular method is growing a plastic shell around a metallic core[82], [176]. Mitrano et al.[82] used these Pd-cored nanoplastic particles (100nm in diameter) to study their fate and transport in a wastewater treatment pilot plant. These were combined with In-labeled microfibers[177] to study co-transport of both metal-labeled nanoplastic and microfibers with natural organic matter in sewage sludge[178]. However, spICP-MS was not employed to measure the particle number concentration for these studies and instead bulk ICP-MS was used to follow nanoplastic degradation or transport. Although this type of tag allows for quantification of particle number, either directly or through bulk ICP-MS, transformation studies cannot utilize them as the metal tag is not uniformly distributed through the entire nanoplastic particle, as it is present only in the core. Thus, particle metal content is insensitive to changes in the thickness of the plastic shell.

We have recently created model, polydisperse metal-tagged nanoplastics by introducing a metal-containing additive homogeneously into a plastic wafer which is then milled into a micro/nanoplastic powder [Manuscript in Prep]. Metal-doped nanoplastics are an ideal substrate for studying the photodegradation of plastics in general as it allows for their discrimination versus a background when measured by spICP-MS. Furthermore, the presence of the metal additive throughout the structure of the plastic allows for the spICP-MS to not only detect the particles but size them as well. Although bulk degradation studies can utilize the metal-cored particles[82], measuring changes in size of the individual particles themselves by spICP-MS requires using homogeneously distributed metal tags. These metal-tagged nanoplastics used in conjunction with spICP-MS can provide both information on mass and number simultaneously.

To demonstrate the utility of this combination of metal-tagged substrate and spICP-MS analysis, the UV-photodegradation of polymethylmethacrylate (PM) and polystyrene (PS) nanoplastics doped with a tantalum organo-metallic additive was monitored using spICP-MS. For the purposes of this thesis, only PM results are presented but a future publication will incorporate both. Photodegradation through UV radiation is one of the most important environmental processes responsible for the mineralization of nanoplastics[179]. PM makes an ideal substrate for the study of nanoplastic photodegradation due to its

hydrophilicity, which increases its colloidal stability in aqueous media. Photodegradation of bulk PM has been shown to proceed primarily through absorption of UV irradiation by the ester moiety where the energy is used for scission of the main carbon chain[180]–[182]. Secondary scission of the ester side groups can also create radical species causing further main chain scission. Given the prior research on bulk PM, we suspected the nanoplastics would be vulnerable to UVB photodegradation as well, perhaps more so due to its high surface area. Changes in particle number and particle size were monitored using spICP-MS for the breakdown of PM suspensions over the course of 14d of irradiation.

The major difference between this study and what came before[83], [183]–[186] is the use of a truly polydisperse metal-tagged nanoplastic starting material. Previous studies focused on the use of monodisperse spheres which while analytically convenient, do not represent the size distributions of the material moving through the earth’s critical zone. By coupling spICP-MS and Single particle optical sizing (SPOS) together, we reveal that the particles are progressively reduced in size by irradiation in a “conveyor belt” manner (see Research Objectives for further discussion). SPOS was used as an alternate analysis technique for measurement of nanoplastic degradation in sizes that exceed what can be measured on the spICP-MS. Lastly, photoinduced fragility in the particles and in a macroplastic substrate were both analyzed by monitoring nanoplastic release using spICP-MS, establishing that this phenomenon can be observed over multiple size regimes. This study adds new information about the photodegradation of plastics in the environment that result in nanoplastic generation. More broadly the results demonstrate the utility of spICP-MS to study the transformation of metal-containing polydisperse nanoscale materials.

4.2 Research Objectives

Nanoplastics are a ubiquitous particulate pollutant that is difficult to study due to their majority carbon composition, which renders them indistinguishable from a carbon background, and their size, which limits the number of available techniques for their study. We propose that spICP-MS can be used in combination with model plastics doped with a small amount of metal to study the environmental processes that result in formation and degradation of nanoplastics (Figure 4.1). UV photodegradation will be the model environmental process used to establish the value of our synthesis/analysis approach.

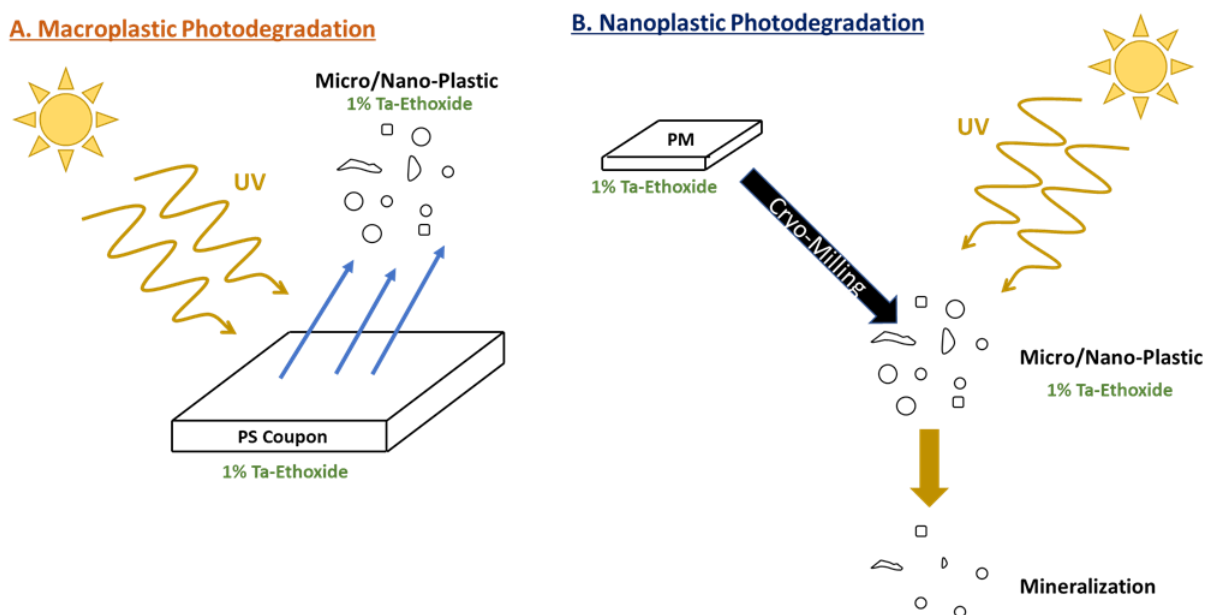


Figure 4-1 Schematic describing the (a) Quantification of nanoplastic released from a macroplastic as a function of UV photodegradation, and (b) Direct quantification of nanoplastic photodegradation

4.2.1 UV Photodegradation of Nanoplastics

We applied novel methodology using spICP-MS to follow the degradation of Ta-doped polymethylmethacrylate (PM) nanoplastics during photodegradation with artificially generated UV-B (λ : $300\pm 25\text{nm}$). The spICP-MS method for analysis of particles 0.2-2 μm in diameter was presented in Chapter 3.

We propose that UV-B irradiation of Ta-PM will cause a progressive reduction in particle size/mass that will be quantifiable by assessing the change in Ta mass by spICP-MS. This process will be analogous to a conveyor belt, where particles are smaller as they move along the belt (See Fig. 4.2 for a graphical representation). We therefore propose a series of hypotheses that describe specific aspects of this process.

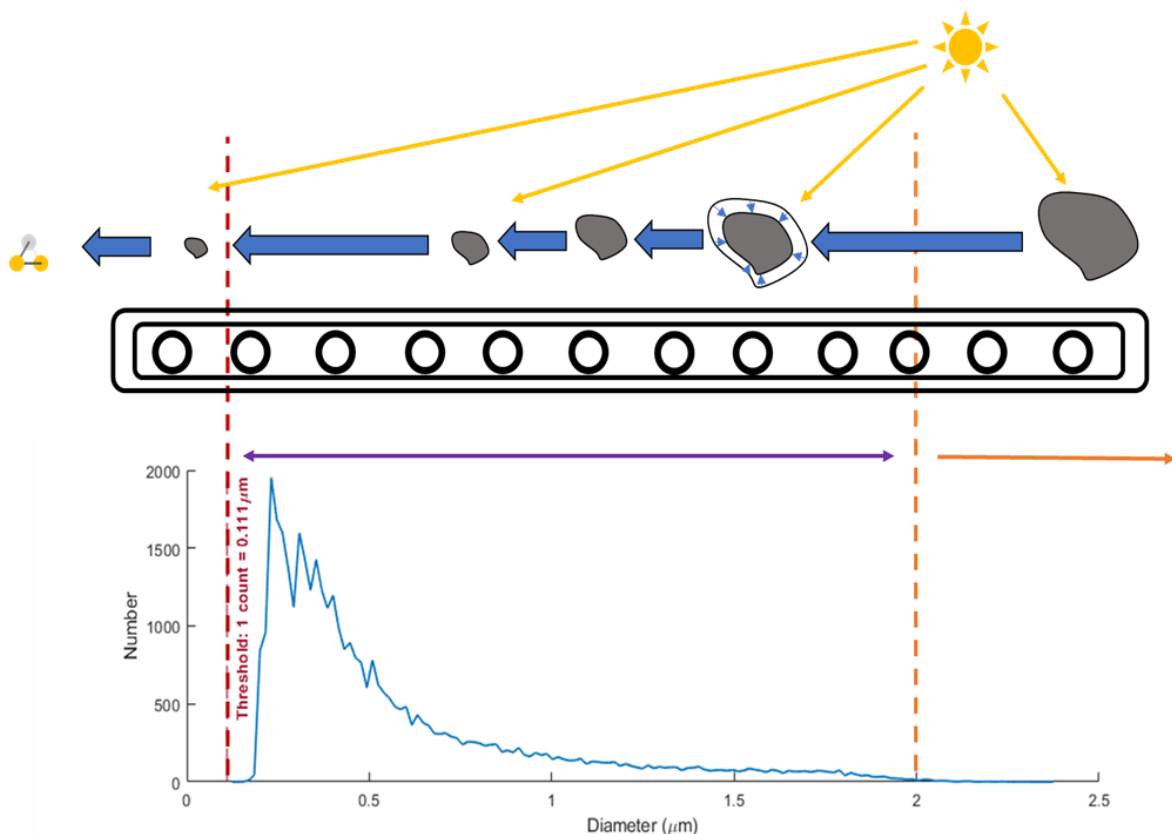


Figure 4-2 The “conveyor belt” hypothesis for the photodegradation of PM and the size regimes for which spICP-MS is applicable. spICP-MS Data broken into three different size ranges of analysis: (A) “Dissolved”; (B) Quantifiable Particles; and (C) Non-quantifiable Particles. The particle detection threshold (see chapter 3) has been converted to an equivalent mass of polymer assuming a 1% (w/w) loading of Ta-Ethoxide (details in Methods).

Hypothesis 1: Photolysis is a “Conveyor Belt” that creates changes in the particle number and size distribution within the spICP-MS Observable Size Range. The major goal of this research is to use spICP-MS and a metal-doped plastic to study the UV photodegradation of nanoplastics directly through changes in particle number and size. Our approach diverges from previous studies in that the particle size distribution (PSD) of the starting material is highly polydisperse, with particle numbers distributed over a continuum of sizes spanning orders of magnitude. This is a natural consequence of the cryo-milling process used to generate the nanoplastics from a macroplastic and reflects a more environmentally relevant PSD[79]. We hypothesized that UV photodegradation of the nanoplastics will proceed as a progressive reduction in particle size/mass as a function of UV irradiation (Figure 4.2).

When studying the nanoplastics directly, one must be cognizant of the characteristics of the starting material and how they interact with the observable range of the spICP-MS. Within the starting nanoplastic, particles sizes span from the nano to microscale and the relationship of particle number to size can be described as a power law which in plain terms means that there are exponentially more particles at smaller sizes than larger sizes. As demonstrated in the preceding chapter (Chapter 3), this

material can be fully characterized using a dilution series. With careful analysis that combines dilutions, one can obtain PSD data on the entire range.

Figure 4.2. depicts a typical spICP-MS analysis with three different regions highlighted. Region B, spanning from the threshold particle diameter, $0.11\mu\text{m}$ in this example, to approximately $2\mu\text{m}$, represents the size region in which particles can be both accurately counted and sized by spICP-MS. Region A exists between the instrument's detection limit (the smallest detectable mass) and the particle detection threshold is referred to as the "dissolved" region. In this region, the measured signal is some combination of signal from both dissolved species and possibly tiny particles whose mass is too small to distinguish from the background (see chapter 3 discussion). The most nebulous region of analysis, C, consists of particles larger than $\approx 2\mu\text{m}$ in diameter. Although particles can be detected and sized in this region, uncertainty in the transport efficiency and/or the ablation efficiency can make spICP-MS analysis unreliable. Both transport efficiency, the ability of the sample introduction system to transport a particle into the plasma, and the ablation efficiency, the ability of the plasma to convert the particle completely into ions, decrease with increasing particle size. Although it depends in the material properties of the particle (density, surface charge, etc.), both efficiencies generally reach low values for particles over $2\mu\text{m}$ [66].

Progressive mass loss in the polydisperse nanoplastic caused by UV irradiation was hypothesized to affect spICP-MS measurements in two ways. The weathering of small particles will cause their mass to drop below the particle detection threshold leading to their absence from particle sizing measurements. Graphically this would be represented on Figure 4.2 by movement of particles that start in Region B, the sweet spot for spICP-MS analysis, to Region A, the "dissolved" region where particles cannot be detected. Secondly, larger particles which initially started out too large to be detected or quantified by the spICP-MS (Figure 4.2, Region C) will lose sufficient mass to enter the detectable range of the spICP-MS (Figure 4.2, Region B). Given these two trends, detectable particle number concentration was predicted to decrease as the starting material contains a high proportion of smaller particles that would be rapidly photodegraded. However, conversely, the mean particle diameter is predicted to rise as the larger particles are brought into the detectable range of the spICP-MS.

SPOS, a technique effective for sizing larger particles (diameters $> 2\mu\text{m}$), was used to confirm the loss of particles larger than the quantifiable spICP-MS range over the course of the irradiation.

Hypothesis 2: NOM Influences PM Photodegradation. NOM was selected as an example of a species present in surface waters with known effects on the photodegradation of other compounds[187]. NOM was hypothesized to have two possible effects: (A) NOM could act as a shield for the nanoplastics, absorbing the incoming radiation thereby reducing the speed of the photodegradation, or (B) NOM could enhance the photodegradation of the nanoplastic through indirect photolysis, where radiation is absorbed by the chromophores present in the NOM and the energy is passed to the nanoplastic, thus degrading it more rapidly. If (A) occurs, the conveyor belt of UV photodegradation will be slowed and the loss in

particle number concentration/growth in mean particle size will be slower with NOM present than without. Conversely, if the reverse is observed than (B) is occurring and the presence of NOM in solution aids the photodegradation. To test these hypotheses, PM suspensions with and without natural organic matter (NOM) were subjected to UVB irradiation and changes in particle number and size were monitored.

Hypothesis 3. Particle Fragility as a function of UV Photodegradation. UV exposure of PM macroplastic is known to cause fracture, reductions in tensile strength and crazing[188]–[190]. It is reasonable to assume that these same processes happen on the micro/nanoscale and that the PM particles themselves will suffer from the same loss in structural integrity during the present photodegradation experiment. spICP-MS can be used to assess the fragility of PM particles in combination with pre-analysis sonication. Sonication can be considered an accelerated form of mechanical weathering[191] and particles made fragile by photodegradation should be more susceptible to shattering than undegraded PM particles. A higher number of particles should be observed by spICP-MS post-sonication compared to pre-sonication for the same samples if fragile particles are present. The amount of fragile material should be proportional to the UVB exposure time.

4.2.2 Nanoplastic Shedding and Fragility of UV Photodegraded Macroplastic

Nanoplastics are generated from macroplastic debris through a variety of different environmental processes but due to the size and composition, these released nanoplastics remain difficult to detect and quantify especially at low concentrations. Combining spICP-MS with metal-doped macroplastic substrates could help bridge this gap in nanoplastic analysis. Thus, we tested two additional hypotheses.

Hypothesis 4: Nanoplastics are Released from Bulk Plastic through Photodegradation. UVB irradiation of PM coupons imbued with a homogeneously distributed Ta additive will cause surface photodegradation proportional to irradiation time. These photodegraded surface will release nanoplastics when immersed in water and these passively released nanoplastics will be quantifiable by spICP-MS. Furthermore, nanoplastic release will increase as a function of UVB exposure time.

Hypothesis 5: Studying the Fragility of Macroscale Plastics through spICP-MS monitoring of Nanoplastic Release. Much as particle fragility after photodegradation can be explored with a combination of spICP-MS and sonication, so too can be the fragility of photodegraded surfaces. We hypothesize that the photo degradation process makes the bulk plastic more brittle. If this hypothesis is correct, exposing coupons to accelerated mechanical stress (i.e. sonication) will lead to additional nanoplastic release. Sonication applied to the photodegraded plastic surfaces should induce the release of greater numbers of particles than passive release alone (hypothesis 4), and this increase in particle number release will be proportional to UVB exposure time. Longer UVB exposure times will create more

sonication-vulnerable material due to expansion of the brittle, photodegraded layer at the surface of the plastic.

4.3 Materials and Methods

Nanoplastic/Macroplastic Synthesis. 1% (w/w) Ta-ethoxide polymethylmethacrylate (PM) coupons and nanoplastic powders were synthesized by collaborators at John Hopkins University (publication in prep) using the same procedure detailed in chapter 3. Whole coupons were used in the PM coupon photodegradation experiments.

Photodegradation Experiment. A Model RPR-100 Rayonet photochemical reactor equipped with 16 cylindrical, vertically oriented, low pressure mercury bulbs (Southern New England Ultraviolet Co, Branford, CT USA) was used for all irradiation experiments. The wavelength of light delivered by the bulbs was $300\pm 25\text{nm}$ (UVB). The fluence of the reactor was 5.21×10^{16} quanta/sec as determined by actinometry[192]. The reactor was equipped with a cooling fan that kept temperatures in the reactor $< 30^\circ\text{C}$ during operation, and a sample carousel rotated sample tubes ensuring even irradiation. All irradiation experiments were carried out in quartz test tubes whose tops were wrapped in parafilm and then aluminum foil to avoid liquid sample evaporation.

Nanoplastic Suspension Experiment. Approximately 50mg of dry nanoplastics powder was resuspended at a nominal concentration of 1mg plastic/mL and sonicated in an ice bath for 4 hours. The resulting suspension was then sieved with a stainless steel $32\mu\text{m}$ sieve to remove any unsuspended material. The suspension was then diluted 50x with nano-pure H_2O (npH₂O) and 8mL of the 50x suspension was aliquoted into each of 4 quartz test tubes. For PM suspensions involving the addition of natural organic matter, the original PM suspension was diluted 50x into a npH₂O solution containing 10mg C/L Suwanee River Fulvic Acid (SRFA) (International Humic Substances Society, Product ID: Suwanee River FA II). Prior to the beginning of the experiments, the tubes were subsampled to establish an initial (day 0) sample, by taking 600uL from each tube and adding it to 5.4mL of npH₂O (10x dilution). All subsequent sampling of the photolysis tubes was done in the same manner. Three tubes, labeled A, B and C, were placed at random positions in the photoreactor sample carousel where they were continuously irradiated with 300nm radiation for up to 13 days. One tube was foil wrapped and placed in the dark outside the reactor to act as a dark control (labeled D). All four tubes were sampled after 1, 3, 5, 7, 9, 11 and 13 days of total irradiation time.

Coupon Photolysis Experiment. Irradiation of PM coupons with UVB light was completed by Casey Smith at John Hopkins University. Ten weighed, 1% Ta-Ethoxide (w/w) PM coupons were placed dry into quartz test tubes, which were placed inside a similar reactor setup as was used for the PM suspension experiments performed at CSM. Coupons were then irradiated for 0, 3, 7, 10 or 14 days with two coupons removed from the reactor per irradiation time. Coupons were weighed, placed in clean 15mL conical

tubes to which 10mL of npH₂O was added. The coupons were then allowed to passively release for a period of 7d, upon which the solution was removed, and the coupons were dried and stored. Solutions from the release and the coupons themselves were then mailed to Colorado School of Mines where the solutions were analyzed by spICP-MS to characterize particle release from the irradiation itself.

Nanoplastic Release Following Coupon Sonication. At Colorado School of Mines, the dried, irradiated coupons were placed in fresh 15mL conical tubes containing 10mL of npH₂O and allowed to sit for 1d. This step was designed as a rinse to remove residual materials from the coupon itself, and these solutions were removed from the coupons and analyzed by spICP-MS as a background to the sonication experiment. A fresh 10mL of solution was added to each coupon and the coupons in solution were bath sonicated for a period of 30min. After sonication, coupons were allowed to rest for 1d allowing for the release of any PM particles resulting from the sonication. Solution was removed from each coupon and analyzed by spICP-MS.

Measurement Parameters of the spICP-MS. Samples were gently vortexed and assayed for ¹⁸¹Ta containing particles using a quadrupole spICP-MS instrument (PerkinElmer Nexion 300D, Waltham, MA, USA) equipped with a cyclonic spray chamber. Each spICP-MS run was 60sec in length, where particle-generated signals were integrated in 100 μ dwell times. Flowrate for the analysis was 0.3mL/min. Transport efficiency was calculated using the size-based method of Pace et al.[120] where the instrument signal is calibrated through the combination of a dissolved ¹⁹⁷Au calibration curve and monodisperse 50nm Au nanospheres (NanoXact Citrate-Stabilized, NanoComposix, San Diego, CA, USA). Each nanosphere delivers a known mass of ¹⁹⁷Au to the instrument and through comparison to the dissolved calibration curve, the transport efficiency can be calculated. Transport efficiency typically ranged from 5-8%. Data collection and analysis, including particle detection, was accomplished using Syngistix ver2.3 (PerkinElmer, Waltham, MA). For spICP-MS analyses involving sample sonication, samples were sonicated for 5, 15 or 30 total minutes using a sonication bath prior to analysis. Multiple dilutions for each sample were measured, where the initial measurement detected >5000 particles or the threshold was 1< count.

Data Processing for spICP-MS Data. Through the Syngistix software, the particle detection threshold was calculated as the mean plus three times the standard deviation of all signals ($\mu + 3\sigma$). Threshold determination in Syngistix is an iterative process where particle signals are identified, removed, and the threshold is recalculated until no more particles are detected. Where the calculated threshold was <1 count, it was manually set to 1 count. Given the whole number counting of the detector, 1 count is theoretically the smallest discrete amount of mass that can be measured on the instrument.

Detected Ta mass was converted to an equivalent size of nanoplastic particle using the equations 3-4 and 3-5 from Chapter 3 of this thesis. For this experiment, MW_{metal} was 180.948 g/mol (Tantalum), MW_{Add} was 406.25 g/mol (Ta(V) Ethoxide), the w/w % of additive was 1% and ρ_{PM} was 1.18 g/cm³.

As per the methodology discussed in chapter 3, spICP-MS data from multiple dilutions for each sample was compared to assess the possibility of data distortion due to particle coincidence. Where appropriate, data from multiple dilutions were combined into a single data set spanning the entire range of sizes measured across all dilutions for a single sample. All presented particle number concentrations and measured particle masses are corrected to reflect the TE and the dilution factor. Particle mass concentrations by particle diameter were calculated by summing all particle masses present in each size bin and correcting for transport efficiency and dilution factor.

SPOS Measurement Parameters. SPOS (Single Particle Optical Sizer, Nicomp Accusizer 770, Particle Sizing Systems, Santa Barbara, CA, USA) was conducted to quantify particles with 0.5-32 μ m in diameter. Although particles were detected larger than 32 μ m in diameter, these detections were few in number (< 0.01 % of the total number counted) and deemed erroneous due to the 32 μ m sieving of the suspensions prior to the experiment. To minimize particle coincidence, samples were diluted in npH₂O aiming to measure <10,000 parts/mL. Dilutions of 20- to 100-fold were commonly used for SPOS analysis. All presented SPOS PSD are corrected for the dilution factor.

Zeta Potential. A Malvern Zetasizer (Malvern, Malvern, UK) was used to measure surface charge for PM suspensions with and without 10mg/mL SRFA NOM. Samples measured by Zetasizer were undiluted. Two replicate measurements were taken of each sample.

4.4 Results and Discussion

4.4.1 Establishment of the Conveyor Belt and Influence of NOM.

Particle number (PNC) and particle mass concentration (PMC) for the PM and PM-NOM dark controls (Figure 4.3 a, b, e, f) remained relatively constant over the irradiation course, apart from some loss on D11-13. This indicates that the changes in the light samples (A, B and C) were driven by the 300nm irradiation and not by other factors (storage loss, dissolution, etc.), which would have affected the dark controls as well. The average D13 particle number concentration (PNC) of the three irradiated samples for both PM and PM-NOM were similar, $4.42 \pm 2.33 \times 10^6$ and $2.63 \pm 1.46 \times 10^6$ part/mL, respectively. Furthermore, the particle mass concentration (PMC), i.e. the sum of mass in detected particles per mL, was substantially higher for the PM suspension ($2.02 \pm 1.07 \times 10^{-6}$ g/mL) compared to the NOM PM suspension ($2.69 \pm 1.59 \times 10^{-8}$ g/mL). The average mean particle diameter was larger for PM (687 \pm 22nm) compared to the PM-NOM (582 \pm 40nm). Growth in mean particle size for irradiated PM samples B/C (Figure 4.3c) coupled with steady PNC (Figure 4.3a) lead to an increase in PMC in both samples (Figure 4.3e). For PM sample A, PNC declined but mean particle diameter increased leading to PMC remaining steady over the course of the experiment. Particle diameters reflect an equivalent PM

particle size to the ^{181}Ta particle mass measured by spICP-MS. All samples were sonicated 5min prior to spICP-MS analysis.

Sample to Sample Variance. Sample to sample variance was significant for some samples in this analysis and bears further discussion. The difference in behavior between PM A and PM B/C suggests that particles may be more difficult to reproducibly measure than dissolved species. When comparing these results to other studies of nanoplastic degradation, one must be cognizant that the majority of these studies use commercially synthesized, monodisperse plastic microspheres that lack the heterogeneity of our PM suspensions. Furthermore, bulk measurements require the use of PNC orders of magnitude greater than those used in this study. With our irregularly shaped, polydisperse starting material, a variety of factors including irregular particle shape, small differences in particle size distribution and nanoscale differences in particle structure, etc. become more significant sources of error at low PNC. Low abundance, larger plastic particles are more likely to be heterogeneously distributed across sample replicates at low total PNC. These larger particles can make up a majority of particle mass and are hypothesized to act as a source of smaller particles after photodegradation. Thus, sample to sample variability in the population of large particles may lead to irreproducible PNC and PMC results for all particle sizes. Possible storage effects over the course of a days-long experiment causing particle loss are more significant at low PNC and at high PNC (i.e. bulk); many of these effects can be averaged out and storage length minimized. Future studies might incorporate more replicates to account for these effects or further restrict the size range of particles in the starting PM suspension through filtration or centrifugation.

Photodegradation Mechanism and Process. Mean particle diameter remains relatively constant for a period of 5-7 days in both PM and PM-NOM irradiated samples suggesting that there is some minimum amount of photodegradation needed prior to significant weathering. This aligns with previous studies of polystyrene MP degradation which suggest there is a lag time before particle degradation occurs [83], [184]. Meides et al. suggests a model for plastic particle degradation that consists of a lag phase where particles suffer radiation damage causing surface abrasion and decollation, i.e. the loss of small loosely held materials on the particle surface. This correlates well with the 5-7d range of the irradiated PM samples where mean particle diameter hasn't risen significantly but PMC has increased slightly, and PNC has increased by roughly 2x. The source of these extra particles could be from the decollation of smaller particles from larger particles, including from those that were initially larger than observable by spICP-MS. Finally, the model suggests that after a certain amount of time, particles have suffered enough damage to fracture and be lost (i.e. reduced to a size below the threshold or fully mineralized). Particle fragility will be addressed in a forthcoming section, but the growth in particle mean diameter suggests that overall, small particles are being lost over time.

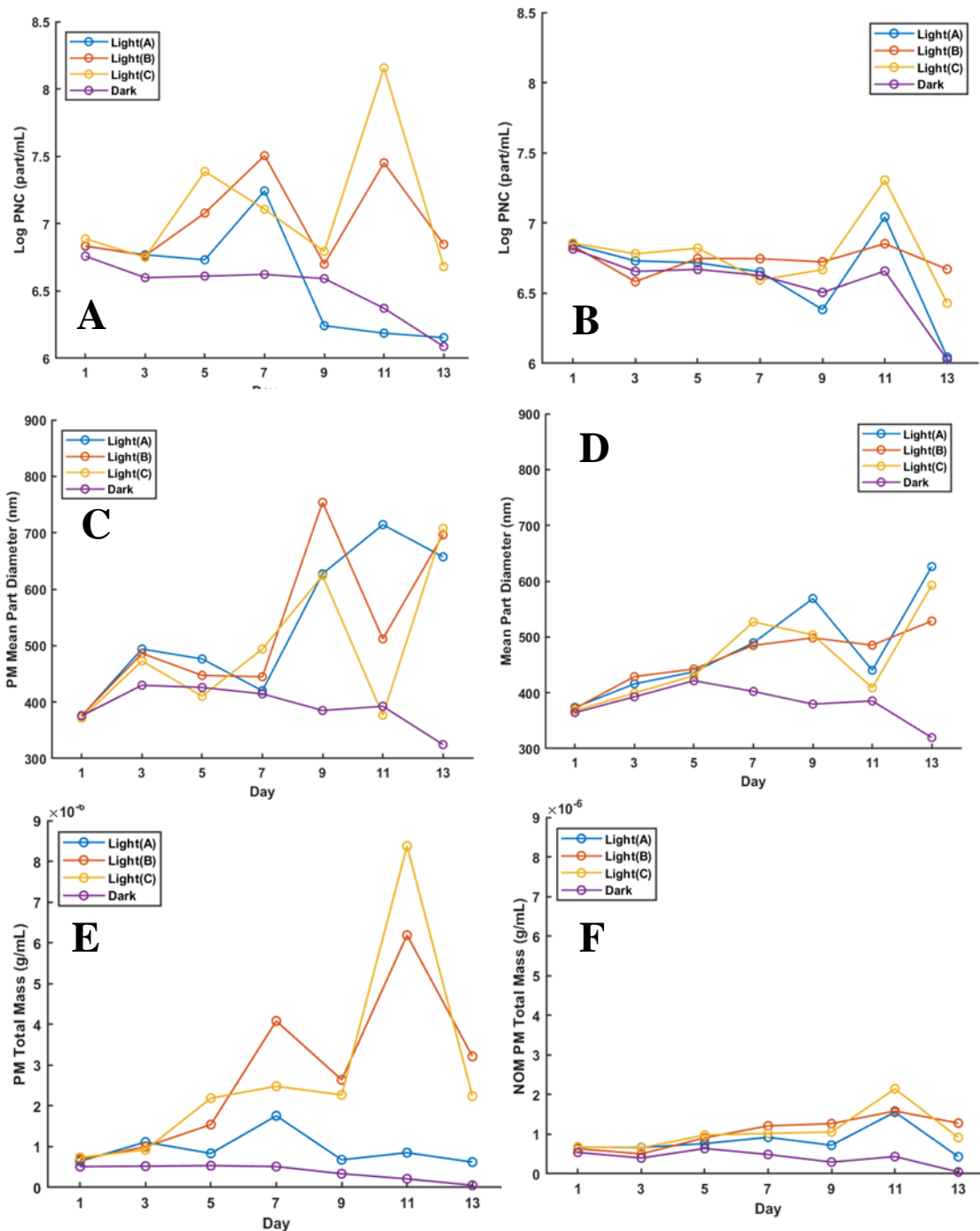


Figure 4-3 Sample parameters measured by spICP-MS for PM suspensions without NOM (PM) and with 10 mg /L SRFA (PM-NOM) over 13d of 300nm light irradiation: Particle Number Concentration (A, PM; B NOM-PM), Mean Particle Diameter (C PM; D NOM-PM), and Particle Mass Concentration (PMC) (E PM; F PM-NOM).

The previous studies of PS microspheres differ from the current PM results in a variety of ways. Liu et al., who used ^{13}C spICP-MS to study the degradation of monodisperse 5 μm diameter polystyrene spheres, found decreasing mean particle diameter over the irradiation course. This was coupled to a 2x increase in PNC which was followed by declining PNC through the last timepoint. PMC was not calculated in their experiment but it can be inferred from the trend in mean particle diameter and PNC that it decreased over the course of the experiment. This contrasts with both the PM and PM-NOM results which show a steady-increasing PNC coupled with increases in mean particle diameter and PMC. This is where the difference in starting materials come into play, as Liu et al started with a monodisperse population within the observable size range of the spICP-MS, whereas the starting PM suspension in this experiment contains a wide range of sizes, some larger than spICP-MS can detect. These larger particles in the PM suspension are suggested to act as a reservoir of particles which are progressively weathered into spICP-MS detection range, thereby replenishing the particles that are weathered to the point of being too small to detect. This leads to a relatively stable PNC but increasing PMC and mean particle diameters as the replenished particles are larger than those lost

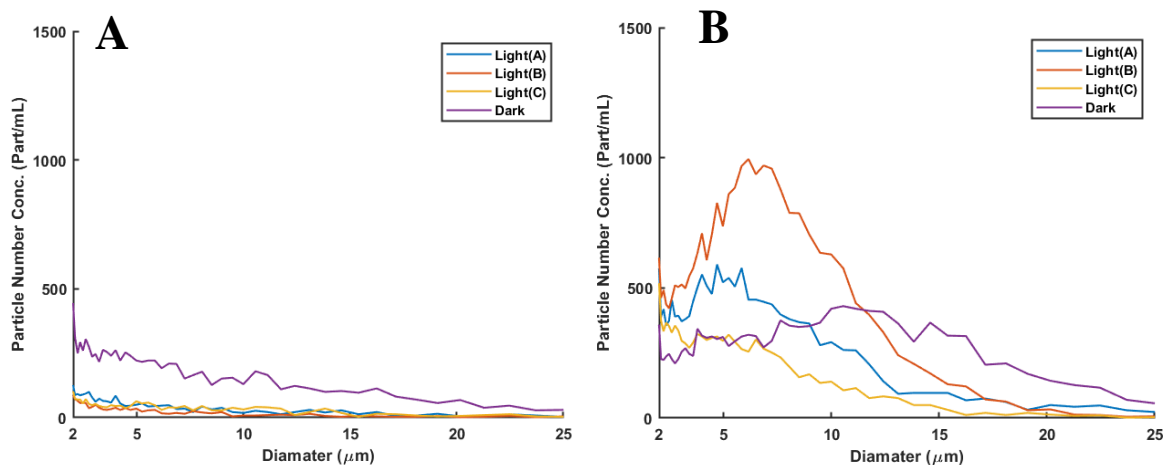


Figure 4-4 SPOS analysis of (a) D13 PM and (b) PM-NOM Suspensions. Particle numbers corrected for any dilution made prior to SPOS analysis. Although particles $<2\mu\text{m}$ were measured by SPOS, analysis was focused on larger sizes which are practically invisible to the spICP-MS.

Single particle optical sizing, a technique that can reliably count and size particles larger than possible by the spICP-MS, was used to show changes accompanying irradiation in population of particles larger than $2\mu\text{m}$ in diameter. This size of particle may not be effectively measured by spICP-MS. SPOS analysis of the D13 PM samples shows a depletion of larger particles in the three irradiated samples (A, B and C) compared to the dark control (Figure 4.4a). This suggests that the source of larger particles and particle mass seen by spICP-MS are the larger spICP-MS invisible particles, which are being UV weathered into spICP-MS visibility. This supports our conveyor belt hypotheses and that there is progressive UV

photodegradation of particles occurring in the irradiated samples, bringing them into and out of the observable range of the spICP-MS.

Influence of NOM. On average, D13 PNC was similar between the irradiated PM and PM-NOM samples, but mean particle diameter and PMC were substantially larger for the PM samples compared to PM-NOM (Figure 4.3). These results suggest that NOM was inhibiting photodegradation in the irradiated PM-NOM samples preserving the smaller particles and preventing the weathering of larger particles into the spICP-MS observable range. The protective effect of NOM is confirmed by the SPOS results as the irradiated samples (A, B and C) of the PM-NOM suspension (Figure 4.4b) still retain large numbers of 2 μm^+ particles compared to the dark control supporting the conclusion that the NOM is protective from UV degradation. Measured particle numbers in the dark control are higher in the PM-NOM sample than the PM sample most likely due to the increased colloidal stability of the PM-NOM particles as indicated by the zeta potential measurements. Zeta potential measurements of the PM suspensions showed a more negative value in the presence of NOM (-29.5mV) compared to without NOM (-17.2mV).

The most likely cause of this protective effect is that the NOM is absorbing the incoming radiation, shielding the PM particles from the harmful radiation. UV absorbance spectra (200-500nm, Figure S.2) of the NOM controls shows a clear photobleaching of the NOM over the course of 13d of irradiation. These pieces of data together suggest that the NOM adsorbs to the PM particles creating a UV protective layer that is photobleached over the course of 300nm irradiation. Unlike many other plastics such as polypropylene and polyethylene which lack a chromophore in their chemical structure, PM can directly absorb UV radiation <320nm in wavelength through its ester moiety[181]. Thus, the absorbance of light by the NOM layer interferes with the direct photolysis of the PM thereby slowing the conveyor belt of PM degradation.

As to the possibility of indirect photodegradation, enhancement of polypropylene photodegradation in the presence of polystyrene-derived organic matter[193] and NOM[194] suggests possible mechanisms of indirect photolysis for microplastics. However, the mechanism postulated for the enhancement effect was increased reactive oxygen species (ROS) generation by the organic matter. These ROS were necessary for degrading the polypropylene as it contains no chromophore of its own unlike the PM used in this experiment[22]. In these results, the direct absorption of UV is the process driving PM photodegradation, so the shielding effect of NOM is more significant than any possible indirect photodegradation catalyzed by the NOM. The effect of NOM character, specifically its ability to absorb UV radiation, is one possible interesting area of future research as NOM character can vary greatly and different NOM may have different protective capacities for PM.

“Conveyor Belt” Conclusions. spICP-MS analysis of the UVB photodegradation of a metal-tagged nanoplastic demonstrates that this process largely conforms to the proposed “conveyor belt” hypothesis. NOM was found to directly affect the photodegradation of PM by acting as a UV-absorbing shield that

delayed PM photodegradation. The major accomplishment of this initial experiment was to demonstrate that a combination of metal tagged nanoplastic substrate, spICP-MS, and SPOS can be used to quantitate and characterize the degradation of a nano-sized material in the presence of environmental matrices like NOM. Bulk studies of microplastic degradation are generally qualitative, using techniques such as FTIR and/or Raman spectroscopy or electron microscopy to follow bulk chemical and morphological changes [186], [195], [196]. Bulk measurements such as mass concentration [82], [177], [178] can be used to follow nanoplastic removal and mineralization, but reveals little about the mechanism of the process itself. PNC and PMC provided by spICP-MS show transformations on a nanoscale and in this study, back up many of the observations made for the photodegradation of larger plastic types. We hope that this analysis framework can be extended to other environmental processes, increasing our understanding about the ways in which nanoplastics are transformed in the environment.

4.4.2 Particle Fragility

One aspect of the measured spICP-MS data that doesn't conform to the hypothesis are the particle number concentrations (Figure 4.3a/b) measured over the course of the experiment. The original PM suspension used for the irradiation experiment contained a power law relationship of particle number to particle size (SI Figure 4.13), showing a higher proportion of small particles to large particles. As demonstrated in Figure 4.2, spICP-MS detected particles until they weathered below the limit of detection; likewise, larger particles initially invisible to the spICP-MS should weather into the detectable size range, but their numbers should not be completely replenished due to the low starting proportion of large particles. However, the observed PNC remains constant for the irradiated samples, suggesting a mechanism for particle number replenishment outside of the progressive UV weathering.

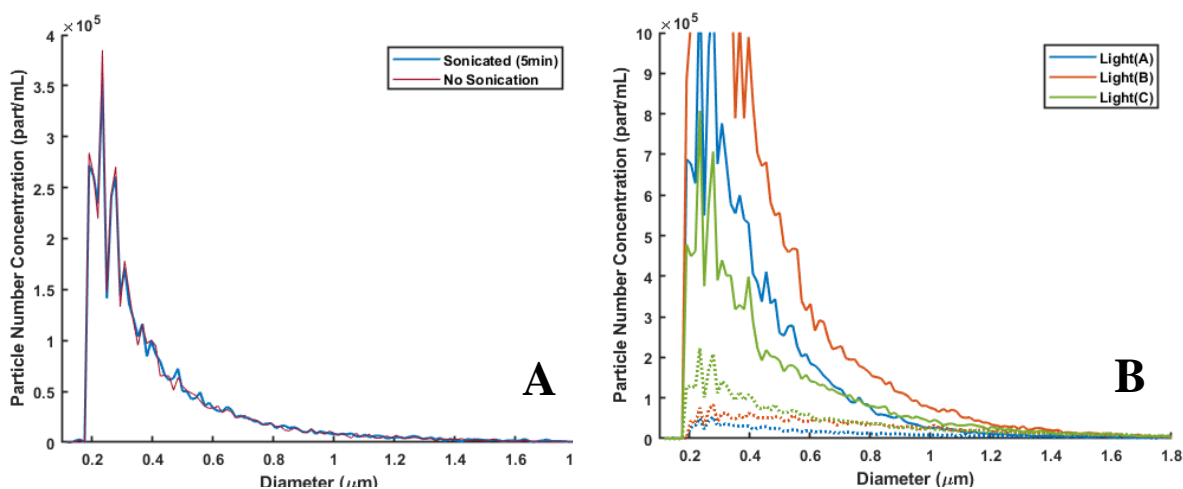


Figure 4-5 (A) PSD for PM dark control day 7 where blue and red lines represent spICP-MS analysis with and without sonication prior to analysis, respectively. (B) PSD for the day 7, irradiated PM samples A, B and C 7 where dashed and solid lines represent spICP-MS analysis with 0 or 5min sonication prior to analysis, respectively. Particle Diameters reflect an equivalent PM particle size to the ¹⁸¹Ta particle mass measured by spICP-MS.

Serendipitously, an error in sample preparation led to an interesting observation about the nature of the PM particles after photodegradation. It was general practice prior to D7 of this experiment to sonicate all PM samples for 5min prior to analysis to resuspend any material adsorbed during storage. However, initially the day 7 samples were measured by spICP-MS without sonication. Upon discovery of the error, samples were sonicated for 5min and analyzed again. Although the particle number concentration (PNC) measured for the dark control (Figure 4.5a) remained similar with no sonication (NS) and after sonication (SN), there was a substantial growth in PNC post-sonication for the three irradiated samples (Figure 4.5b). The appearance of additional particles after sonication suggests that the sonication may have broken apart material creating extra particles. That this happened only in the irradiated samples suggests that photodegradation may create “fragile” particles that can be shattered by the application of mechanical force. Given this observation was made late into this irradiation experiment, only timepoints after D7 could be assayed for the presence of these “fragile” particles (Figure 4.6) and some timepoints do not have complete data sets (i.e. sonicated/non-sonicated data for all four samples).

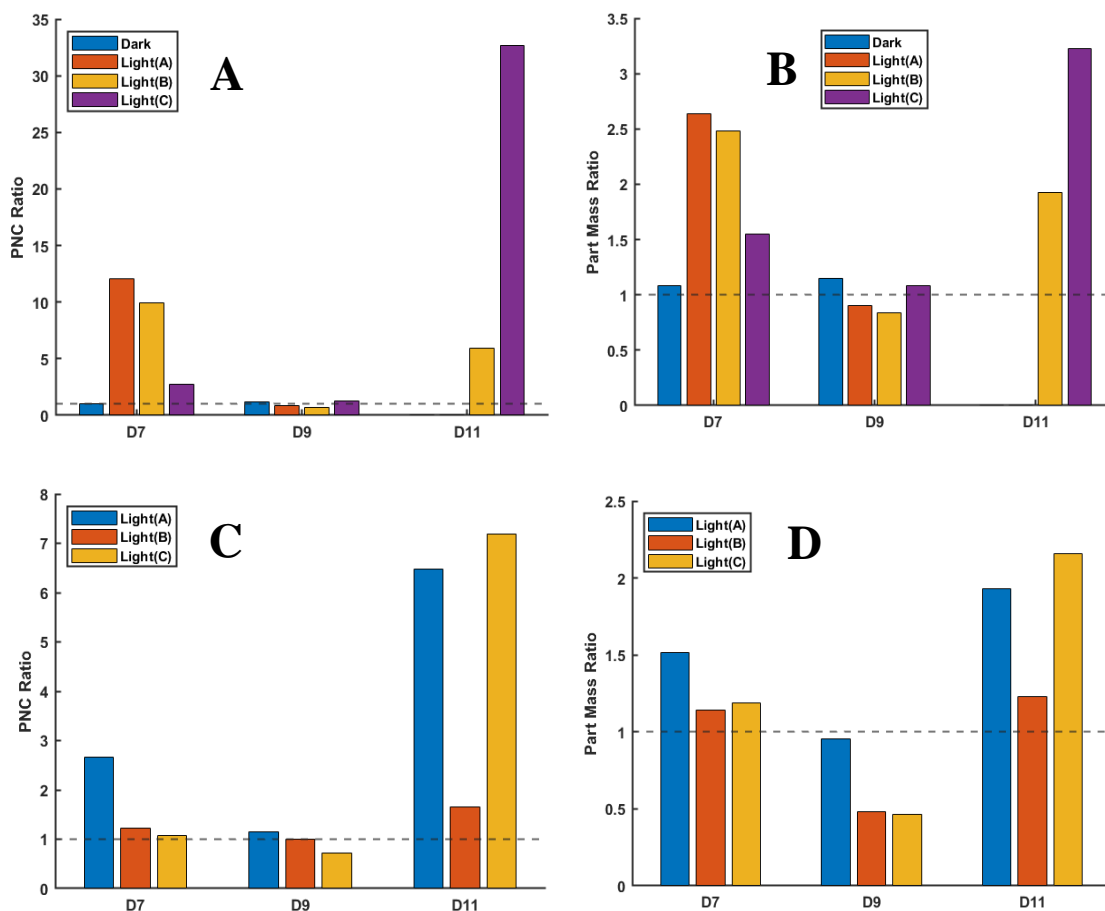


Figure 4-6 Ratio of spICP-MS measured PNC and PMC for Sonicated (5min, SN) and Non-Sonicated (NS) samples for PM (Panels a and b, respectively) and PM-NOM suspensions (Panels c and d, respectively). There were no measurements of SN to NS material for the Dark and Light (A) samples on D11 for the PM suspension (Panels a/b)

A comparison of PNC and particle mass concentration (PMC) measured for sonicated (SN) and non-sonicated (NS) samples for D7, D9 and D11 samples of both the PM and PM-NOM suspensions is shown in Figure 4.6. In general, where additional particles were observed by spICP-MS (PNC Ratio >1), additional mass in solution (PMC ratio >1) was observed as well. The increase in observed mass suggests that the additional particles may have been brought into the spICP-MS observable size range through the shattering of fragile large particles outside this size range. Nanovoids formed by UV-induced chain scission[195] become propagation sites for larger cracks that are widened by further UV irradiation or other forces (mechanical, thermal, etc.)[189]. This process has been investigated on the macroscale in PM airplane cockpit canopies[189] and in PM-ZnO composites[195]. Our results broadly suggest that this process is happening on the nanoscale as well.

Mild mechanical force (stirring) was shown to fracture severely degraded microplastic particles after 3200hr of solar simulator exposure[184] or 12hr of 254nm irradiation[83]. Similar to our results, Liu et al

reported increases in PNC concurrent with the detection of smaller particles, which suggesting that the larger particles are fragmenting into larger numbers of smaller particles. In our experiments, sonication is shown here to be effective in fragmenting photo-weakened material, but not strong enough to disrupt pristine material.

The degree to which sonication caused increases in PNC and PMC varied from day to day and sample to sample. For both PM and PM-NOM, D9 samples showed little evidence of fragile material compared to the day preceding (D7) and following (D11). However, one possibility is that the particles undergo cycles of being weakened by photodegradation and shattering, repeated ad nauseum until complete mineralization. Brandon et al.[186] saw a similar cycling in their microplastic UV degradation study as the ratio of oxygen-containing functional groups, a measure of photo-oxidized material, was cyclical over the course of irradiation. They speculated that as photo-oxidation can only occur to a surface depth commensurate with O₂ infiltration, that there were cycles of surface material being weakened until fragmentation. This fragmentation exposes virgin plastic to UV photooxidation, thereby beginning the cycle over again. In our experiment, we postulate that particle fragmentation follows a similar cycle of larger particles being weakened before ultimately fragmenting into smaller particles with virgin surfaces. Thus, the cycling of PNC increases post-sonication reflects this cycle of photodegradation followed by particle fragmentation.

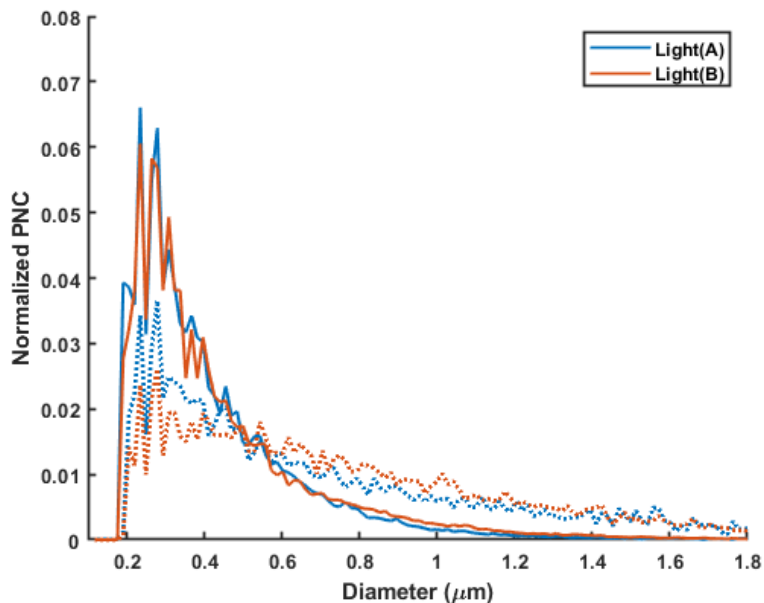


Figure 4-7 Normalized PNC for PM D7 5min Sonicated (solid lines) and No Sonication (dotted lines) samples (non-normalized data shown in Figure 5b).

There were notably a few samples that saw significant mass loss after sonication (Figure 4.6D, PM-NOM D9 L-B and L-C) but not a commensurate decrease in PNC, indicating that the fragile particles existed within the observable size range of the spICP-MS. Sonication then shattered these particles replenishing the PNC but reducing PMC by making their masses too small for the spICP-MS to detect.

The growth in PNC and PMC post-sonication for many samples was disproportionate (not 1:1) and in general PNC grew at a faster rate than PMC suggesting that most of the particles revealed by sonication were smaller sized. Figure 4.7 shows the normalized PNC for PM D7 samples A and B, demonstrating that PNC grows for smaller particles and drops for larger particles after sonication. Furthermore, both PNC and PMC for the PM suspension increased after sonication more than the PM-NOM suspension. For example, the PNC and PMC ratios of 32.7 and 3.22, respectively, measured post sonication for D11 C PM, compared to 7.19 and 2.15, respectively for D11 C PM-NOM. This finding suggests that more fragile particles exist in the PM sample than in the PM-NOM sample consistent with the observation that NOM decreases PM degradation rate. It would follow that any reduction in photodegradation rate would in turn reduce the amount of photoinduced fragile material in the PM-NOM samples.

These results also shed some explanation to the spikes in observed PNC for PM on D7 and D11 (Figure 4.3a), as well as PM-NOM on D11 (Figure 4.3b). Given the spICP-MS results measured for the non-sonicated/sonicated PM and PM-NOM samples (Figure 4.6), these spikes are now suspected to result from the presence of fragile material that was shattered into a larger number of particles.

4.4.3 Variable Sonication Time: Examination of the Magnitude of Photoinduced Fragility.

A repeat experiment was conducted with triplicate PM suspensions irradiated with 300nm wavelength light for 13 days. No PM-NOM suspensions were included in this repeat experiment. Analysis with spICP-MS was conducted immediately after sampling (no sonication), and then after 5min sonication. Additional measurements were made for later samples after 15min (D9, D11, D13) and 30min total sonication time (D13). Similar to the previous experiment, the non-sonicated (NS) particle number concentration (PNC) remained stable for 2 of 3 irradiated samples and the dark control (Figure 4.8a). PNC declined in sample C alone over the course of the irradiation. The constant PNC measured in the dark sample suggests that the PM suspension is colloidally stable, so the loss in sample C PNC most likely resulted from the irradiation alone, and may reflect sampling difficulties at low total PNC (see previous discussion).

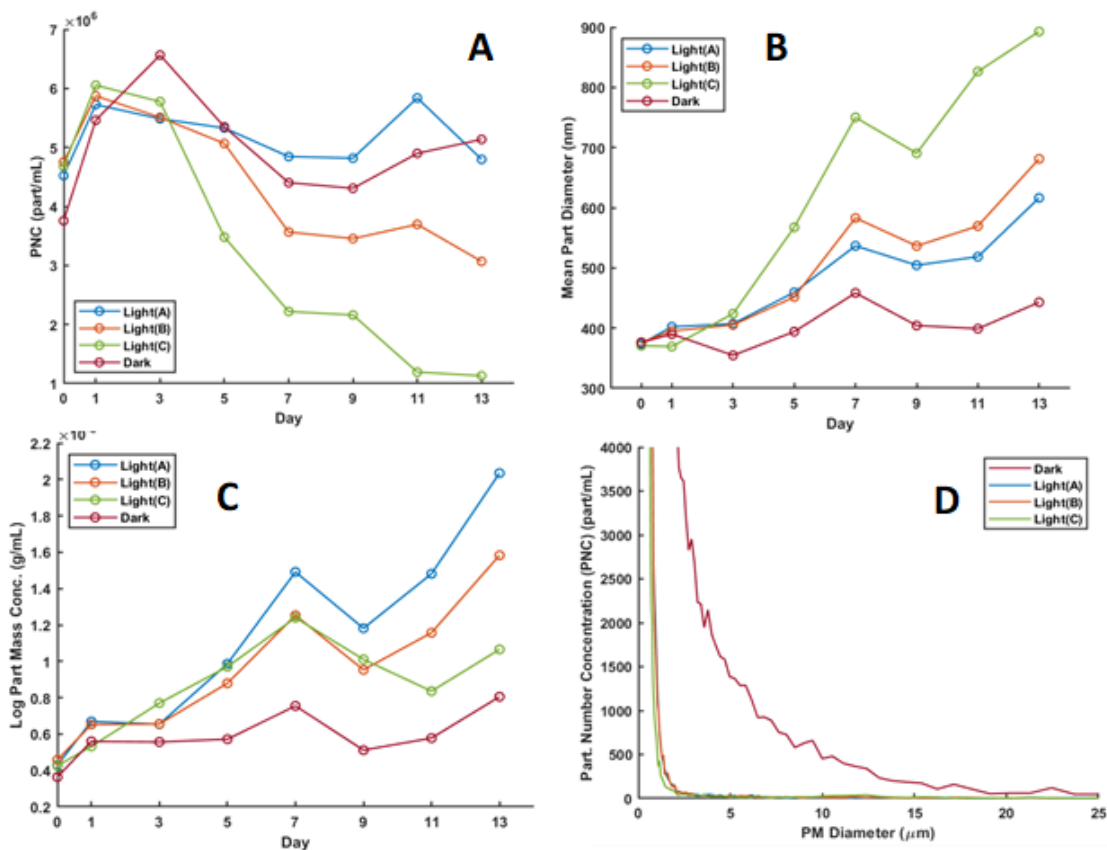


Figure 4-8 Non-Sonicated (NS) (a) Particle Number Concentration (part/mL), (b) Particle Mean Diameter, and (c) Particle Mass Concentration (PMC) as function of irradiation time measured by spICP-MS. Particle Diameters reflect an equivalent PM particle size to the 181Ta particle mass measured by spICP-MS. (d) Particle Number Concentration (PNC) as measured by SPOS on D13 for the three irradiated samples. PNC is corrected for the dilution factor and volume measured during the SPOS experiment.

In contrast to PNC, the NS mean particle diameter increases for all three irradiated samples (Light A, B, C; Figure 4.8b) and remains relatively constant for the dark control, consistent with previous results. Similarly, the particle mass concentration (PMC) (Figure 4.2a) of all three irradiated samples increased with irradiation time, while in the dark control remained constant. Furthermore, SPOS analysis of particles >2μm in diameter on D13 showed a decrease in measured particle numbers for the irradiated samples compared to the dark control. As with previous results, this demonstrates the progressive weathering of larger particles over the irradiation course. These results together suggest that the UV degradation of the PM samples is occurring in the same manner as the previous experiment, where material is progressively weathered into the highest range of the spICP-MS observable size range and lost at the lowest range.

Comparing the ratio of sonicated (SN) to non-sonicated (NS) PNC (SI Figure 4.15a) and PMC (SI Figure 4.15b), only two of the irradiated samples (D9 A and D13 C) showed ratios >1 suggesting the presence of fragile particles. Ratios exceeding 1 indicate that higher particle numbers and/or particle mass were measured post-sonication compared to without sonication which is hallmark of the existence of

fragile photodegraded material. The absence of PNC and PMC growth after sonication for most timepoints suggested that photodegradation had not sufficiently weakened the particles such that they could be fragments by a 5min sonication.

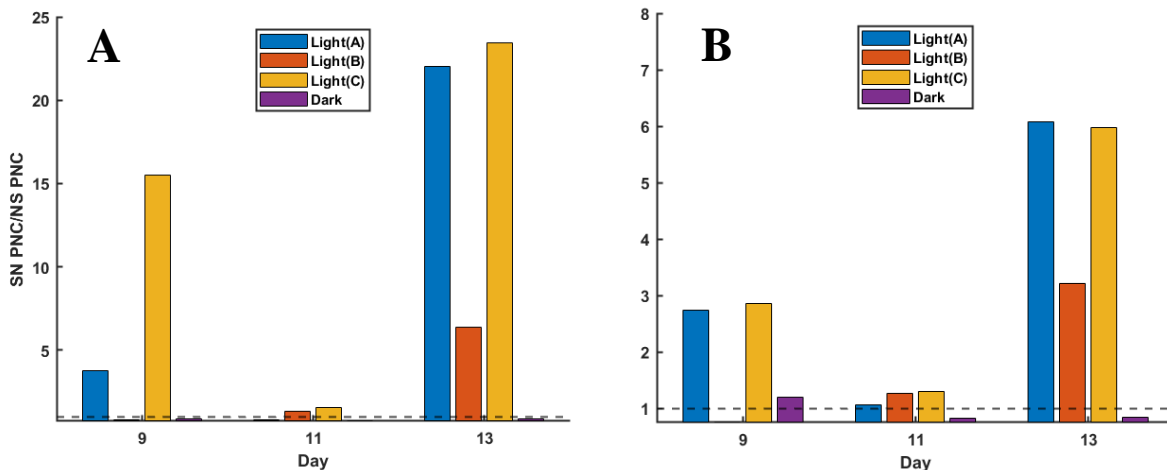


Figure 4-9 Ratio of sonicated (15min) to no sonication PNC (Panel A) and PMC (Panel B) measured by spICP-MS.

However, extending the pre-analysis sonication time to 15min for the D9, D11 and D13 samples caused increases in observed PNC and PMC ratios (Figure 4.9). In contrast to 5min of pre-spICP-MS sonication time, spICP-MS measurement after 15min sonication (ESN) showed PNC and PMC ratios >1 for most of the irradiated samples. Furthermore, in the few samples that saw an increase in PNC and PMC ratios after 5min sonication, additional sonication resulted in even larger changes. Importantly, observed PMC and PNC stayed relatively constant in the dark control (0.8-1.2) after 15min sonication, suggesting that the sonication itself is not creating fragile particles.

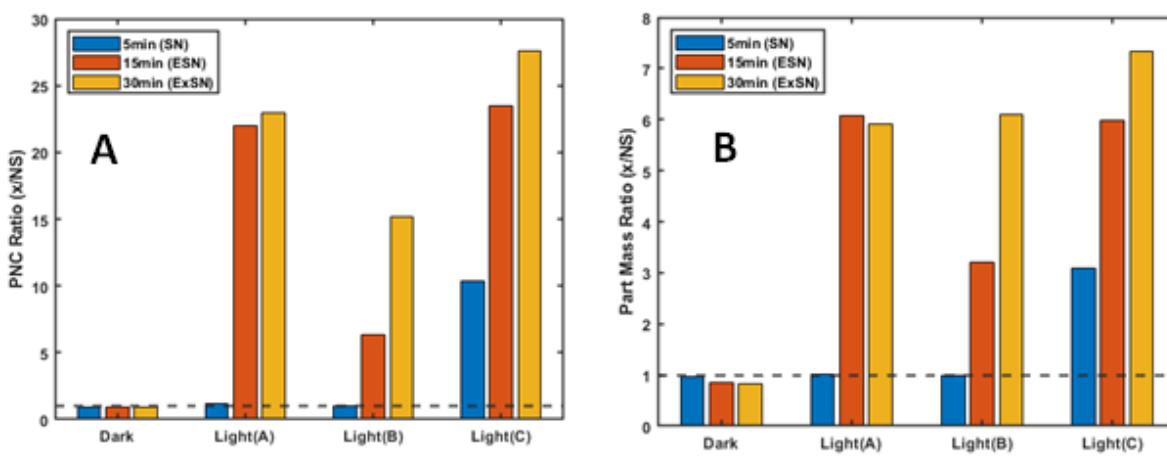


Figure 4-10 PNC (a) and PMC (b) from spICP-MS analysis of D13 samples where samples were sonicated for 0, 5, 15 and 30min prior to analysis.

By applying different levels of force, i.e., different sonication times, the degree of fragility in the photodegraded PM samples can be assessed. Figure 10 shows effect of variable sonication (5, 15 and 30min) on spICP-MS measurements of D13 samples where PNC and PMC are ratioed to NS. PNC and PMC ratios for the dark control were approximately 1, again suggesting that the PM material itself is not fragile without UV photodegradation. The three irradiated samples showed varying degrees of susceptibility to sonication. Sample A had relatively similar PNC and PMC ratios between 15 and 30min sonication suggesting that 15min sonication was sufficient to fully fragment any fragile material. In contrast, samples B and C showed increasing fragmentation with increasing sonication time.

Furthermore, extending this analysis to SPOS, we can see a similar effect (Figure 4.11). A 5min sonication prior to SPOS analysis increases the observed number of particles in all irradiated samples but not in the dark control, continuing trends seen with the spICP-MS measurements. Slightly more particles are measured in the dark control after 5min sonication and 30min sonication that may be attributable to resuspension of adsorbed materials.

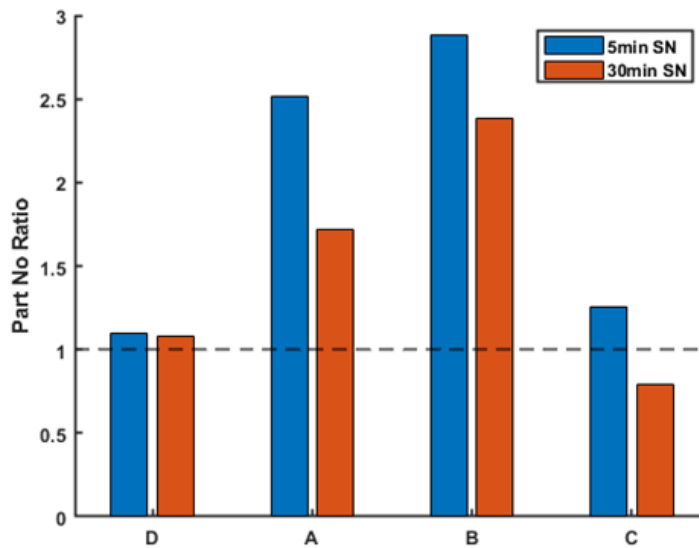


Figure 4-11 Ratio of Sonicated (5min or 30min) particle number to Non-Sonicated Particle no measured by SPOS.

The increase in particle numbers post-sonication of any length of time for the irradiated samples suggest that the hypothesized fragile material exists in this larger size range as well. Interestingly, a 30min sonication causes a reduction in particle numbers compared to the 5min sonication. This trend may represent the shattering of particles that exist in the sizable range of the SPOS ($>0.5\mu\text{m}$) such that they fall below the SPOS measurement range ($\approx 1-2\mu\text{m}$). This is supported by the spICP-MS, which measures particles $\geq 0.1\mu\text{m}$ in diameter and shows increasing particle numbers after a 30min sonication for the same D13 samples.

Sonication is presented as an accelerated weathering process akin to the mechanical forces experienced by plastic particles in many different environments[185], [197], [198]. This mechanical abrasion is an important step in the weathering process, accelerating the rate of plastic decay where photodegraded material is fragmented and lost, exposing new surface for photodegradation[21]. In this study, variable sonication times pre-analysis provides an additional information that allows the fragility of the nanoplastics to be interrogated in more detail. Using the growth in PMC post-sonication as a proxy for the amount of fragile material disturbed, by applying different amounts of force through varying sonication time, we can assess the fragility of each PM sample. For example, the largest growth in PMC after 5min sonication comes in sample C whereas samples A and B show no growth in PMC. This suggests that sample C is perhaps the most fragile of the three as it is the easiest to fragment with the lowest amount of force. Sample B has the lowest growth in PMC after 15min (ESN) sonication, leading to the samples being ranked $C > A > B$ from most fragile to least fragile. Interestingly, the PMC growth for the three samples after 30min (ExSN) of sonication is relatively similar with the ratio of ExSN PMC/NS PMC being within 6-7. This finding suggests that the three samples may have similar, total amounts of photodegraded material, but different susceptibility to sonication-induced fragmentation.

Through a combination of spICP-MS and SPOS we demonstrated the existence of particles made fragile by photodegradation and physically broken up through the pre-analysis application of mechanical force via sonication. The process of using different sonication times to probe the fragility of the particles is envisioned as a means of correlating qualitative observations about morphological or chemical changes into quantitative information. Sonication time could be calibrated to represent the amount of energy delivered by different environmental processes such as friction from wave motion[199, p. 20] or abrasion by mineral particles on beaches[198]. Metal-tagged nanoplastics exposed to UV degradation or other degradation processes could be studied through variable sonication times to judge their ability to fragment under these different environmental processes, or with other mechanical processes, such as freeze-thaw cycles.

4.4.4 Macroplastic Fragility Analysis by spICP-MS

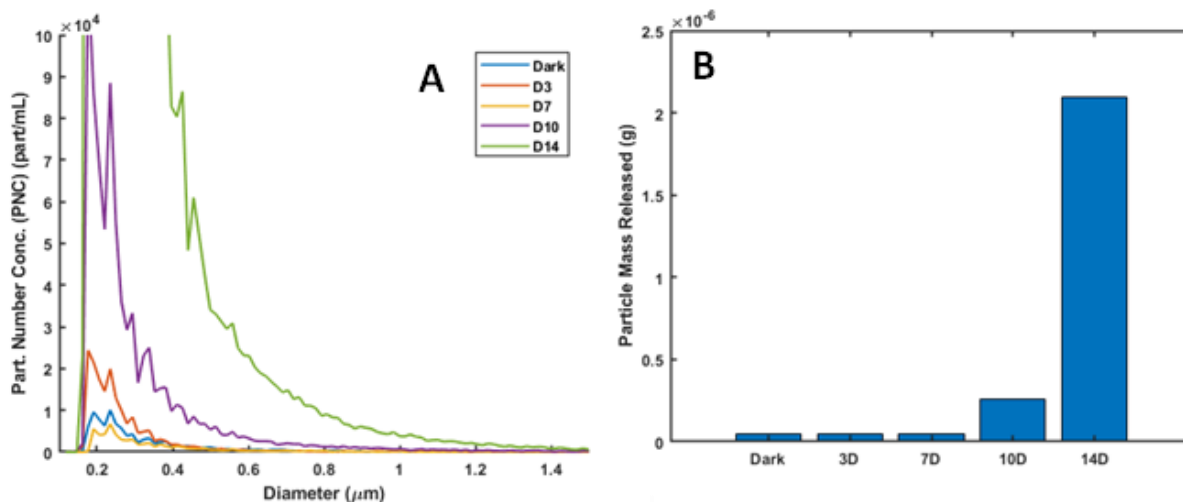


Figure 4-12 (A) Particle size distributions of nanoplastic released post-sonication for coupons UV irradiated for 0-14d. Each irradiation time has duplicates but only one PSD for each irradiation time is shown. (B) Average total PM particle mass released post-sonication. Average value of two coupons per irradiation time.

In addition to studying the photodegradation and fragility of particles, spICP-MS can be a useful tool for the study of the same phenomena in macroplastics. Ta-PM particles for the nanoplastic photodegradation experiment were produced through cryo-milling of tantalum-doped PM coupon. However, the coupon itself can be used as a substrate for photodegradation experiments as any particles that are shed during the degradation process will contain tantalum and thus will be detectable by spICP-MS.

PM coupons were irradiated in quartz tubes under 300nm light for variable amounts of time (0, 3, 7, 10 and 14 days), upon which time they were removed and immersed in np-H₂O for a period of 7 days to allow for passive particle release. After the initial release time, the coupons were removed and dried. Coupons were then rinsed in np-H₂O for 1D after which this rinse solution was removed. Afterwards, each coupon was immersed in a fresh aliquot of np-H₂O and sonicated for 30min in bath sonicator. Coupons were then allowed to passively release for 1D. The samples from the 7D post-irradiation soak (no sonication), 1D rinse and the post-30min sonication samples were then analyzed by spICP-MS.

PM particle release post irradiation over the 7D soak (pre-sonication) was negligible for all coupons, ranging from 0.611 to 1.77 $\times 10^{-9}$ g of PM particle mass released per coupon. The 1D rinse prior to sonication showed similar, negligible released amounts for all coupons ranging from 0.142-1.68 $\times 10^{-9}$ g released per coupon. PM particle release was amplified by sonication (Figure 4.12a) with larger amounts of particles and larger sizes of particles released with increasing irradiation time. Particle release for the

14D coupons (Figure 4.12b) averaged 2.1×10^{-6} g/coupon which was roughly 42x that released by the dark control (4.9×10^{-8} g/coupon) and 1200x what was released by the 14D coupon (1.77×10^{-9} g) in the pre-sonication 7D soak.

These results replicate previous studies in which photodegradation creates nano to millimeter sized mechanical deficiencies (voids) in the material[195] that can be exploited by mechanical force to fragment into micro(nano)plastics[183], [199], [200]. Mechanical force is one of the driving forces for plastic degradation[21], [197] and understanding its role in the progressive weathering of large plastic debris is essential to predicting nanoplastic release. This experimental framework could be extended to include both qualitative measurements of the macroplastic surface before and after degradation to correlate these measurements quantitatively to nanoplastic release. For example, the amount of PM mass released for the 3D and 7D coupons was comparable to the dark control, suggesting that a minimum amount of surface photodegradation is needed before the surface is fragile enough to be disrupted by sonication. The state of the surface could be confirmed using electron microscopy or the degree of photooxidation through techniques sensitive to changes in chemical groups such as FTIR. Lastly, the variable sonication used in the previous section to assess the possibility of particle fragmentation under mechanical stress could be extended here to examine surface fragility and how it relates to nanoplastic release in a quantitative way.

spICP-MS in combination with a metal doped substrate provides significant advantages as technique for measuring nanoplastic release in both sensitivity and particle counting. The detectable concentration of nanoplastic by spICP-MS in this study is order of magnitudes lower than other methods using weight loss[200] or total organic carbon (TOC) analysis[193] to follow the mass of nanoplastic released. The highest total measured mass of nanoplastic, 2.1×10^{-6} g, in this experiment would be exceptionally difficult to detect through mass loss of the original coupon or through TOC. However, the addition of 1% (w/w) of Ta-Ethoxide to this mass of polymer equates to 4.71×10^{-8} g of embedded Ta, which is easily detected by the spICP-MS. Furthermore, spICP-MS allows for the counting and sizing of particles at sizes smaller than optical microscopy[183] but larger than other nanosized single particle techniques such as NTA[200]. This enhanced size range plus the ability to rapidly count large numbers of particles makes this technique a standout analytical technique for the evaluation of nanoplastic release.

4.4.5 Overall Conclusions.

These results establish a basic framework for evaluating the photodegradation of metal-doped polymers using the spICP-MS. Photodegradation of PM was shown to generally conform to the conveyor belt hypothesis with smaller particles being eliminated from, and large particles being weathered into, the spICP-MS observable size range. Furthermore, NOM was demonstrated to be protective of PM particles against photodegradation as shown by the slower increase in observable mass and mean particle diameter

in irradiated PM-NOM samples compared to PM alone. Nanoplastic release from a macroplastic substrate was also measured using a similar framework, and that sonication, a stand-in for mechanical weathering, released greater amounts of nanoplastic dependent on the UV degradation of the surface.

4.5 Supporting Information.

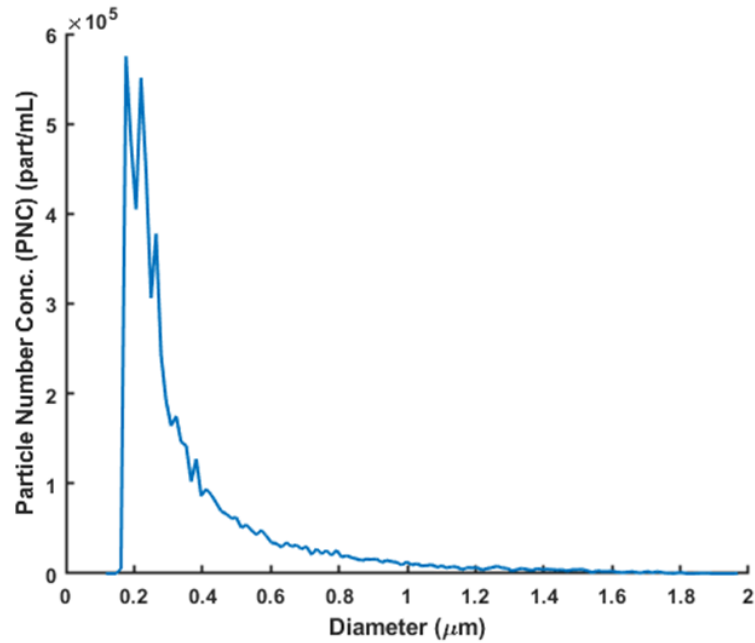


Figure 4-13 spICP-MS PSD of D0 PM Suspension. Particle number concentration corrected for transport efficiency and dilution factor. Particle diameters reflects an equivalently sized PM particle to the amount of ^{181}Ta mass detected by the spICP-MS.

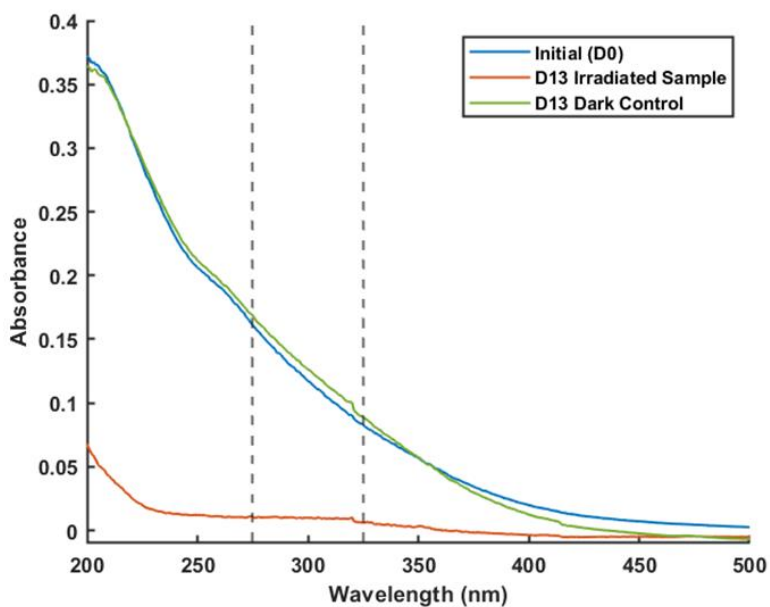


Figure 4-14 UV Absorbance of NOM control samples (no PM) at D0, and both the D13 Dark and Light Controls.

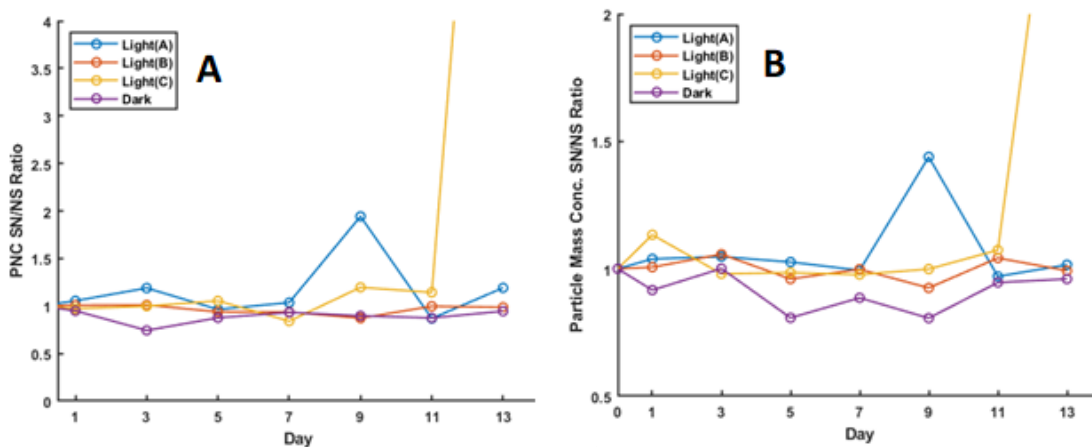


Figure 4-15 Ratio of PNC (Panel A) and PMC (Panel B) of Sonicated (5min) (SN) to No Sonication (NS) measured by spICP-MS over the irradiation course. The PNC and PMC values for D13 C that are off scale are 10.33 and 3.08, respectively.

5.1 Summary of Results and Implications

Expanding use of engineered nanomaterials in consumer products and the increased generation of incidental nanomaterials has concerningly increased the environmental concentrations of nanomaterials. Although there are numerous studies documenting the existence of engineered and incidental nanomaterials in the environment, they remain difficult to truly identify, characterize and quantify. Naturally occurring nanomaterials mask their presence, and their heterogeneity in size, chemical composition and shape confound efforts to successfully characterize them. Outside of their characterization, many questions remain about the fate of engineered and incidental nanomaterials in the environment and the ecological risks that they pose. Improvements in instrumentation and methodology have not necessarily translated to the ability to study the reactions that these materials participate in. The work in this thesis attempts to address the problems inherent in anthropogenic nanomaterials identification and quantitation, but also uses this knowledge to extend our ability to study their interactions with the environment.

Chapter 2 deals primarily with the question of identification, namely, how do we identify anthropogenic materials against a natural particle background that shares a chemical composition? For this example, zinc was chosen as the element of interest due to its incorporation in natural (minerals, hetero aggregates, etc.), incidental (tire wear, brake, emissions, etc.) and engineered (sunscreen, plastic additive, etc.) nanomaterials. The urban portion of the South Platte watershed in Denver, Colorado (USA) was sampled for zinc to identify and quantify different nanomaterial sources. Single particle ICP-QMS was employed, to provide single elemental (Zn) signals arising from particle detection events. Coupling this technique to sample pre-fractionation (sedimentation, filtration) provided additional information on the Zn speciation. Filtration demonstrated that the background concentration Zn comprised of both dissolved Zn species and particles with masses too small to be resolved by the spICP-QMS. The presence of larger particles containing only a small amount of Zn was demonstrated by sedimentation pre-spICP-MS analysis. Multi-element particle content was examined on a particle-by-particle basis using Single particle ICP-TOFMS (spICP-TOFMS), allowing for a more detailed speciation of the Zn particles discriminating between possibly anthropogenic and geogenic Zn-containing particles. Anthropogenic particles were hypothesized to have elemental compositions that were mostly Zn, representing the ZnO incorporated into many consumer goods (tires, sunscreens, etc.). Multi-metal particles, although possibly anthropogenic, were hypothesized to be geogenic in origin if Zn forms a minority of the total elemental content. Different sites in the South Platte watershed showed different proportions of these particles largely agreeing with the spICP-QMS results. The commonly utilized spICP-QMS and methodology used by environmental scientists demonstrates how careful application of pre-fractionation can provide

additional information about particle speciation. Although more widely known, spICP-TOFMS was in its infancy when this study was published in 2020, and this article is one of the first demonstrating its utility in speciating between anthropogenic and natural nanomaterials in a single sample.

With some insight into identification, Chapter 3 turns its focus to the issue of quantitation. Sampled nanomaterials can have broad, continuous, polydisperse particle size distributions that create analytical difficulties for many single particle techniques, including spICP-MS. Many of the standards used for spICP-MS methodological development are monodisperse and present few of the same analytical challenges. Employing environmentally relevant, metal-tagged nanoplastics, as well as environmental Al-bearing stream colloid samples, we demonstrate the deleterious effects of particle-based backgrounds caused by coincident small particles on spICP-MS analysis of particle number concentration (PNC) and particle size distribution (PSD). Novel methodology is proposed which can successfully minimize the effects of particle coincidence using serial dilutions to identify distortion-free segments of the PSD, which are combined and modeled using the power law. The physical relevance of the parameters derived from power law modeling are demonstrated using suspensions of two different nanoplastics. Finally, this new methodology is compared to a single dilution spICP-MS analysis of Al-bearing colloids sampled during a storm event to highlight the possible distortions in a single dilution analysis and demonstrates the value of our proposed methodology for environmental nanomaterial analysis. More accurate accounting of environmental colloid size distributions and mass could have beneficial effects in a wide variety of areas including more accurate chemical speciation calculation in the presence of colloids or calculation of nanomaterial dosage in particle toxicology.

Lastly, lessons from the previous two chapters were applied to study of the environmental processes that shape these polydisperse environmental colloids. UV photodegradation is one of the primary means of plastic weathering in the environment, and study of this process in nanoplastics has been hampered by the analytical difficulties posed by their size and carbon composition. Utilizing the same metal-tagged nanoplastic substrate from the previous chapter, we measured the UV photodegradation of polymethylmethacrylate (PM) nanoplastics. Unlike previous studies, the starting material contained an environmentally relevant, continuous polydisperse particle size distribution allowing for unique observations about the photodegradation process. A combination of spICP-MS and single particle optical sizing (SPOS) demonstrated that photolysis of PM plastic is a “conveyor belt”, where particles are progressively weathered to smaller and smaller sizes. The utility of this analytical approach was demonstrated through the addition of NOM which was shown to directly interact with the PM plastic and protect it from UV degradation. Notably, the novel use of Ta-tagged PM allowed for the study of the photodegradation process in the presence of a carbon background presented by the NOM. This methodology opens a new area of inquiry as nanoplastic research is regularly hampered by carbon backgrounds and this combination of metal-tagging and spICP-MS circumvents this particular problem.

Pre-analysis sonication of the photodegraded PM particles was shown to catalyze their fragmentation, unlike particles with no UV exposure. By varying the sonication time, different levels of particle fragility were demonstrated, providing the basis for estimating their propensity for the generation of additional particles through fracture. Finally, nanoplastic release from macroplastic coupons doped with Ta-additive was demonstrated, showing advantages in particle identification and sensitivity compared to other studies. Pre-analysis sonication was extended to these coupons demonstrating how a combination of UV photodegradation and mechanical force can be used to evaluate the potential for nanoplastic release. The possible applications of the methodology presented in this study are many, but a few will be discussed in more detail in future directions.

5.2 Future Avenues of Inquiry

Environmental colloids, a synthesis of particles of varied origin and chemical composition, present challenges in speciation, quantitation and characterization that are unlikely to be easily solved. The methodology presented in this thesis hopefully lays some guideposts to the identification of anthropogenic particles against a natural particle background (Chapter 2), the accurate quantification of broad polydisperse colloidal samples (Chapter 3) and the study of these polydisperse samples as they undergo environmental transformation (Chapter 4).

Power law distributions or particle number by particle size have been demonstrated as ubiquitous in the natural environment and deserve further examination. In chapter 3, a single power law model was used to fit the Al-colloid spICP-MS data with a degree of success. However, environmental colloids are an integration of particles from different sources, and each of these sources could create a particle population adhering to different power law or other particle number to size relationships. Therefore, a more accurate model might integrate multiple power laws each describing a different constituent of the colloid. Model substrates from different sources but similar elemental composition, such as ground minerals or particles from tire wear, could be individually characterized by spICP-MS and data fit with a unique model describing each particle size distribution. These model materials could be combined into the same sample, measured by spICP-MS and a mix of the individual models could be used to fit the data. The accuracy of a mix of models could be assessed, and if successful, this process could be extended to a sampled environmental colloid. In addition to spICP-MS, this sampled colloid could be examined with an orthogonal single particle technique such as Automated Mineralogy (SEM/EDX) or spICP-TOF-MS, which would be used for speciation. With some information on speciation in hand, a mix of power law models could be adapted to fit the spICP-MS data to increase its accuracy. As mentioned previously, more accurate estimates of particle size and number will lead to more accurate assessment of colloidal surface area or mass, which are essential in modeling their participation in adsorption or transport reactions.

One can imagine a seemingly infinite number of variations on the experimental methodology using a combination of metal-tagged plastics and spICP-MS presented in chapter 5. Plastic type has been already explored to some degree with polystyrene (PS) (results not presented here but likely included in a future publication), but metal tag incorporation in other plastic types, polyethylene, polypropylene, etc., is an easy expansion of this study. Furthermore, photodegradation under other wavelengths of light (UVC, UVA, solar spectrum) and other methods of nanoplastic degradation/generation (thermal, mechanical) could be studied. However, the principal advantage in this technique is that it allows for the identification of nanoplastic against a background. PM photodegradation in the presence of NOM was demonstrated in chapter 5, but this could be easily extended to other environmental matrices with complex composition. Photodegradation in surface waters sampled from marine environments, estuaries or other environments suffering from plastic pollution could be studied giving direct insight into the fate of nanoplastics in each of these environments. Different types of nanoplastic combined with NOM of different composition could be studied in tandem to look for both direct and indirect mechanisms of photolysis. Finally, as hinted by another publication studying the degradation of one nanoplastic in the presence of the other, mixes of nanoplastics could be studied in the same experiment with each type nanoplastic containing a different metal tag. The study of the environmental degradation in the presence of other organic species is perhaps the most timely and novel future application of this research.

REFERENCES

- [1] E. Roduner, "Size matters: why nanomaterials are different," *Chem. Soc. Rev.*, vol. 35, no. 7, p. 583, 2006, doi: 10.1039/b502142c.
- [2] M. F. Hochella *et al.*, "Natural, incidental, and engineered nanomaterials and their impacts on the Earth system," *Science*, vol. 363, no. 6434, p. eaau8299, Mar. 2019, doi: 10.1126/science.aau8299.
- [3] B. Gu, J. Schmitt, Z. Chen, L. Liang, and J. F. McCarthy, "Adsorption and desorption of different organic matter fractions on iron oxide," *Geochim. Cosmochim. Acta*, vol. 59, no. 2, pp. 219–229, Jan. 1995, doi: 10.1016/0016-7037(94)00282-Q.
- [4] M. F. Hochella, J. N. Moore, C. V. Putnis, A. Putnis, T. Kasama, and D. D. Eberl, "Direct observation of heavy metal-mineral association from the Clark Fork River Superfund Complex: Implications for metal transport and bioavailability," *Geochim. Cosmochim. Acta*, vol. 69, no. 7, pp. 1651–1663, Apr. 2005, doi: 10.1016/j.gca.2004.07.038.
- [5] P. P. Fu, Q. Xia, H.-M. Hwang, P. C. Ray, and H. Yu, "Mechanisms of nanotoxicity: Generation of reactive oxygen species," *J. Food Drug Anal.*, vol. 22, no. 1, pp. 64–75, Mar. 2014, doi: 10.1016/j.jfda.2014.01.005.
- [6] M. Baalousha *et al.*, "Outdoor urban nanomaterials: The emergence of a new, integrated, and critical field of study," *Sci. Total Environ.*, vol. 557–558, pp. 740–753, Jul. 2016, doi: 10.1016/j.scitotenv.2016.03.132.
- [7] M. Shakeel, F. Jabeen, S. Shabbir, M. S. Asghar, M. S. Khan, and A. S. Chaudhry, "Toxicity of Nano-Titanium Dioxide (TiO₂-NP) Through Various Routes of Exposure: a Review," *Biol. Trace Elem. Res.*, vol. 172, no. 1, pp. 1–36, Jul. 2016, doi: 10.1007/s12011-015-0550-x.
- [8] A. Weir, P. Westerhoff, L. Fabricius, K. Hristovski, and N. von Goetz, "Titanium Dioxide Nanoparticles in Food and Personal Care Products," *Environ. Sci. Technol.*, vol. 46, no. 4, pp. 2242–2250, Feb. 2012, doi: 10.1021/es204168d.
- [9] W. Shen, C. Zhang, Q. Li, W. Zhang, L. Cao, and J. Ye, "Preparation of titanium dioxide nano particle modified photocatalytic self-cleaning concrete," *J. Clean. Prod.*, vol. 87, pp. 762–765, Jan. 2015, doi: 10.1016/j.jclepro.2014.10.014.
- [10] A. N. Papadopoulos, D. N. Bikiaris, A. C. Mitropoulos, and G. Z. Kyzas, "Nanomaterials and Chemical Modifications for Enhanced Key Wood Properties: A Review," *Nanomaterials*, vol. 9, no. 4, Art. no. 4, Apr. 2019, doi: 10.3390/nano9040607.
- [11] S. K. Malyan, S. Yadav, V. Sonkar, V. C. Goyal, O. Singh, and R. Singh, "Mechanistic understanding of the pollutant removal and transformation processes in the constructed wetland system," *Water Environ. Res.*, vol. 93, no. 10, pp. 1882–1909, Oct. 2021, doi: 10.1002/wer.1599.
- [12] R. Gusain, K. Gupta, P. Joshi, and O. P. Khatri, "Adsorptive removal and photocatalytic degradation of organic pollutants using metal oxides and their composites: A comprehensive review," *Adv. Colloid Interface Sci.*, vol. 272, p. 102009, Oct. 2019, doi: 10.1016/j.cis.2019.102009.
- [13] A. Servin *et al.*, "A review of the use of engineered nanomaterials to suppress plant disease and enhance crop yield," *J. Nanoparticle Res.*, vol. 17, no. 2, p. 92, Feb. 2015, doi: 10.1007/s11051-015-2907-7.
- [14] M. Bundschuh *et al.*, "Nanoparticles in the environment: where do we come from, where do we go to?," *Environ. Sci. Eur.*, vol. 30, no. 1, p. 6, Feb. 2018, doi: 10.1186/s12302-018-0132-6.
- [15] P. Pant and R. M. Harrison, "Estimation of the contribution of road traffic emissions to particulate matter concentrations from field measurements: A review," *Atmos. Environ.*, vol. 77, pp. 78–97, Oct. 2013, doi: 10.1016/j.atmosenv.2013.04.028.

- [16] P. Klöckner, T. Reemtsma, P. Eisentraut, U. Braun, A. S. Ruhl, and S. Wagner, “Tire and road wear particles in road environment – Quantification and assessment of particle dynamics by Zn determination after density separation,” *Chemosphere*, vol. 222, pp. 714–721, May 2019, doi: 10.1016/j.chemosphere.2019.01.176.
- [17] A. Dahl *et al.*, “Traffic-generated emissions of ultrafine particles from pavement–tire interface,” *Atmos. Environ.*, vol. 40, no. 7, pp. 1314–1323, Mar. 2006, doi: 10.1016/j.atmosenv.2005.10.029.
- [18] Z. Tian *et al.*, “A ubiquitous tire rubber–derived chemical induces acute mortality in coho salmon,” *Science*, vol. 371, no. 6525, pp. 185–189, Jan. 2021, doi: 10.1126/science.abd6951.
- [19] “Plastic production worldwide 2021,” *Statista*. <https://www.statista.com/statistics/282732/global-production-of-plastics-since-1950/> (accessed Apr. 18, 2023).
- [20] R. Geyer, J. R. Jambeck, and K. L. Law, “Production, use, and fate of all plastics ever made,” *Sci. Adv.*, vol. 3, no. 7, p. e1700782, Jul. 2017, doi: 10.1126/sciadv.1700782.
- [21] A. ter Halle, L. Ladirat, M. Martignac, A. F. Mingotaud, O. Boyron, and E. Perez, “To what extent are microplastics from the open ocean weathered?,” *Environ. Pollut.*, vol. 227, pp. 167–174, Aug. 2017, doi: 10.1016/j.envpol.2017.04.051.
- [22] B. Gewert, M. M. Plassmann, and M. MacLeod, “Pathways for degradation of plastic polymers floating in the marine environment,” *Environ. Sci. Process. Impacts*, vol. 17, no. 9, pp. 1513–1521, 2015, doi: 10.1039/C5EM00207A.
- [23] A. L. Dawson *et al.*, “Turning microplastics into nanoplastics through digestive fragmentation by Antarctic krill,” *Nat. Commun.*, vol. 9, no. 1, Art. no. 1, Mar. 2018, doi: 10.1038/s41467-018-03465-9.
- [24] J. Ru, Y. Huo, and Y. Yang, “Microbial Degradation and Valorization of Plastic Wastes,” *Front. Microbiol.*, vol. 11, 2020, Accessed: Apr. 28, 2023. [Online]. Available: <https://www.frontiersin.org/articles/10.3389/fmicb.2020.00442>
- [25] J. Gigault *et al.*, “Nanoplastics are neither microplastics nor engineered nanoparticles,” *Nat. Nanotechnol.*, vol. 16, no. 5, pp. 501–507, May 2021, doi: 10.1038/s41565-021-00886-4.
- [26] H. Ma, S. Pu, S. Liu, Y. Bai, S. Mandal, and B. Xing, “Microplastics in aquatic environments: Toxicity to trigger ecological consequences,” *Environ. Pollut.*, vol. 261, p. 114089, Jun. 2020, doi: 10.1016/j.envpol.2020.114089.
- [27] M. Hoch, “Organotin compounds in the environment – an overview,” *Appl. Geochem.*, p. 25, 2001.
- [28] C. Chen, L. Chen, Y. Yao, F. Artigas, Q. Huang, and W. Zhang, “Organotin Release from Polyvinyl Chloride Microplastics and Concurrent Photodegradation in Water: Impacts from Salinity, Dissolved Organic Matter, and Light Exposure,” *Environ. Sci. Technol.*, vol. 53, no. 18, pp. 10741–10752, Sep. 2019, doi: 10.1021/acs.est.9b03428.
- [29] F. Caputo *et al.*, “Measuring particle size distribution and mass concentration of nanoplastics and microplastics: addressing some analytical challenges in the sub-micron size range,” *J. Colloid Interface Sci.*, vol. 588, pp. 401–417, Apr. 2021, doi: 10.1016/j.jcis.2020.12.039.
- [30] M. Zhang *et al.*, “Detection of engineered nanoparticles in aquatic environments: current status and challenges in enrichment, separation, and analysis,” *Environ. Sci. Nano*, vol. 6, no. 3, pp. 709–735, 2019, doi: 10.1039/C8EN01086B.
- [31] “Abundance of elements in Earth’s crust,” *Wikipedia*. Mar. 24, 2023. Accessed: Apr. 20, 2023. [Online]. Available: https://en.wikipedia.org/w/index.php?title=Abundance_of_elements_in_Earth%27s_crust&oldid=1146443928#cite_note-7

- [32] A. Praetorius *et al.*, “Single-particle multi-element fingerprinting (spMEF) using inductively-coupled plasma time-of-flight mass spectrometry (ICP-TOFMS) to identify engineered nanoparticles against the elevated natural background in soils,” *Environ. Sci. Nano*, vol. 4, no. 2, pp. 307–314, Feb. 2017, doi: 10.1039/C6EN00455E.
- [33] F. Loosli *et al.*, “Sewage spills are a major source of titanium dioxide engineered (nano)-particle release into the environment,” *Environ. Sci. Nano*, vol. 6, no. 3, pp. 763–777, Mar. 2019, doi: 10.1039/C8EN01376D.
- [34] O. US EPA, “Drinking Water Regulations,” Sep. 21, 2015. <https://www.epa.gov/dwreginfo/drinking-water-regulations> (accessed Apr. 22, 2023).
- [35] H.-S. Kwon, M. H. Ryu, and C. Carlsten, “Ultrafine particles: unique physicochemical properties relevant to health and disease,” *Exp. Mol. Med.*, vol. 52, no. 3, pp. 318–328, Mar. 2020, doi: 10.1038/s12276-020-0405-1.
- [36] H. M. Braakhuis, M. V. Park, I. Gosens, W. H. De Jong, and F. R. Cassee, “Physicochemical characteristics of nanomaterials that affect pulmonary inflammation,” *Part. Fibre Toxicol.*, vol. 11, no. 1, p. 18, Apr. 2014, doi: 10.1186/1743-8977-11-18.
- [37] D. E. Schraufnagel, “The health effects of ultrafine particles,” *Exp. Mol. Med.*, vol. 52, no. 3, pp. 311–317, Mar. 2020, doi: 10.1038/s12276-020-0403-3.
- [38] M. Hassellöv, J. W. Readman, J. F. Ranville, and K. Tiede, “Nanoparticle analysis and characterization methodologies in environmental risk assessment of engineered nanoparticles,” *Ecotoxicology*, vol. 17, no. 5, pp. 344–361, Jul. 2008, doi: 10.1007/s10646-008-0225-x.
- [39] K. W. Powers, S. C. Brown, V. B. Krishna, S. C. Wasdo, B. M. Moudgil, and S. M. Roberts, “Research Strategies for Safety Evaluation of Nanomaterials. Part VI. Characterization of Nanoscale Particles for Toxicological Evaluation,” *Toxicol. Sci.*, vol. 90, no. 2, pp. 296–303, Apr. 2006, doi: 10.1093/toxsci/kfj099.
- [40] B. J. Berne and R. Pecora, *Dynamic Light Scattering: With Applications to Chemistry, Biology, and Physics*. Courier Corporation, 2000.
- [41] M. E. Schimpf, K. Caldwell, and J. C. Giddings, *Field-Flow Fractionation Handbook*. John Wiley & Sons, 2000.
- [42] J. Gigault, J. M. Pettibone, C. Schmitt, and V. A. Hackley, “Rational strategy for characterization of nanoscale particles by asymmetric-flow field flow fractionation: A tutorial,” *Anal. Chim. Acta*, vol. 809, pp. 9–24, Jan. 2014, doi: 10.1016/j.aca.2013.11.021.
- [43] M. Baalousha, B. Stolpe, and J. R. Lead, “Flow field-flow fractionation for the analysis and characterization of natural colloids and manufactured nanoparticles in environmental systems: A critical review,” *J. Chromatogr. A*, vol. 1218, no. 27, pp. 4078–4103, Jul. 2011, doi: 10.1016/j.chroma.2011.04.063.
- [44] C. W. Cuss *et al.*, “Measuring the distribution of trace elements amongst dissolved colloidal species as a fingerprint for the contribution of tributaries to large boreal rivers,” *Sci. Total Environ.*, vol. 642, pp. 1242–1251, Nov. 2018, doi: 10.1016/j.scitotenv.2018.06.099.
- [45] A. Philippe and G. E. Schaumann, “Evaluation of Hydrodynamic Chromatography Coupled with UV-Visible, Fluorescence and Inductively Coupled Plasma Mass Spectrometry Detectors for Sizing and Quantifying Colloids in Environmental Media,” *PLOS ONE*, vol. 9, no. 2, p. e90559, Feb. 2014, doi: 10.1371/journal.pone.0090559.
- [46] B. Kowalczyk, I. Lagzi, and B. A. Grzybowski, “Nanoseparations: Strategies for size and/or shape-selective purification of nanoparticles,” *Curr. Opin. Colloid Interface Sci.*, vol. 16, no. 2, pp. 135–148, Apr. 2011, doi: 10.1016/j.cocis.2011.01.004.

- [47] K. L. Planken and H. Cölfen, “Analytical ultracentrifugation of colloids,” *Nanoscale*, vol. 2, no. 10, pp. 1849–1869, 2010, doi: 10.1039/C0NR00215A.
- [48] M. Kamiti, D. Boldridge, L. M. Ndoping, and E. E. Remsen, “Simultaneous Absolute Determination of Particle Size and Effective Density of Submicron Colloids by Disc Centrifuge Photosedimentometry,” *Anal. Chem.*, vol. 84, no. 24, pp. 10526–10530, Dec. 2012, doi: 10.1021/ac3022086.
- [49] R. F. Egerton, *Physical Principles of Electron Microscopy*. Cham: Springer International Publishing, 2016. doi: 10.1007/978-3-319-39877-8.
- [50] K. Eitel, G. Bryant, and H. J. Schöpe, “A Hitchhiker’s Guide to Particle Sizing Techniques,” *Langmuir*, vol. 36, no. 35, pp. 10307–10320, Sep. 2020, doi: 10.1021/acs.langmuir.0c00709.
- [51] S. B. Rice *et al.*, “Particle size distributions by transmission electron microscopy: an interlaboratory comparison case study,” *Metrologia*, vol. 50, no. 6, pp. 663–678, Dec. 2013, doi: 10.1088/0026-1394/50/6/663.
- [52] “Introduction to Nanoparticle Tracking Analysis (NTA)”.
- [53] V. Filipe, A. Hawe, and W. Jiskoot, “Critical Evaluation of Nanoparticle Tracking Analysis (NTA) by NanoSight for the Measurement of Nanoparticles and Protein Aggregates,” *Pharm. Res.*, vol. 27, no. 5, pp. 796–810, May 2010, doi: 10.1007/s11095-010-0073-2.
- [54] J. A. Gallego-Urrea, J. Tuoriniemi, and M. Hassellöv, “Applications of particle-tracking analysis to the determination of size distributions and concentrations of nanoparticles in environmental, biological and food samples,” *TrAC Trends Anal. Chem.*, vol. 30, no. 3, pp. 473–483, Mar. 2011, doi: 10.1016/j.trac.2011.01.005.
- [55] R. F. Domingos *et al.*, “Characterizing Manufactured Nanoparticles in the Environment: Multimethod Determination of Particle Sizes,” *Environ. Sci. Technol.*, vol. 43, no. 19, pp. 7277–7284, Oct. 2009, doi: 10.1021/es900249m.
- [56] E. J. Petersen *et al.*, “Determining what really counts: modeling and measuring nanoparticle number concentrations,” *Environ. Sci. Nano*, vol. 6, no. 9, pp. 2876–2896, 2019, doi: 10.1039/C9EN00462A.
- [57] E. Bolea *et al.*, “Analytical applications of single particle inductively coupled plasma mass spectrometry: a comprehensive and critical review,” *Anal. Methods*, vol. 13, no. 25, pp. 2742–2795, Jul. 2021, doi: 10.1039/D1AY00761K.
- [58] S. Lee, X. Bi, R. B. Reed, J. F. Ranville, P. Herckes, and P. Westerhoff, “Nanoparticle Size Detection Limits by Single Particle ICP-MS for 40 Elements,” *Environ. Sci. Technol.*, vol. 48, no. 17, pp. 10291–10300, Sep. 2014, doi: 10.1021/es502422v.
- [59] M. D. Montañó, B. J. Majestic, Å. K. Jämting, P. Westerhoff, and J. F. Ranville, “Methods for the Detection and Characterization of Silica Colloids by Microsecond spICP-MS,” *Anal. Chem.*, vol. 88, no. 9, pp. 4733–4741, May 2016, doi: 10.1021/acs.analchem.5b04924.
- [60] I. Abad-Álvarez, E. Peña-Vázquez, E. Bolea, P. Bermejo-Barrera, J. R. Castillo, and F. Laborda, “Evaluation of number concentration quantification by single-particle inductively coupled plasma mass spectrometry: microsecond vs. millisecond dwell times,” *Anal. Bioanal. Chem.*, vol. 408, no. 19, pp. 5089–5097, Jul. 2016, doi: 10.1007/s00216-016-9515-y.
- [61] M. Mansor *et al.*, “Application of Single-Particle ICP-MS to Determine the Mass Distribution and Number Concentrations of Environmental Nanoparticles and Colloids,” *Environ. Sci. Technol. Lett.*, vol. 8, no. 7, pp. 589–595, Jul. 2021, doi: 10.1021/acs.estlett.1c00314.
- [62] K. A. Huynh, E. Siska, E. Heithmar, S. Tadjiki, and S. A. Pergantis, “Detection and Quantification of Silver Nanoparticles at Environmentally Relevant Concentrations Using Asymmetric Flow Field–

- Flow Fractionation Online with Single Particle Inductively Coupled Plasma Mass Spectrometry,” *Anal. Chem.*, vol. 88, no. 9, pp. 4909–4916, May 2016, doi: 10.1021/acs.analchem.6b00764.
- [63] L. Fréchette-Viens, M. Hadioui, and K. J. Wilkinson, “Quantification of ZnO nanoparticles and other Zn containing colloids in natural waters using a high sensitivity single particle ICP-MS,” *Talanta*, vol. 200, pp. 156–162, Aug. 2019, doi: 10.1016/j.talanta.2019.03.041.
- [64] F. Laborda, C. Trujillo, and R. Lobinski, “Analysis of microplastics in consumer products by single particle-inductively coupled plasma mass spectrometry using the carbon-13 isotope,” *Talanta*, vol. 221, p. 121486, Jan. 2021, doi: 10.1016/j.talanta.2020.121486.
- [65] M. D. Montaña, J. W. Olesik, A. G. Barber, K. Challis, and J. F. Ranville, “Single Particle ICP-MS: Advances toward routine analysis of nanomaterials,” *Anal. Bioanal. Chem.*, vol. 408, no. 19, pp. 5053–5074, Jul. 2016, doi: 10.1007/s00216-016-9676-8.
- [66] R. C. Merrifield, C. Stephan, and J. R. Lead, “Quantification of Au Nanoparticle Biouptake and Distribution to Freshwater Algae Using Single Cell – ICP-MS,” *Env. Sci Technol.*, p. 7, 2018.
- [67] S. Bevers, M. Montaña, L. Rybicki, T. Hofmann, F. von der Kammer, and J. Ranville, “Quantification and Characterization of Nanoparticulate Zinc in an Urban Watershed,” *Front. Environ. Sci. Biogeochem. Dyn.*, vol. 8, Jun. 2020, doi: 10.3389/fenvs.2020.00084.
- [68] S. Naasz *et al.*, “Multi-element analysis of single nanoparticles by ICP-MS using quadrupole and time-of-flight technologies,” *J. Anal. At. Spectrom.*, vol. 33, no. 5, pp. 835–845, May 2018, doi: 10.1039/C7JA00399D.
- [69] A. J. Goodman, A. Gundlach-Graham, S. G. Bevers, and J. F. Ranville, “Characterization of nano-scale mineral dust aerosols in snow by single particle inductively coupled plasma mass spectrometry,” *Environ. Sci. Nano*, vol. 9, no. 8, pp. 2638–2652, Aug. 2022, doi: 10.1039/D2EN00277A.
- [70] “AccuSizer® A7000 Single Particle Optical Sizing”.
- [71] T. Ito, L. Sun, M. A. Bevan, and R. M. Crooks, “Comparison of Nanoparticle Size and Electrophoretic Mobility Measurements Using a Carbon-Nanotube-Based Coulter Counter, Dynamic Light Scattering, Transmission Electron Microscopy, and Phase Analysis Light Scattering,” *Langmuir*, vol. 20, no. 16, pp. 6940–6945, Aug. 2004, doi: 10.1021/la049524t.
- [72] “Coulter Principle, Counting and Sizing Particles.”
<https://www.beckman.com/resources/technologies/flow-cytometry/history/coulter-principle> (accessed Apr. 19, 2023).
- [73] B. Tolla and D. Boldridge, “Distortion of Single-Particle Optical Sensing (SPOS) Particle Count by Sub-Countable Particles,” *Part. Part. Syst. Charact.*, vol. 27, no. 1–2, pp. 21–31, 2010, doi: 10.1002/ppsc.200900081.
- [74] E. J. W. Wynn and M. J. Hounslow, “Coincidence correction for electrical-zone (Coulter-counter) particle size analysers,” *Powder Technol.*, vol. 93, no. 2, pp. 163–175, Oct. 1997, doi: 10.1016/S0032-5910(97)03267-1.
- [75] H. E. Pace *et al.*, “Single Particle Inductively Coupled Plasma-Mass Spectrometry: A Performance Evaluation and Method Comparison in the Determination of Nanoparticle Size,” *Environ. Sci. Technol.*, vol. 46, no. 22, pp. 12272–12280, Nov. 2012, doi: 10.1021/es301787d.
- [76] J. Liu, K. E. Murphy, R. I. MacCuspie, and M. R. Winchester, “Capabilities of Single Particle Inductively Coupled Plasma Mass Spectrometry for the Size Measurement of Nanoparticles: A Case Study on Gold Nanoparticles,” *Anal. Chem.*, vol. 86, no. 7, pp. 3405–3414, Apr. 2014, doi: 10.1021/ac403775a.

- [77] W. Anderson, D. Kozak, V. A. Coleman, Å. K. Jämting, and M. Trau, “A comparative study of submicron particle sizing platforms: Accuracy, precision and resolution analysis of polydisperse particle size distributions,” *J. Colloid Interface Sci.*, vol. 405, pp. 322–330, Sep. 2013, doi: 10.1016/j.jcis.2013.02.030.
- [78] N. C. Bell, C. Minelli, J. Tompkins, M. M. Stevens, and A. G. Shard, “Emerging Techniques for Submicrometer Particle Sizing Applied to Stöber Silica,” *Langmuir*, vol. 28, no. 29, pp. 10860–10872, Jul. 2012, doi: 10.1021/la301351k.
- [79] J. Buffle and G. G. Leppard, “Characterization of Aquatic Colloids and Macromolecules. 1. Structure and Behavior of Colloidal Material,” *Environ. Sci. Technol.*, vol. 29, no. 9, pp. 2169–2175, Sep. 1995, doi: 10.1021/es00009a004.
- [80] C. Junge, “THE SIZE DISTRIBUTION AND AGING OF NATURAL AEROSOLS AS DETERMINED FROM ELECTRICAL AND OPTICAL DATA ON THE ATMOSPHERE,” *J. Atmospheric Sci.*, vol. 12, no. 1, pp. 13–25, Feb. 1955, doi: 10.1175/1520-0469(1955)012<0013:TSDAAO>2.0.CO;2.
- [81] M. Bittelli, G. S. Campbell, and M. Flury, “Characterization of Particle-Size Distribution in Soils with a Fragmentation Model,” *Soil Sci. Soc. Am. J.*, vol. 63, no. 4, pp. 782–788, Jul. 1999, doi: 10.2136/sssaj1999.634782x.
- [82] D. M. Mitrano, A. Beltzung, S. Frehland, M. Schmiedgruber, A. Cingolani, and F. Schmidt, “Synthesis of metal-doped nanoplastics and their utility to investigate fate and behaviour in complex environmental systems,” *Nat. Nanotechnol.*, vol. 14, no. 4, pp. 362–368, Apr. 2019, doi: 10.1038/s41565-018-0360-3.
- [83] Z. Liu *et al.*, “Quantifying the Dynamics of Polystyrene Microplastics UV-Aging Process,” *Environ. Sci. Technol. Lett.*, vol. 9, no. 1, pp. 50–56, Jan. 2022, doi: 10.1021/acs.estlett.1c00888.
- [84] Y. Zheng, L. Mutzner, C. Ort, R. Kaegi, and F. Gottschalk, “Modelling engineered nanomaterials in wet-weather discharges,” *NanoImpact*, vol. 16, p. 100188, Apr. 2019, doi: 10.1016/j.impact.2019.100188.
- [85] W. D. Shuster, J. Bonta, H. Thurston, E. Warnemuende, and D. R. Smith, “Impacts of impervious surface on watershed hydrology: A review,” *Urban Water J.*, vol. 2, no. 4, pp. 263–275, Dec. 2005, doi: 10.1080/15730620500386529.
- [86] K. Lamprea, A. Bressy, C. Mirande-Bret, E. Caupos, and M.-C. Gromaire, “Alkylphenol and bisphenol A contamination of urban runoff: an evaluation of the emission potentials of various construction materials and automotive supplies,” *Environ. Sci. Pollut. Res.*, vol. 25, no. 22, pp. 21887–21900, Aug. 2018, doi: 10.1007/s11356-018-2272-z.
- [87] X. Zuo, D. Fu, and H. Li, “Speciation distribution and mass balance of copper and zinc in urban rain, sediments, and road runoff,” *Environ. Sci. Pollut. Res.*, vol. 19, no. 9, pp. 4042–4048, Nov. 2012, doi: 10.1007/s11356-012-0907-z.
- [88] G. S. Toor, M. L. Occhipinti, Y.-Y. Yang, T. Majcherek, D. Haver, and L. Oki, “Managing urban runoff in residential neighborhoods: Nitrogen and phosphorus in lawn irrigation driven runoff,” *PLOS ONE*, vol. 12, no. 6, p. e0179151, Jun. 2017, doi: 10.1371/journal.pone.0179151.
- [89] A. Young, V. Kochenkov, J. K. McIntyre, J. D. Stark, and A. B. Coffin, “Urban stormwater runoff negatively impacts lateral line development in larval zebrafish and salmon embryos,” *Sci. Rep.*, vol. 8, no. 1, Art. no. 1, Feb. 2018, doi: 10.1038/s41598-018-21209-z.
- [90] C. O. Hendren, X. Mesnard, J. Dröge, and M. R. Wiesner, “Estimating Production Data for Five Engineered Nanomaterials As a Basis for Exposure Assessment,” *Environ. Sci. Technol.*, vol. 45, no. 7, pp. 2562–2569, Apr. 2011, doi: 10.1021/es103300g.

- [91] T. Y. Sun, D. M. Mitrano, N. A. Bornhöft, M. Scheringer, K. Hungerbühler, and B. Nowack, “Envisioning Nano Release Dynamics in a Changing World: Using Dynamic Probabilistic Modeling to Assess Future Environmental Emissions of Engineered Nanomaterials,” *Environ. Sci. Technol.*, vol. 51, no. 5, pp. 2854–2863, Mar. 2017, doi: 10.1021/acs.est.6b05702.
- [92] B. Giese *et al.*, “Risks, Release and Concentrations of Engineered Nanomaterial in the Environment,” *Sci. Rep.*, vol. 8, no. 1, Art. no. 1, Jan. 2018, doi: 10.1038/s41598-018-19275-4.
- [93] T. Gonet and B. A. Maher, “Airborne, Vehicle-Derived Fe-Bearing Nanoparticles in the Urban Environment: A Review,” *Environ. Sci. Technol.*, vol. 53, no. 17, pp. 9970–9991, Sep. 2019, doi: 10.1021/acs.est.9b01505.
- [94] F. Sommer *et al.*, “Tire Abrasion as a Major Source of Microplastics in the Environment,” *Aerosol Air Qual. Res.*, vol. 18, no. 8, pp. 2014–2028, 2018, doi: 10.4209/aaqr.2018.03.0099.
- [95] Y. Yang, M. Vance, F. Tou, A. Tiwari, M. Liu, and M. F. Hochella, “Nanoparticles in road dust from impervious urban surfaces: distribution, identification, and environmental implications,” *Environ. Sci. Nano*, vol. 3, no. 3, pp. 534–544, 2016, doi: 10.1039/C6EN00056H.
- [96] M. F. Hochella *et al.*, “Nanominerals, Mineral Nanoparticles, and Earth Systems,” *Science*, vol. 319, no. 5870, pp. 1631–1635, Mar. 2008, doi: 10.1126/science.1141134.
- [97] F. Piccinno, F. Gottschalk, S. Seeger, and B. Nowack, “Industrial production quantities and uses of ten engineered nanomaterials in Europe and the world,” *J. Nanoparticle Res.*, vol. 14, no. 9, p. 1109, Aug. 2012, doi: 10.1007/s11051-012-1109-9.
- [98] M. Milani, F. P. Pucillo, M. Ballerini, M. Camatini, M. Gualtieri, and S. Martino, “First evidence of tyre debris characterization at the nanoscale by focused ion beam,” *Mater. Charact.*, vol. 52, no. 4, pp. 283–288, Jul. 2004, doi: 10.1016/j.matchar.2004.06.001.
- [99] B. Herzog, S. Mongiat, C. Deshayes, M. Neuhaus, K. Sommer, and A. Mantler, “In vivo and in vitro assessment of UVA protection by sunscreen formulations containing either butyl methoxy dibenzoyl methane, methylene bis-benzotriazolyl tetramethylbutylphenol, or microfine ZnO,” *Int. J. Cosmet. Sci.*, vol. 24, no. 3, pp. 170–185, 2002, doi: 10.1046/j.1467-2494.2002.00137.x.
- [100] M. J. Osmond and M. J. McCall, “Zinc oxide nanoparticles in modern sunscreens: An analysis of potential exposure and hazard,” *Nanotoxicology*, vol. 4, no. 1, pp. 15–41, Mar. 2010, doi: 10.3109/17435390903502028.
- [101] J.-P. Kaiser, S. Zuin, and P. Wick, “Is nanotechnology revolutionizing the paint and lacquer industry? A critical opinion,” *Sci. Total Environ.*, vol. 442, pp. 282–289, Jan. 2013, doi: 10.1016/j.scitotenv.2012.10.009.
- [102] T. B. Councell, K. U. Duckenfield, E. R. Landa, and E. Callender, “Tire-Wear Particles as a Source of Zinc to the Environment,” *Environ. Sci. Technol.*, vol. 38, no. 15, pp. 4206–4214, Aug. 2004, doi: 10.1021/es034631f.
- [103] M. S. Ermolin, P. S. Fedotov, A. I. Ivaneev, V. K. Karandashev, N. N. Fedyunina, and V. V. Eskina, “Isolation and quantitative analysis of road dust nanoparticles,” *J. Anal. Chem.*, vol. 72, no. 5, pp. 520–532, May 2017, doi: 10.1134/S1061934817050057.
- [104] “Application of U.S. EPA guidelines in a bioavailability-based assessment of ambient water quality criteria for zinc in freshwater - DeForest - 2012 - Environmental Toxicology and Chemistry - Wiley Online Library.” <https://setac.onlinelibrary.wiley.com/doi/full/10.1002/etc.1810> (accessed May 01, 2023).
- [105] L. M. Furtado *et al.*, “The persistence and transformation of silver nanoparticles in littoral lake mesocosms monitored using various analytical techniques,” *Environ. Chem.*, vol. 11, no. 4, pp. 419–430, Aug. 2014, doi: 10.1071/EN14064.

- [106] A. P. Gondikas, F. von der Kammer, R. B. Reed, S. Wagner, J. F. Ranville, and T. Hofmann, "Release of TiO₂ Nanoparticles from Sunscreens into Surface Waters: A One-Year Survey at the Old Danube Recreational Lake," *Environ. Sci. Technol.*, vol. 48, no. 10, pp. 5415–5422, May 2014, doi: 10.1021/es405596y.
- [107] A. Gondikas *et al.*, "Where is the nano? Analytical approaches for the detection and quantification of TiO₂ engineered nanoparticles in surface waters," *Environ. Sci. Nano*, vol. 5, no. 2, pp. 313–326, Feb. 2018, doi: 10.1039/C7EN00952F.
- [108] R. B. Reed, D. P. Martin, A. J. Bednar, M. D. Montaña, P. Westerhoff, and J. F. Ranville, "Multi-day diurnal measurements of Ti-containing nanoparticle and organic sunscreen chemical release during recreational use of a natural surface water," *Environ. Sci. Nano*, vol. 4, no. 1, pp. 69–77, 2017, doi: 10.1039/C6EN00283H.
- [109] M. Hadioui, V. Merdzan, and K. J. Wilkinson, "Detection and Characterization of ZnO Nanoparticles in Surface and Waste Waters Using Single Particle ICPMS," *Environ. Sci. Technol.*, vol. 49, no. 10, pp. 6141–6148, May 2015, doi: 10.1021/acs.est.5b00681.
- [110] M. D. Montaña, H. R. Badiei, S. Bazargan, and J. F. Ranville, "Improvements in the detection and characterization of engineered nanoparticles using spICP-MS with microsecond dwell times," *Environ. Sci. Nano*, vol. 1, no. 4, pp. 338–346, 2014, doi: 10.1039/C4EN00058G.
- [111] R. d. Heringer and J. F. Ranville, "Gunshot residue (GSR) analysis by single particle inductively coupled plasma mass spectrometry (spICP-MS)," *Forensic Sci. Int.*, vol. 288, pp. e20–e25, Jul. 2018, doi: 10.1016/j.forsciint.2018.05.010.
- [112] S. Gschwind *et al.*, "Capabilities of inductively coupled plasma mass spectrometry for the detection of nanoparticles carried by monodisperse microdroplets," *J. Anal. At. Spectrom.*, vol. 26, no. 6, pp. 1166–1174, Jun. 2011, doi: 10.1039/C0JA00249F.
- [113] O. Borovinskaya, B. Hattendorf, M. Tanner, S. Gschwind, and D. Günther, "A prototype of a new inductively coupled plasma time-of-flight mass spectrometer providing temporally resolved, multi-element detection of short signals generated by single particles and droplets," *J. Anal. At. Spectrom.*, vol. 28, no. 2, pp. 226–233, Jan. 2013, doi: 10.1039/C2JA30227F.
- [114] L. Hendriks, A. Gundlach-Graham, B. Hattendorf, and D. Günther, "Characterization of a new ICP-TOFMS instrument with continuous and discrete introduction of solutions," *J. Anal. At. Spectrom.*, vol. 32, no. 3, pp. 548–561, Mar. 2017, doi: 10.1039/C6JA00400H.
- [115] J. W. Olesik and P. J. Gray, "Considerations for measurement of individual nanoparticles or microparticles by ICP-MS: determination of the number of particles and the analyte mass in each particle," *J. Anal. At. Spectrom.*, vol. 27, no. 7, p. 1143, 2012, doi: 10.1039/c2ja30073g.
- [116] A. Hegetschweiler, O. Borovinskaya, T. Staudt, and T. Kraus, "Single-Particle Mass Spectrometry of Titanium and Niobium Carbonitride Precipitates in Steels," *Anal. Chem.*, vol. 91, no. 1, pp. 943–950, Jan. 2019, doi: 10.1021/acs.analchem.8b04012.
- [117] T. Erhardt, C. M. Jensen, O. Borovinskaya, and H. Fischer, "Single Particle Characterization and Total Elemental Concentration Measurements in Polar Ice Using Continuous Flow Analysis-Inductively Coupled Plasma Time-of-Flight Mass Spectrometry," *Environ. Sci. Technol.*, vol. 53, no. 22, pp. 13275–13283, Nov. 2019, doi: 10.1021/acs.est.9b03886.
- [118] M. D. Montaña, F. von der Kammer, C. W. Cuss, and J. F. Ranville, "Opportunities for examining the natural nanogeochemical environment using recent advances in nanoparticle analysis," *J. Anal. At. Spectrom.*, vol. 34, no. 9, pp. 1768–1772, Aug. 2019, doi: 10.1039/C9JA00168A.
- [119] U. EPA, *Method 200.2, Revision 2.8: Sample Preparation Procedure for Spectrochemical Determination of Total Recoverable Elements*. US EPA Washington, DC, USA, 1994.

- [120] H. E. Pace, N. J. Rogers, C. Jarolimek, V. A. Coleman, C. P. Higgins, and J. F. Ranville, "Determining Transport Efficiency for the Purpose of Counting and Sizing Nanoparticles via Single Particle Inductively Coupled Plasma Mass Spectrometry," *Anal. Chem.*, vol. 83, no. 24, pp. 9361–9369, Dec. 2011, doi: 10.1021/ac201952t.
- [121] F. Laborda, E. Bolea, and J. Jiménez-Lamana, "Single Particle Inductively Coupled Plasma Mass Spectrometry: A Powerful Tool for Nanoanalysis," *Anal. Chem.*, vol. 86, no. 5, pp. 2270–2278, Mar. 2014, doi: 10.1021/ac402980q.
- [122] M. Baalousha, "Aggregation and disaggregation of iron oxide nanoparticles: Influence of particle concentration, pH and natural organic matter," *Sci. Total Environ.*, vol. 407, no. 6, pp. 2093–2101, Mar. 2009, doi: 10.1016/j.scitotenv.2008.11.022.
- [123] A. Nel, T. Xia, L. Mädler, and N. Li, "Toxic Potential of Materials at the Nanolevel," *Science*, vol. 311, no. 5761, pp. 622–627, Feb. 2006, doi: 10.1126/science.1114397.
- [124] A. E. Nel *et al.*, "Understanding biophysicochemical interactions at the nano–bio interface," *Nat. Mater.*, vol. 8, no. 7, Art. no. 7, Jul. 2009, doi: 10.1038/nmat2442.
- [125] K. Adachi and Y. Tainosho, "Characterization of heavy metal particles embedded in tire dust," *Environ. Int.*, vol. 30, no. 8, pp. 1009–1017, Oct. 2004, doi: 10.1016/j.envint.2004.04.004.
- [126] B. A. Butler, J. F. Ranville, and P. E. Ross, "Spatial variations in the fate and transport of metals in a mining-influenced stream, North Fork Clear Creek, Colorado," *Sci. Total Environ.*, vol. 407, no. 24, pp. 6223–6234, Dec. 2009, doi: 10.1016/j.scitotenv.2009.08.040.
- [127] C. Walther, S. Büchner, M. Filella, and V. Chanudet, "Probing particle size distributions in natural surface waters from 15 nm to 2 μ m by a combination of LIBD and single-particle counting," *J. Colloid Interface Sci.*, vol. 301, no. 2, pp. 532–537, Sep. 2006, doi: 10.1016/j.jcis.2006.05.039.
- [128] S. Baur, T. Reemtsma, H.-J. Stärk, and S. Wagner, "Surfactant assisted extraction of incidental nanoparticles from road runoff sediment and their characterization by single particle-ICP-MS," *Chemosphere*, vol. 246, p. 125765, May 2020, doi: 10.1016/j.chemosphere.2019.125765.
- [129] C.-C. Lin, S.-J. Chen, K.-L. Huang, W.-I. Hwang, G.-P. Chang-Chien, and W.-Y. Lin, "Characteristics of Metals in Nano/Ultrafine/Fine/Coarse Particles Collected Beside a Heavily Trafficked Road," *Environ. Sci. Technol.*, vol. 39, no. 21, pp. 8113–8122, Nov. 2005, doi: 10.1021/es048182a.
- [130] F. Laborda, J. Jiménez-Lamana, E. Bolea, and J. R. Castillo, "Critical considerations for the determination of nanoparticle number concentrations, size and number size distributions by single particle ICP-MS," *J. Anal. At. Spectrom.*, vol. 28, no. 8, p. 1220, 2013, doi: 10.1039/c3ja50100k.
- [131] P. Trivedi and L. Axe, "Modeling Cd and Zn Sorption to Hydrous Metal Oxides," *Environ. Sci. Technol.*, vol. 34, no. 11, pp. 2215–2223, Jun. 2000, doi: 10.1021/es991110c.
- [132] A. Sheikhsosseini, M. Shirvani, and H. Shariatmadari, "Competitive sorption of nickel, cadmium, zinc and copper on palygorskite and sepiolite silicate clay minerals," *Geoderma*, vol. 192, pp. 249–253, Jan. 2013, doi: 10.1016/j.geoderma.2012.07.013.
- [133] T. Xia *et al.*, "Comparison of the Mechanism of Toxicity of Zinc Oxide and Cerium Oxide Nanoparticles Based on Dissolution and Oxidative Stress Properties," *ACS Nano*, vol. 2, no. 10, pp. 2121–2134, Oct. 2008, doi: 10.1021/nn800511k.
- [134] N. M. Franklin, N. J. Rogers, S. C. Apte, G. E. Batley, G. E. Gadd, and P. S. Casey, "Comparative Toxicity of Nanoparticulate ZnO, Bulk ZnO, and ZnCl₂ to a Freshwater Microalga (*Pseudokirchneriella subcapitata*): The Importance of Particle Solubility," *Environ. Sci. Technol.*, vol. 41, no. 24, pp. 8484–8490, Dec. 2007, doi: 10.1021/es071445r.

- [135] R. B. Reed, D. A. Ladner, C. P. Higgins, P. Westerhoff, and J. F. Ranville, “Solubility of nano-zinc oxide in environmentally and biologically important matrices,” *Environ. Toxicol. Chem.*, vol. 31, no. 1, pp. 93–99, 2012, doi: 10.1002/etc.708.
- [136] R. F. Domingos, Z. Rafiei, C. E. Monteiro, M. A. K. Khan, and K. J. Wilkinson, “Agglomeration and dissolution of zinc oxide nanoparticles: role of pH, ionic strength and fulvic acid,” *Environ. Chem.*, vol. 10, no. 4, pp. 306–312, Aug. 2013, doi: 10.1071/EN12202.
- [137] H. Ma, P. L. Williams, and S. A. Diamond, “Ecotoxicity of manufactured ZnO nanoparticles – A review,” *Environ. Pollut.*, vol. 172, pp. 76–85, Jan. 2013, doi: 10.1016/j.envpol.2012.08.011.
- [138] A.-J. Miao *et al.*, “Zinc oxide–engineered nanoparticles: Dissolution and toxicity to marine phytoplankton,” *Environ. Toxicol. Chem.*, vol. 29, no. 12, pp. 2814–2822, 2010, doi: 10.1002/etc.340.
- [139] J. W. Moreau, P. K. Weber, M. C. Martin, B. Gilbert, I. D. Hutcheon, and J. F. Banfield, “Extracellular Proteins Limit the Dispersal of Biogenic Nanoparticles,” *Science*, vol. 316, no. 5831, pp. 1600–1603, Jun. 2007, doi: 10.1126/science.1141064.
- [140] F. Montanarella and M. V. Kovalenko, “Three Millennia of Nanocrystals,” *ACS Nano*, vol. 16, no. 4, pp. 5085–5102, Apr. 2022, doi: 10.1021/acsnano.1c11159.
- [141] J.-H. Lee *et al.*, “Artificially engineered magnetic nanoparticles for ultra-sensitive molecular imaging,” *Nat. Med.*, vol. 13, no. 1, pp. 95–99, Jan. 2007, doi: 10.1038/nm1467.
- [142] M. S. de Almeida, E. Susnik, B. Drasler, P. Taladriz-Blanco, A. Petri-Fink, and B. Rothen-Rutishauser, “Understanding nanoparticle endocytosis to improve targeting strategies in nanomedicine,” *Chem. Soc. Rev.*, vol. 50, no. 9, pp. 5397–5434, 2021, doi: 10.1039/D0CS01127D.
- [143] G. Liu, P. H. Dave, R. W. M. Kwong, M. Wu, and H. Zhong, “Influence of Microplastics on the Mobility, Bioavailability, and Toxicity of Heavy Metals: A Review,” *Bull. Environ. Contam. Toxicol.*, vol. 107, no. 4, pp. 710–721, Oct. 2021, doi: 10.1007/s00128-021-03339-9.
- [144] M. Hassellöv and F. von der Kammer, “Iron Oxides as Geochemical Nanovectors for Metal Transport in Soil-River Systems,” *Elements*, vol. 4, no. 6, pp. 401–406, Dec. 2008, doi: 10.2113/gselements.4.6.401.
- [145] M. A. Maurer-Jones, I. L. Gunsolus, C. J. Murphy, and C. L. Haynes, “Toxicity of Engineered Nanoparticles in the Environment,” *ACS Publications*, Mar. 07, 2013. <https://pubs.acs.org/doi/pdf/10.1021/ac303636s> (accessed Jan. 18, 2023).
- [146] J. A. Rizzolo *et al.*, “Soluble iron nutrients in Saharan dust over the central Amazon rainforest,” *Atmospheric Chem. Phys.*, vol. 17, no. 4, pp. 2673–2687, Feb. 2017, doi: 10.5194/acp-17-2673-2017.
- [147] M. Riediker *et al.*, “Particle toxicology and health - where are we?,” *Part. Fibre Toxicol.*, vol. 16, no. 1, p. 19, Dec. 2019, doi: 10.1186/s12989-019-0302-8.
- [148] J. R. Lead, G. E. Batley, P. J. J. Alvarez, J. D. Judy, and K. Schirmer, “Nanomaterials in the environment: Behavior, fate, bioavailability, and effects—An updated review,” *Environ. Toxicol. Chem.*, p. 35, 2018.
- [149] A. Kim, W. B. Ng, W. Bernt, and N.-J. Cho, “Validation of Size Estimation of Nanoparticle Tracking Analysis on Polydisperse Macromolecule Assembly,” *Sci. Rep.*, vol. 9, no. 1, p. 2639, Feb. 2019, doi: 10.1038/s41598-019-38915-x.
- [150] D. J. White, “PSD measurement using the single particle optical sizing (SPOS) method,” *Géotechnique*, vol. 53, no. 3, pp. 317–326, Apr. 2003, doi: 10.1680/geot.2003.53.3.317.
- [151] H. Maring, “Mineral dust aerosol size distribution change during atmospheric transport,” *J. Geophys. Res.*, vol. 108, no. D19, p. 8592, 2003, doi: 10.1029/2002JD002536.

- [152] D. Mozhayeva and C. Engelhard, “A critical review of single particle inductively coupled plasma mass spectrometry – A step towards an ideal method for nanomaterial characterization,” *J. Anal. At. Spectrom.*, vol. 35, no. 9, pp. 1740–1783, 2020, doi: 10.1039/C9JA00206E.
- [153] J. Tuoriniemi, G. Cornelis, and M. Hassellöv, “Size Discrimination and Detection Capabilities of Single-Particle ICPMS for Environmental Analysis of Silver Nanoparticles,” *Anal. Chem.*, vol. 84, no. 9, pp. 3965–3972, May 2012, doi: 10.1021/ac203005r.
- [154] L. Hendriks, A. Gundlach-Graham, and D. Günther, “Performance of sp-ICP-TOFMS with signal distributions fitted to a compound Poisson model,” *J. Anal. At. Spectrom.*, vol. 34, no. 9, pp. 1900–1909, 2019, doi: 10.1039/C9JA00186G.
- [155] A. Hineman and C. Stephan, “Effect of dwell time on single particle inductively coupled plasma mass spectrometry data acquisition quality,” *J. Anal. At. Spectrom.*, vol. 29, no. 7, pp. 1252–1257, Jun. 2014, doi: 10.1039/C4JA00097H.
- [156] N. D. Donahue *et al.*, “Assessing nanoparticle colloidal stability with single-particle inductively coupled plasma mass spectrometry (SP-ICP-MS),” *Anal. Bioanal. Chem.*, vol. 412, no. 22, pp. 5205–5216, Sep. 2020, doi: 10.1007/s00216-020-02783-6.
- [157] R. J. B. Peters *et al.*, “Detection of nanoparticles in Dutch surface waters,” *Sci. Total Environ.*, vol. 621, pp. 210–218, Apr. 2018, doi: 10.1016/j.scitotenv.2017.11.238.
- [158] A. Azimzada *et al.*, “Release of TiO₂ nanoparticles from painted surfaces in cold climates: characterization using a high sensitivity single-particle ICP-MS,” *Environ. Sci. Nano*, vol. 7, no. 1, pp. 139–148, 2020, doi: 10.1039/C9EN00951E.
- [159] T. Alshehri *et al.*, “Wildland-urban interface fire ashes as a major source of incidental nanomaterials,” *J. Hazard. Mater.*, vol. 443, p. 130311, Feb. 2023, doi: 10.1016/j.jhazmat.2022.130311.
- [160] H. Xi, P. Larouche, S. Tang, and C. Michel, “Characterization and variability of particle size distributions in Hudson Bay, Canada,” *J. Geophys. Res. Oceans*, vol. 119, no. 6, pp. 3392–3406, Jun. 2014, doi: 10.1002/2013JC009542.
- [161] C. M. Cristina and J. J. Sansalone, “‘First Flush,’ Power Law and Particle Separation Diagrams for Urban Storm-Water Suspended Particulates,” *J. Environ. Eng.*, vol. 129, no. 4, pp. 298–307, Apr. 2003, doi: 10.1061/(ASCE)0733-9372(2003)129:4(298).
- [162] A. Tewari, H. Almuhtaram, M. J. McKie, and R. C. Andrews, “Microplastics for Use in Environmental Research,” *J. Polym. Environ.*, Jul. 2022, doi: 10.1007/s10924-022-02519-w.
- [163] J. L. Green, C. A. Petty, and E. A. Grulke, “Impact grinding of thermoplastics: A size distribution function model,” *Polym. Eng. Sci.*, vol. 37, no. 5, pp. 888–895, May 1997, doi: 10.1002/pen.11732.
- [164] J. Raasch and H. Umhauer, “Errors in the Determination of Particle Size Distributions Caused by coincidences in optical particle counters,” *Part. Part. Syst. Character.*, vol. 1, no. 1–4, pp. 53–58, 1984, doi: 10.1002/ppsc.19840010109.
- [165] E. S. Cross *et al.*, “Single particle characterization using a light scattering module coupled to a time-of-flight aerosol mass spectrometer,” *Atmos Chem Phys*, 2009.
- [166] P. Kulkarni, P. A. Baron, and K. Willeke, *Aerosol Measurement: Principles, Techniques, and Applications*. John Wiley & Sons, 2011.
- [167] J. R. Jambeck *et al.*, “Plastic waste inputs from land into the ocean,” *Science*, vol. 347, no. 6223, pp. 768–771, Feb. 2015, doi: 10.1126/science.1260352.
- [168] N. O. and A. A. US Department of Commerce, “What are microplastics?” <https://oceanservice.noaa.gov/facts/microplastics.html> (accessed Apr. 15, 2023).

- [169] P. Liu *et al.*, “Critical effect of iron red pigment on photoaging behavior of polypropylene microplastics in artificial seawater,” *J. Hazard. Mater.*, vol. 404, p. 124209, Feb. 2021, doi: 10.1016/j.jhazmat.2020.124209.
- [170] F. Yu, C. Yang, Z. Zhu, X. Bai, and J. Ma, “Adsorption behavior of organic pollutants and metals on micro/nanoplastics in the aquatic environment,” *Sci. Total Environ.*, vol. 694, p. 133643, Dec. 2019, doi: 10.1016/j.scitotenv.2019.133643.
- [171] P. Liu, X. Zhan, X. Wu, J. Li, H. Wang, and S. Gao, “Effect of weathering on environmental behavior of microplastics: Properties, sorption and potential risks,” *Chemosphere*, vol. 242, p. 125193, Mar. 2020, doi: 10.1016/j.chemosphere.2019.125193.
- [172] E. Bolea-Fernandez, “Detection of microplastics using inductively coupled plasma-mass spectrometry (ICP-MS) operated in single-event mode,” p. 7, 2020.
- [173] “Mass Spectrometry of Inductively Coupled Plasmas,” *Anal. Chem.*, vol. 58, no. 1, pp. 97A-105A, Jan. 1986, doi: 10.1021/ac00292a788.
- [174] J. Jiménez-Lamana, L. Marigliano, J. Allouche, B. Grassl, J. Szpunar, and S. Reynaud, “A Novel Strategy for the Detection and Quantification of Nanoplastics by Single Particle Inductively Coupled Plasma Mass Spectrometry (ICP-MS),” *Anal. Chem.*, vol. 92, no. 17, pp. 11664–11672, Sep. 2020, doi: 10.1021/acs.analchem.0c01536.
- [175] Y. Lai *et al.*, “Counting Nanoplastics in Environmental Waters by Single Particle Inductively Coupled Plasma Mass Spectroscopy after Cloud-Point Extraction and In Situ Labeling of Gold Nanoparticles,” *Environ. Sci. Technol.*, vol. 55, no. 8, pp. 4783–4791, Apr. 2021, doi: 10.1021/acs.est.0c06839.
- [176] R. J. Rauschendorfer *et al.*, “Development and Application of Nanoparticle-Nanopolymer Composite Spheres for the Study of Environmental Processes,” *Front. Toxicol.*, vol. 3, p. 752296, Dec. 2021, doi: 10.3389/ftox.2021.752296.
- [177] M. Schmiedgruber, R. Hufenus, and D. M. Mitrano, “Mechanistic understanding of microplastic fiber fate and sampling strategies: Synthesis and utility of metal doped polyester fibers,” *Water Res.*, vol. 155, pp. 423–430, May 2019, doi: 10.1016/j.watres.2019.02.044.
- [178] A. S. Keller, J. Jimenez-Martinez, and D. M. Mitrano, “Transport of Nano- and Microplastic through Unsaturated Porous Media from Sewage Sludge Application,” *Environ. Sci. Technol.*, vol. 54, no. 2, pp. 911–920, Jan. 2020, doi: 10.1021/acs.est.9b06483.
- [179] A. L. Andrady, “The plastic in microplastics: A review,” *Mar. Pollut. Bull.*, vol. 119, no. 1, pp. 12–22, Jun. 2017, doi: 10.1016/j.marpolbul.2017.01.082.
- [180] R. B. Fox, L. G. Isaacs, and S. Stokes, “Photolytic degradation of poly(methyl methacrylate),” *J. Polym. Sci. A*, vol. 1, no. 3, pp. 1079–1086, Mar. 1963, doi: 10.1002/pol.1963.100010321.
- [181] “The photo-degradation of polymethylmethacrylate I. The mechanism of degradation,” *Proc. R. Soc. Lond. Ser. Math. Phys. Sci.*, vol. 210, no. 1103, pp. 461–481, Jan. 1952, doi: 10.1098/rspa.1952.0013.
- [182] A. Torikai, M. Ohno, and K. Fueki, “Photodegradation of poly(methyl methacrylate) by monochromatic light: Quantum yield, effect of wavelengths, and light intensity,” *J. Appl. Polym. Sci.*, vol. 41, no. 56, pp. 1023–1032, 1990, doi: 10.1002/app.1990.070410513.
- [183] T. S. Hebner and M. A. Maurer-Jones, “Characterizing microplastic size and morphology of photodegraded polymers placed in simulated moving water conditions,” *Environ. Sci. Process. Impacts*, vol. 22, no. 2, pp. 398–407, 2020, doi: 10.1039/C9EM00475K.

- [184] N. Meides *et al.*, “Reconstructing the Environmental Degradation of Polystyrene by Accelerated Weathering,” *Environ. Sci. Technol.*, vol. 55, no. 12, pp. 7930–7938, Jun. 2021, doi: 10.1021/acs.est.0c07718.
- [185] M. Hadiuzzaman, M. Salehi, and T. Fujiwara, “Plastic litter fate and contaminant transport within the urban environment, photodegradation, fragmentation, and heavy metal uptake from storm runoff,” *Environ. Res.*, vol. 212, p. 113183, Sep. 2022, doi: 10.1016/j.envres.2022.113183.
- [186] J. Brandon, M. Goldstein, and M. D. Ohman, “Long-term aging and degradation of microplastic particles: Comparing in situ oceanic and experimental weathering patterns,” *Mar. Pollut. Bull.*, vol. 110, no. 1, pp. 299–308, Sep. 2016, doi: 10.1016/j.marpolbul.2016.06.048.
- [187] D. Vione, M. Minella, V. Maurino, and C. Minero, “Indirect Photochemistry in Sunlit Surface Waters: Photoinduced Production of Reactive Transient Species,” *Chem. - Eur. J.*, vol. 20, no. 34, pp. 10590–10606, Aug. 2014, doi: 10.1002/chem.201400413.
- [188] K. G. de C. Monsores, A. O. da Silva, S. de S. A. Oliveira, J. G. P. Rodrigues, and R. P. Weber, “Influence of ultraviolet radiation on polymethylmethacrylate (PMMA),” *J. Mater. Res. Technol.*, vol. 8, no. 5, pp. 3713–3718, Sep. 2019, doi: 10.1016/j.jmrt.2019.06.023.
- [189] I.-S. Kim, H. Cho, K.-S. Sohn, K. Kim, and S. Kim, “A study on the severe crazing phenomenon of the PMMA canopy under prolonged exposure to tropical climates,” *Eng. Fail. Anal.*, vol. 129, p. 105719, Nov. 2021, doi: 10.1016/j.engfailanal.2021.105719.
- [190] B. Dickens, J. W. Martin, and D. Waksman, “Thermal and photolytic degradation of plates of poly(methyl methacrylate) containing monomer,” *Polymer*, vol. 25, no. 5, pp. 706–715, May 1984, doi: 10.1016/0032-3861(84)90041-7.
- [191] A. K. Sarkar, A. E. Rubin, and I. Zucker, “Engineered Polystyrene-Based Microplastics of High Environmental Relevance,” *Environ. Sci. Technol.*, vol. 55, no. 15, pp. 10491–10501, Aug. 2021, doi: 10.1021/acs.est.1c02196.
- [192] J. L. Bitter, J. Yang, S. B. Milani, C. T. Jafvert, and D. Howard Fairbrother, “Transformations of oxidized multiwalled carbon nanotubes exposed to UVC (254 nm) irradiation,” *Environ. Sci. Nano*, vol. 1, no. 4, pp. 324–337, 2014, doi: 10.1039/C4EN00073K.
- [193] P. Liu *et al.*, “Polystyrene microplastics accelerated photodegradation of co-existed polypropylene via photosensitization of polymer itself and released organic compounds,” *Water Res.*, vol. 214, p. 118209, May 2022, doi: 10.1016/j.watres.2022.118209.
- [194] T. F. Mundhenke, S. C. Li, and M. A. Maurer-Jones, “Photodegradation of polyolefin thin films in simulated freshwater conditions,” *Environ. Sci. Process. Impacts*, vol. 24, no. 12, pp. 2284–2293, Dec. 2022, doi: 10.1039/D2EM00359G.
- [195] C.-W. Cui, C. Yang, J. Bao, X.-J. Huang, X.-F. Zeng, and J.-F. Chen, “Monodispersed ZnO Nanoparticle-Poly(methyl methacrylate) Composites with Visible Transparency for Ultraviolet Shielding Applications,” *ACS Appl. Nano Mater.*, vol. 3, no. 9, pp. 9026–9034, Sep. 2020, doi: 10.1021/acsnm.0c01723.
- [196] L. Zhu, S. Zhao, T. B. Bittar, A. Stubbins, and D. Li, “Photochemical dissolution of buoyant microplastics to dissolved organic carbon: Rates and microbial impacts,” *J. Hazard. Mater.*, vol. 383, p. 121065, Feb. 2020, doi: 10.1016/j.jhazmat.2019.121065.
- [197] P. L. Corcoran, M. C. Biesinger, and M. Grifi, “Plastics and beaches: A degrading relationship,” *Mar. Pollut. Bull.*, vol. 58, no. 1, pp. 80–84, Jan. 2009, doi: 10.1016/j.marpolbul.2008.08.022.
- [198] I. Efimova, M. Bagaeva, A. Bagaev, A. Kileso, and I. P. Chubarenko, “Secondary Microplastics Generation in the Sea Swash Zone With Coarse Bottom Sediments: Laboratory Experiments,” *Front. Mar. Sci.*, vol. 5, 2018, Accessed: Apr. 24, 2023. [Online]. Available: <https://www.frontiersin.org/articles/10.3389/fmars.2018.00313>

- [199] Y. K. Song, S. H. Hong, M. Jang, G. M. Han, S. W. Jung, and W. J. Shim, "Combined Effects of UV Exposure Duration and Mechanical Abrasion on Microplastic Fragmentation by Polymer Type," *Environ. Sci. Technol.*, vol. 51, no. 8, pp. 4368–4376, Apr. 2017, doi: 10.1021/acs.est.6b06155.
- [200] F. Zha *et al.*, "Release of millions of micro(nano)plastic fragments from photooxidation of disposable plastic boxes," *Sci. Total Environ.*, vol. 858, p. 160044, Feb. 2023, doi: 10.1016/j.scitotenv.2022.160044.

APPENDIX A PERMISSIONS

The content of chapter 2 was adapted from a published article:

S. Bevers, M. D. Montano, L. Rybicki, T. Hofmann, F. von der Kammer, J. F. Ranville. “Quantification and Characterization of Nanoparticulate Zinc in an Urban Watershed.” *Frontiers in Environmental Science: Biogeochemical Dynamics*, 8:84 (2020).

Permission to adapt and republish this material was granted by the statement of the Frontiers in Environmental Journal Copyright Statement from the journal website:

“Copyright Statement

Under the Frontiers Conditions for Website Use and the Frontiers General Conditions for Authors, authors of articles published in Frontiers journals retain copyright on their articles, except for any third-party images and other materials added by Frontiers, which are subject to copyright of their respective owners. Authors are therefore free to disseminate and re-publish their articles, subject to any requirements of third-party copyright owners and subject to the original publication being fully cited. The ability to copy, download, forward or otherwise distribute any materials is always subject to any copyright notices displayed. Copyright notices must be displayed prominently and may not be obliterated, deleted or hidden, totally or partially.”

Accessed 8/17/2023.

The entirety of this statement can be found at the website address:

<https://www.frontiersin.org/journals/environmental-science/about#copyright-statement>